Computational Agent-Based Modeling of Surgical Vocal Fold Injury and Repair

Aman Garg, B.Eng.

Department of Biomedical Engineering

McGill University, Montréal

August 2018

A thesis submitted to McGill University in partial fulfilment of the requirements

of the degree of Master of Engineering

ACKNOWLEDGEMENTS

I would like to graciously thank my co-authors Jeannie A. C. Karwowski, Michael Powell and Prof. Jon T. Sakata for their continuous assistance and support in conducting this research work. I would like to acknowledge my laboratory colleagues Patrick Coburn, Grace Yu and Caroline Shung for their intermittent assistance and contributions.

I would like to recognize the advice and help provided by my supervisors Dr. Nicole Li-Jessen and Prof. Luc Mongeau throughout the duration of my Master's study. Their patience, unwavering support and expert guidance were of immense value and comfort without which this work would undoubtedly not have been possible. I would also like to acknowledge the research operating grant from the National Institute of Deafness and other Communication Disorder of the National Institutes of Health under award number R03DC012112 (PI: Li-Jessen) and R01DC005788 (PI: Mongeau) for conducting the work presented in this thesis.

I would like to thank Dr. Joseph Jaja and Nuttiiya Seekhao for their collaboration in the adaptation of the vocal fold agent-based model to rodent specification. Special thanks to our lab's Research Assistant, Samson Yuen for helping at various stages during my thesis by solving issues during model calibration. Finally, I would like to thank my family for their unconditional support, guidance and tolerance.

PREFACE

In accordance with the thesis preparation and submission guidelines, this thesis has been written in the form of a compilation of two original research articles, presented in Chapters 2 and 3. Each research article consists of sections as per the journal guidelines. I am the first author of both articles. In the capacity of a master's student, my contributions towards these manuscripts included literature review, experiment design, data analysis and interpretation and manuscript preparation. The contributions of co-authors are included in each manuscript.

ABSTRACT

Voice disorders affect about one in ten adults at some point in their lifetime. Vocal fold scarring can result from surgical excision of benign and malignant vocal fold lesions. The elicited inflammation and healing response is complex and dynamic. It involves immune and repair cells (e.g., neutrophils, macrophages, fibroblasts) and molecules (e.g., inflammatory cytokines, damage-associated molecular pattern molecules) to locate damaged tissue, eliminate the necrotic cells and debris, and produce extracellular matrix substances for eventual tissue repair. A mechanistic understanding of the vocal fold injury and repair process will help in identifying the effective treatments for iatrogenic vocal fold scarring from surgery.

The overall goal of this thesis was to develop computational agent-based models (ABM) that could numerically simulate the dynamics of major cellular and molecular components involved in surgical vocal fold injury and repair. The first research goal was to phenotype and enumerate immune and repair cells in surgically injured rat vocal folds up to 4 weeks after surgical injury. Viable cells were isolated from harvested vocal folds and were stained for cell surface markers specific to neutrophils, macrophages, endothelial cells and fibroblasts. Multi-parametric flow cytometry was then conducted to count the number of cells for each cell population in the vocal fold samples.

The second research goal was to calibrate and validate existing agent-based models of vocal fold injury and repair (VF-ABM) with the flow cytometry data. Global sensitive analysis using Random Forests were first employed to identify the most influential model parameters on the outputs of cell numbers. The Robust Parameter Estimation (ROPE) algorithm from the package

of Statistical Parameter Optimization Tool for Python (SPOTPY) was then used to calibrate VF-ABM for early time points from Day 1 to Day 5 of the flow cytometry data. Subsequently, VF-ABM were run 100 times to generate 95% confidence intervals for model evaluation. VF-ABM predicted outputs were considered accurate if the empirical data points were within the 95% confidence intervals of simulated outputs. Cell population quantities were calculated for Day 7, Week 2 and Week 4 respectively against the empirical flow cytometry data. Predicted cell populations reached 100% accuracy for Day 7. Although VF-ABM generated qualitative trends of cell population comparable to those of Weeks 2 and 4, the corresponding empirical data values fell outside of the 95% confidence intervals.

Results from the flow cytometry study provided quantitative and time-dependent data on major cell populations involved in surgical vocal fold injury. Results from the model verification informed the area of improvements for the next generation of VF-ABM. This thesis contributes to the development of a computational tool that would better inform clinicians in prescribing treatments for patients with voice disorders.

ABRÉGÉ

Les problèmes de la voix affectent environ un adulte sur dix à un moment ou à un autre de leur vie. La cicatrisation des replis vocaux peut résulter de l'excision chirurgicale des lésions d bénignes et malignes. Des cellules (neutrophiles, macrophages, fibroblastes) et molécules (cytokines inflammatoires, molécules associées aux dégâts) immunitaires et réparatrices participent à la réponse inflammatoire et cicatrisante. Ce processus implique la localisation du tissu endommagé, l'élimination de cellules nécrotiques et de débris, et la production de substances de la matrice extracellulaire pour la réparation éventuelle du tissu. Une meilleure compréhension du processus de réparation et de blessure des cordes vocales aidera à identifier les traitements efficaces pour la cicatrisation des plis vocaux iatrogènes suite aux complications chirurgicales.

L'objectif principal de cette thèse était de développer des modèles numériques multi-agents (SMA) pour des simulations dynamiques du rôle des principaux composants cellulaires et moléculaires impliqués dans la blessure et la réparation des replis vocaux. Le premier objectif de lu présente était de déterminer les phénotypes des cellules immunitaires en utilisant la cytométrie en flux dans la réparation des cordes vocales de rat. Des cellules vivantes ont été récoltées de cordes vocales et ont été colorées avec des marqueurs de surface cellulaire spécifiques aux neutrophiles, macrophages, cellules endothéliales, et fibroblastes. La cytométrie de flux multi-paramétrique a ensuite été utilisée pour compter le nombre de chaque population de cellule.

Le deuxième objectif était de calibrer et valider un modèle informatique basé sur un SMA de la blessure aux replis vocaux et leur réparation utilisant les données de lu cytométrie de flux. Une analyse de sensibilité globale busée sur les méthode « Random Forests » a été utilisé pour

identifier les paramètres du modèle les plus influents sur les populations cellulaires. L'algorithme ROPE (Robust Parameter Estimation) de l'outil d'optimisation statistique des paramètres pour Python (SPOTPY) a ensuite été utilisé pour calibrer le VF-ABM pour la période initiale allant du Jour 1 au Jour 5 des données de cytométrie de flux. Par la suite, VF-ABM ont été exécutés 100 fois pour générer des intervalles de confiance à 95% pour l'évaluation du modèle. Les permis ont été évaluées avec des prédiction intervalles de confiance de 95% par comparaisons avec les donnesse expérimentales de prédictions a été évaluée pour les semaines 1, 2, et 4 respectivement par rapport aux données empiriques de cytométrie de flux. Bien que les tendances qualitatives de la population cellulaire prédites sout comparables à celles des données empiriques pour les semaines 2 et 4, les valeurs des données empiriques déposent les intervalles de confiance.

Les résultats de l'étude de cytométrie de flux ont fourni des données quantitatives et dépendantes du temps sur les principales populations de cellules impliquées dans la lésion du re pli vocal chirurgical. Les résultats de la vérification du modèle suggèrent des améliorations possibles pour la prochaine génération de VF-ABM. Cette thèse constitue une étape essentielles dans le développement d'un outil de calcul qui permettrait de mieux informer les cliniciens dans la prescription de traitements individualises pour les patients atteints de troubles de la voix.

TABLE OF CONTENT

LIST OF TABLES

LIST OF FIGURES

CHAPTER 1: INTRODUCTION

1.1 Clinical Motivation

Approximately 17.9 million adults (7.6%) in the United States experience voice disorders at some points in their lifetime [1-3]. Voice disorders involve impairments with varying pitch, quality and loudness in daily conversation as well as occupational voice use such as in voice performance and teaching. Among all voice disorders, vocal fold scarring is considered as the most perplexing clinical problem because current treatment options to fully repair the fibrotic tissue are limited [4-6]. Vocal fold scars can be developed within the lamina propria after surgical removal of benign or malignant vocal fold lesions. The scarred tissue alters the microarchitecture and vibratory functions of the vocal folds and results in a debilitating condition of the human voice, i.e., dysphonia [4-10]. Iatrogenic vocal fold scarring triggers a cascade of cellular and molecular events associated with inflammation and wound repair, whereas the degree of response varies across patients depending on a myriad of personal and lifestyle factors. Computer simulation has become an appealing approach to help integrate and analyze massive patient data for personalized medical treatments. The overall goal of this thesis was to improve the accuracy of existing vocal fold agent-based models (VF-ABM) in simulating cellular and molecular activities associated with surgical vocal fold injury and repair. Two experimental studies were conducted. For the first study, the research goal was to identify and phenotype immune and repair cells in surgically injured rat vocal folds up to 4 weeks after surgical injury. In the second study, the biological representation of VF-ABM was optimized through sensitivity analysis, model calibration and verification using flow cytometry data from the first study. The ultimate goal is to further develop ABM into a computer

software that could pre-operatively inform clinicians about an individual's risk of iatrogenic scarring from surgery.

1.2 Vocal Folds

The vocal folds are located within the larynx. Human vocal folds are comprised of three major layers namely the epithelium, the lamina propria (LP), and the vocalis muscle [11, 12]. The lamina propria of vocal folds can be further anatomically categorized into three layers from superficial to deep based on their histological compositions. These three layers are the superficial lamina propria (SLP), the intermediate lamina propria (ILP), and the deep lamina propria (DLP). The superficial layer (SLP) is characterized by loose tissue with a small amount of collagen or elastin fibers, while the intermediate layer (ILP) and the deep layer (DLP) have a high concentration of elastin fiber and collagen fibers, respectively [12, 13]. This unique layered microstructure allows human vocal folds to withstand high-frequency mechanical deformations during human phonation [14].

Distinctive cell populations have been identified across the three layers of LP. Most of the vocal fold cellularity data have been acquired using rodent models because of the common tri-layered structure of LP between rodents and human [15-26]. The major vocal fold cell populations include fibroblasts, myofibroblasts, neutrophils and macrophages. Fibroblasts are reported to be the most abundant cell type in uninjured and injured rat vocal folds. In uninjured vocal folds, the DLP contains the highest concentration of fibroblasts [27, 28]. Fibroblasts were found to be distributed uniformly throughout the LP after injury [27, 28]. Macrophages and myofibroblasts were found to be predominantly localized in the SLP of injured and uninjured vocal folds [27-30]. Compared to other cells, blood-circulatory neutrophils were found in low concentration in

uninjured LP, but were evidently recruited after surgical vocal fold injury in rats [31]. Time-varying, quantitative data of these cell populations related to vocal fold scarring, however, do not exist in literature and thus research on this topic would be timely and warranted.

1.3 Need for Computational Biology

Complex and dynamic interactions between cells, signaling molecules and extracellular matrix are triggered by surgery. The resulting outcomes of tissue repair are often unpredictable and largely depend on many health factors such as lesion type, severity and patients' health status [4, 6, 10]. At present, prophylactic or adjunctive therapeutics are available for the treatment of iatrogenic vocal fold scarring but their treatment effects are notably patient-dependent [32-37]. Some examples of such treatments include behavioral voice therapies, growth factor therapies, cell therapies and use of injectable augmentation substances [38-40]. As such, a comprehensive understanding of the time-varying inflammation and healing mechanism associated with surgical vocal fold injury and scarring is necessary to optimize the preventive and therapeutic care of vocal fold injuries.

Systems biology approaches have been applied to help understand disease complexity such as traumatic brain injury, sepsis, diabetes and acute liver failure [41-47]. Owing to a large number of interacting components in biological systems, the conventional experimental approach of studying one isolated cell or molecule is not sufficient to understand the complexity of biological systems. Conventional experimental approaches have generated much useful knowledge and information about individual components and functions of biological systems [48, 49]. The challenge is to connect these datasets in comprehending the complex dynamics of these systems

[49]. The study of isolated subsystems following a reductionist approach tends to obscure mechanisms of interaction between different components and the associated biological complexity [48]. For example, enzymes in a specific molecular pathway are often analyzed in isolation. Catalytic reactivity for these biological catalysts (enzymes) is however emerging from complex and dynamic interactions among various components (e.g., reactants, substrates, products etc.) of the targeted pathway [50]. The aggregated dynamics of these interactions are not intuitive and cannot be conceptualized by investigating each enzyme individually [50].

Systems biology provides an alternative method of investigating the aggregated activity of individual biological components at a systems level. In other words, systems biology focuses on the comprehension of how a process, a cell, a group of cells, or an organism act as a whole [51]. The main tool in systems biology is computational modeling and simulation. For instance, systems biology has been used for creating simulations of signalling pathways, transcription networks, physiological processes, biochemical mechanisms and metabolic processes [49]. Systems biology can be used to quantify the interrelationships (structure or organization) and interaction (behavior or dynamics) between biological components and provide insights into developing a mechanistic understanding of complex biological processes [52]. Systems biology does not only quantify interactions between components, but also potentially reproduces the emergent properties of the system. For example, agent based models (ABM) allow numerical simulations of the behavior of individual components (agents) and their interactions that in turn generate an emergent behavior based on the aggregated behaviors of individual agents [53].

Computational models have been shown to improve our understanding of molecular, cellular, tissue and population behavior in health and diseases [52, 54]. For instance, numerical

simulations have been used to investigate the response of an entire human immune system to various diseases at scales ranging from individual antigens to systematic behavior [55]. Computational models can also be used to test various hypotheses (i.e., in silico experiments) that may be challenging to perform empirically in human patients [52, 54]. In the era of personalized/ precision medicine, computational models have become an indispensable tool to integrate different forms of patient data (e.g., demographics, clinical, lifestyle etc.) and generate specific disease phenotypes or cohorts for in silico clinical trials [56, 57].

The Canadian Institutes of Health Research (CIHR) and the National Institutes of Health (NIH) in the United States have emphasized the use of computational models to understand complex diseases in conjunction with conventional experimental approaches [58]. Patient-specific computational models have already been developed for numerous inflammatory diseases, such as traumatic brain injury, sepsis and acute liver failure [41-45]. However, no such models have been developed for characterizing the inflammatory and healing process of the vocal folds. Our research group has been working on the development of computational ABM to numerically simulate the dynamics of major cellular and molecular components involved in surgical vocal fold injury and repair [59-66]. The ultimate goal was to further transform ABM into computer software that can guide surgeons in the best methods to repair voices that have been lost by predicting individual patients' response to vocal fold surgery.

1.4 Agent Based Models in Vocal Fold Biology

Agent-based models (ABM) is a bottom-up simulation approach [67]. ABM emphasizes the employment and interaction of self-directed decision-making entities called agents [67]. The main

components of ABM include agents, rules for governing the actions and decisions of these agents and virtual environment where these agents interact with. The framework of ABM is flexible for incorporating both spatial domain and stochasticity [67]. The emergent phenomena in ABM resulting from interactions of agents make it advantageous for modeling biological systems [67]. Such emergent phenomena can be found in traffic flow, stock market, disasters and corporate organizations [53]. For example, disaster situations such as fire in crowded places result in panic among people. This collective panic behavior is an emergent phenomenon that originates from complex individual-level behavior and interactions between individuals [53]. Based on the simulation results, practical ways can be suggested to optimize the escape strategy for tackling such disaster situations [68]. In biology, the organization of a cell, tissue or an organ system can also be considered as an example of the emergent phenomenon [49]. For instance, biological macromolecules self-organize to yield complex functional structures such as organelles, protein complexes, tissues and whole cells [49].

Our research group has developed a series of ABM to numerically simulate acute vocal fold inflammation, including phonotrauma and surgical vocal fold trauma [59-63, 69]. The models were partially calibrated and verified with animal and human vocal fold data [18-20, 70, 71]. The ABM represented a three-dimensional (3D) vocal fold LP that is populated by cells [platelets, macrophages, neutrophils, fibroblasts], extracellular matrix (ECM) substances [collagen type I, elastin and Hyaluronic acid (HA)] and chemical mediators [tumor necrosis factor-α (TNF-α), interleukin-1β (IL-1β), interleukin-10 (IL-10), interleukin-6 (IL-6) interleukin-8 (IL-8), basic fibroblast growth factor (bFGF), and transforming growth factor (TGF-β1)]. However, as quantitative data on vocal fold cellularity were limited, the cellular data have not been fully

characterized in the model. Specifically, model parameters related to immune and repair cells have not been calibrated and validated with empirical experiments. Both empirical and computational experiments are thus needed to improve the numerical simulation of cellular outputs of the vocal fold ABM.

1.5 Thesis Research Objectives

The overall goal of this study was to develop computational agent-based models (ABM) that could numerically simulate the dynamics of major cellular and molecular components involved in surgical vocal fold injury and repair. This research contributes to the development of a computational tool that would better inform clinicians about an individual's risk of iatrogenic scarring from surgery and help them in prescribing treatments for patients with voice disorders. The specific aims of this project were:

1. To phenotype and enumerate immune and repair cells including neutrophils, macrophages, endothelial cells and fibroblasts in surgically injured rat vocal folds using multiparametric flow cytometry, up to 4 weeks post-injury.
2. To calibrate and validate the existing ABM of surgical vocal fold injury and repair with the empirical flow cytometry data.

1.6 Original Contributions

To achieve research objectives outlined above, several original contributions were made: development of theoretical concepts, design of experiment, design and implementation of bivariate gating strategy, identification of cellular types and subtypes, interpretation of trends of cell populations, implementation of correlation analyses and mixed effect models for statistical

analysis of flow cytometry results, development of algorithms for sensitivity analysis, implementing Random Forests, data curation, developing three strategies for model calibration and validation, agent based model calibration using SPOTPY, statistical evaluation of model, and writing of manuscripts.

1.7 Thesis Outline

Chapter 1 introduces the clinical motivation, background and research objectives of this thesis. Chapters 2 and 3 are the two original papers (Garg Aman, Karwowski Jeannie A. C., Powell Michael, Sakata Jon T., Li-Jessen Nicole Y. K., *Multi-parametric flow cytometry for cell phenotyping in surgical vocal fold injuries.* Laryngoscope, 2018 and Garg Aman, Yuen Samson, Seekhao Nuttiiya, Yu Grace, Jaja Joseph, Mongeau Luc, Li-Jessen Nicole Y. K., *Towards a physiological scale of vocal fold agent-based biological models: sensitivity analysis, calibration and validation*. IEEE Transactions on Computational Biology and Bioinformatics, 2018) of this thesis research to be submitted to peer-reviewed journals. Chapter 4 summarizes the conclusions of this thesis and discusses the future directions of this research.

CHAPTER 2: CELL PHENOTYPING IN VOCAL FOLDS

2.1 PREFACE

Quantitative data on the temporal dynamics of cell population involved in vocal fold surgical injury are limited in the literature. One objective of the present study was to identify and enumerate major cell populations, including neutrophils, macrophages, endothelial cells and fibroblasts in injured rat vocal folds up to four weeks post-surgery. The extended follow-up time-point research design with the technology of multi-parametric flow cytometry would advance current understanding of major cell populations associated with vocal fold injury and repair. Two independent flow cytometry panels (Panel A including 11 parameters and Panel B including eight parameters) were used for cell identification. Bivariate gating analysis was used to identify individual cell populations. The time-varying dynamics of individual cell populations were observed following surgical vocal fold injury. The experimental part of this manuscript was conducted at University of Maryland by Jeannie A. C. Karwowski (JACK) and Michael Powell (MP) under the supervision of Dr. Nicole Y. K. Li-Jessen (NLJ). My contributions towards this manuscript include development of theoretical concepts, literature review, design and implementation of bivariate gating strategy, identification of cellular types and subtypes, interpretation of trends of cell populations, implementation of correlation analyses and mixed effect models for statistical analysis of flow cytometry results, data analysis and interpretation, and manuscript preparation.

Multi-parametric flow cytometry for cell phenotyping in surgical vocal fold injuries

Aman Garg[1], Jeannie A. C. Karwowski, Michael Powell[2], Jon T. Sakata[3], Nicole Y. K. Li-Jessen[1,4,5*]

[1] Department of Biological and Biomedical Engineering, McGill University, Montreal, Quebec, Canada

[2] Virginia Tech Carillon Research Institute, Roanoke, Virginia, U.S.A.

[3] Department of Biology, McGill University, Montreal, Quebec, Canada

[4] School of Communication Sciences and Disorders, McGill University, Montreal, Quebec, Canada

[5] Department of Otolaryngology – Head and Neck Surgery, McGill University, Montreal, Quebec, Canada

[*] Corresponding author

E-mail: nicole.li@mcgill.ca (NLJ)

AG: Data Curation, Formal analysis, Software, Validation, Visualization, Writing - original draft, Writing - Review and editing

JACK: Data Curation, Investigation, Methodology, Writing - Review and editing

MP: Data Curation, Investigation, Methodology

JTS: Formal analysis, Supervision, Validation, Writing - Review and editing

NLJ: Conceptualization, Fund acquisition, Investigation, Methodology, Project administration, Resources, Supervision, Validation, Writing - Review and editing

2.2 ABSTRACT

Background: A comprehensive profile of cellularity following vocal fold surgery is integral to the understanding of iatrogenic scarring. The goal of this study was to identify and phenotype neutrophils, macrophages, endothelial cells and fibroblasts in injured rat vocal folds up to four weeks after surgery.

Methods: Vocal folds were scarred bilaterally in 140 rats and 20 rats were used as uninjured controls. Cells were isolated from harvested vocal fold mucosae and subjected to an 11-parameter flow cytometry analysis.

Results: Populations of neutrophils (CD45+His48+), macrophages (CD106-CD44H+/ His48-CD68+) and endothelial cells (CD29+CD44H+CD106+) were identified in surgically injured vocal folds. Fibroblasts (CD29+CD105+CD106-) were identified in both injured and uninjured vocal folds. Subtypes of macrophages and fibroblasts, putatively corresponding to classically and alternatively activated macrophages and to typical fibroblasts and myofibroblasts, were also identified.

2.3 INTRODUCTION

Voice disorders are the most common communication disorder across the lifespan, afflicting almost one-third of the general population in North America at any point in their life [72-75]. Phonosurgery is required to remove vocal fold lesions in patients if they are not motivated to engage in conservative voice therapy [76, 77]. Unfortunately, persistent dysphonia associated with iatrogenic scarring of vocal folds can occur in patients after the operation [4-10]. Surgical injury induces a highly complex acute inflammation and healing response that can lead to stiff, fibrotic

vocal folds. Immune cells (neutrophils and macrophages), repair cells (fibroblasts and endothelial cells) and signaling molecules (e.g., cytokines, growth factors, damage-associated molecular pattern molecules [DAMPs] etc.) are involved to locate damaged tissue, eliminate the necrotic cells and debris, and produce extracellular matrix (ECM) substances for eventual tissue repair [78-83]. Temporal dynamics of cytokines, DAMP and ECM have been widely studied in vocal fold scarring after surgery using animal models [29, 30, 84-106]. In contrast, information on vocal fold cellularity is relatively limited to reports from a few healthy human studies [27, 28, 107] and a handful of animal studies [18, 30, 87, 108-111] (**Table 2.1**).

In young and adult healthy human vocal folds, fibroblasts, macrophages and myofibroblasts were reported as major cell populations in the lamina propria [27, 28, 107]. Fibroblasts were abundant in all layers of lamina propria with the highest number in the deep lamina propria [28]. Macrophages and myofibroblasts were predominantly found in the superficial lamina propria of healthy vocal folds [27, 28]. Little is known about how these cell populations change following vocal fold injury in humans. Animal studies provided relatively qualitative information about cellularity changes following surgical damage to vocal folds in rats [18, 108, 109], rabbits [111] and pigs [30, 87] (**Table 2.1**). In general, neutrophil-like cells were reported to peak within one day in surgically injured vocal folds. These cells then dramatically decreased three days after injury, suggesting a phase transition from inflammation to wound repair at that time [108]. Macrophages were also reported in injured porcine vocal folds [30]. Several macrophage phenotypes including SLA-DR+, CD16+/SLA+, CD80/86+/SLA-DR+ and CD163+/SLA-DR+ were reported following surgical vocal fold injury [30]. Lastly, fibroblasts were found to be the

most dominant cell population in injured rat vocal folds [18]. Fibroblasts were notably present from Day 1 to Day 7 with maximum density at Day 3 following surgery [18, 109, 111].

In most of the aforesaid reports, conventional histological and immunostaining techniques were used for cell identification in vocal folds [18, 27, 28, 108, 111]. Histological staining is semi-quantitative in nature with a low sensitivity [112]. Flow cytometry offers a quantitative and sensitive method to characterize the identity and behaviour of cell populations [113, 114]. Flow cytometry discriminates cell types based on their size and granularity due to the light scattering property of cells [115, 116]. Flow cytometry also allows for the identification of multiple and specific cell populations using fluorescence labels targeting antigenic cell-surface or intracellular proteins [117]. For instance, flow cytometry has been widely applied to understand lymphocyte and macrophage subpopulations [118], leukocyte differentiation pathways [119] and intracellular cytokine expression [120-123].

Surgical trauma is a well-cited cause of vocal fold scarring and the secondary dysphonia presents one of the most challenging and functionally debilitating conditions affecting the human voice [4-6, 10, 15, 124-127]. A comprehensive understanding of the inflammation and healing mechanisms underlying vocal fold scarring is to design effective preventive and therapeutic intervention for this recalcitrant vocal condition. In the current study, a maximum 11-parameter flow cytometry panel was employed to identify and enumerate neutrophils, macrophages, fibroblasts and endothelial cells in rat vocal folds up to 4 weeks following surgery. The goal was to improve our understanding of major cell populations associated with vocal fold injury and repair.

2.4 MATERIALS AND METHODS

2.4.1 Experimental Design and Hypothesis

The current study was a one-way between-subjects design with time [0 (uninjured control), 1, 2, 3, or 5 days, and 1, 2, or 4 weeks post-surgery] as the independent variable. These time points represent the typical progression from acute inflammation to late tissue remodeling [15, 18, 20, 21, 91, 110, 128]. Dependent variables were percentages of neutrophils, macrophages, fibroblasts, and endothelial cells in the overall cell population. These cells represent fundamental immune and repair cell types involved in inflammation and healing [78, 80-82, 129]. Based on skin and vocal fold literature [18, 82], we hypothesized that immune cells in vocal folds (neutrophils and macrophages) would permeate the wound site within one day after surgery, while repair cells (fibroblasts and endothelial cells) would start to accumulate around three days after surgery.

2.4.2 Vocal Fold Surgical Model

The animal study was approved by the Institutional Animal Care and Use Committee of the University of Maryland-College Park (protocol number: R-12-85). A total of 160 male Sprague-Dawley rats (four to six months old, 450-500 g) were used in the study. Rats were selected because they share important structural similarities with human vocal folds [15, 16, 86]. Also, most biological data pertinent to vocal fold scarring and its treatments have been previously reported for rat models [16-18, 20-23, 108-110].

Vocal fold injuries were performed in 140 rats using an established protocol. Twenty rats were used as uninjured controls [15]. Regarding the surgical protocol, animals were anesthetized, and their vocal folds were bilaterally injured using a 25-gauge needle to strip the vocal fold mucosa

until the thyroarytenoid muscle was exposed [15]. At each end-point of the study, animals were euthanized via CO_2 asphyxiation, and larynges were removed immediately following euthanasia [15]. For anesthesia induction, the rats were injected with isoflurane (2% to 3% delivered at 0.8 to 1.5 L/min) followed by maintenance with an intraperitoneal injection of ketamine hydrochloride (90 mg/ kg) and xylazine hydrochloride (9 mg/kg). Rats with injured vocal folds were euthanized at each of seven post-surgery time points: Days 1, 2, 3, 5 and Weeks 1, 2, 4. Due to the unexpected death of the animals, between 16 to 19 animals survived at each assigned time point for laryngeal harvest and the subsequent flow cytometry analysis (**Table 2.2**).

2.4.3 Vocal Fold Cell Isolation

The mucosae of both sides of vocal folds were dissected and separated from the underlying thyroarytenoid muscles under a stereoscope. Vocal fold mucosal samples were pooled and subjected to single cell isolation. The strategy of sample pooling has been used for rat vocal fold cell and protein analysis considering the small size of rat vocal folds [84, 109]. Samples were dispersed into single cell suspensions using digestion, centrifugation and filtration steps [109]. First, dissected mucosa were placed in conical panels covered in aluminum foil and then incubated in Ca/Mg free DPBS solution (Mediatech, Cat#: 21-031-CV) with 0.05% collagenase (Gibco, Cat#: 17018-029) /0.001% DNAse I (Sigma Aldrich, Cat#: D4513) for 20 minutes at 37ºC to dissolve the extracellular matrix for cell release. The samples were thoroughly mixed and incubated again in 37ºC water bath. Once samples were visually confirmed to contain no large chunks of tissue, the solution was filtered with 40 nm cell strainers. Filtered samples were centrifuged at 290g for five minutes at 4ºC. After aspirating the supernatant, remaining cells were

suspended in HBSS (Corning, Cat#: 21-022-CV) from 1M HEPES solution with 2% fetal calf serum (HyClone, Cat#: SH30071.03) and 10nM HEPES (diluted from 1M HEPES solution, Corning, Cat#: 25-060-CI). Resulted single cell suspension samples were transferred to flow cytometry polystyrene tubes and centrifuged at 201g for 10 minutes at 4°C. After aspiration and suspension, the total cell number was determined with trypan blue staining and a hemacytometer. The number of isolated vocal fold cells ranged between 2.15 x 10^5 cells and 2.02 x 10^6 cells across time points (**Table 2.2**).

2.4.4 Sample Preparation for Flow Cytometry

Experimental Samples. Two independent flow cytometry panels (Panels A and B) were designed to cross-validate the results for cell identification and to evaluate if a more parsimonious flow panel would be sufficient to characterize cell populations. Panel A (**Table 2.3**) consisted of 11 parameters including FSC (cell size), SSC (cell granularity), one cell viability marker (AmCyan) and eight fluorescent cell surface markers (CD11b/c, CD29, CD44H, CD45, CD68, CD105, CD106 and His48). Panel B (**Table 2.4**) was composed of eight parameters including FSC, SSC, one cell viability marker (AmCyan) and five fluorescent cell surface markers (CD31, CD45, CD90, CD163 and His48). These specific cell surface markers were selected according to the literature of rat immunology (**Table 2.5** and **Table 2.6**). Pre-conjugated primary antibodies were used to facilitate specific affinity to surface antigens (see S2.1 and S2.2 Table for catalogue number and the fluorescence conjugate information). Isolated cells were first incubated in 1:100 diluted purified mouse anti-rat CD32 - FcγII blocker (Monoclonal D34-485, 0.5 mg/ml, BD) in staining buffer for 20 minutes at 4°C. This blocking step was required to prevent non-specific antibody

reagents to the Fc-receptor on cells such as monocytes and macrophages. Samples were then stained in 1:100 dilution of either eight (Panel A) or five (Panel B) preconjugated antibodies (**Table 2.5** and **Table 2.6**) with staining buffer for 30 minutes at 4^{o}C in a dark room. At the end, we collected cell type information across a total of 16 datasets (8 time points × 2 flow panels).

Control Samples. Unstained samples were used as negative controls that contained 5% FBS and DPBS without Ca/Mg ions. Samples were washed with DPBS without Ca/Mg ions twice and then stained with 1:1000 diluted fixable viability dye in DPBS without Ca/Mg ions for 30 minutes at 4^{o}C in a dark room. A fixable viability dye was used to exclude dead cells from the analysable population. UltraComp eBeads, which are beads conjugated with individual fluorochromes, were used as single-color controls for compensation setup to correct the spectral overlap. For the fixable viability dye and UltraComp beads, procedures were performed according to manufacturers. Samples were washed with staining buffer twice and then transferred to clear polystyrene flow cytometry tubes until analysis. Samples were read using BD FACSAria II (BD Bio sciences, California, USA) in the Maryland Pathogen Research Institute. Compensation steps were performed to correct spectral overlap before every run of the flow analysis [130, 131].

2.5 DATA PROCESSING AND ANALYSIS

2.5.1 Cell Population Analysis

Multiple markers were used for cell identification since no single surface marker is specific to the cells of interest. Two separate flow panels consisting of eight or five cell surface markers (CD markers) plus FSC, SSC and one cell viability marker were used to phenotype vocal fold cells as shown in **Table 2.5** and **Table 2.6**, respectively. The categorization of cells as neutrophils,

macrophages, endothelial cells and fibroblasts depending on marker expression was based on published literature [132-142]. Bivariate gating, an approach commonly used in flow cytometric analyses, was used primarily to analyse the multi-dimensional flow cytometry data [113, 119, 143-147].

2.5.2 Bivariate Gating Strategy

Live cells were categorized into different cell types and subtypes using a bivariate gating strategy (FlowJo software 10.0.7; LLC, Oregon, USA). Cell viability and compensation were applied during the setup of the experiment. For all datasets, gating analysis was performed by one individual (AG) who was blind to experimental conditions. Separate gating algorithms were developed for Panels A (**Figure 2.1**, **Table 2.5**) and B (**Figure 2.2**, **Table 2.6**) [132-142]. **Figure 2.3** shows the application of the gating strategy for Panel A from Day 2 data sample to further illustrate the concept.

The flowchart of gating strategy for Panel A (**Figure 2.1**) first used FSC-A vs SSC-A to represent the distribution of cells based on size, granularity and intracellular composition. These two scattering parameters led to the exclusion of debris, other non-cellular particles and lymphocytes [148, 149]. To exclude doublets that were considered as single cells, three tests were implemented in the following order: (1) FSC-W vs FSC-H (W=width; H=height) to select low FSC-W cells, (2) FSC-W histogram to check the threshold and (3) FSC-H vs FSC-A (A=area) to select cells that were clustered diagonally [150, 151]. A positive gating approach was used in which, instead of excluding negative cells (showing negative expression of a marker), priority was given to cells showing positive expression of a marker. The CD29 vs CD45 plot was used to

distinguish CD29+CD45+ hematopoietic cells (neutrophils and macrophages) from CD29+CD45- non-hematopoietic cells (endothelial cells and fibroblasts) [132, 133, 136-139]. Here CD29 not only separated hematopoietic cells from non-hematopoietic cells, but it was also used as a conventional marker to gate out erythrocytes. For the gating of hematopoietic cells, CD45+His48+ cells were selected as neutrophils and were further verified using a His48+CD11b/c+ gate (**Figure 2.1**) [141, 142]. From the same gate of hematopoietic cells, macrophages were identified by using CD106-CD44H+ and His48-CD68+ gates [132, 133, 138, 140]. In the case of non-hematopoietic cells (CD29+CD45-), CD106 was used to distinguish CD29+CD106+ endothelial cells from CD29+CD106- fibroblasts [132, 137]. Endothelial cells and fibroblasts were then confirmed by using CD44H+CD106+ and CD29+CD105+ gates, respectively [132, 133, 137, 139].

Regarding Panel B (**Figure 2.2**), FSC-A vs SSC-A and doublet exclusion tests were used in a similar way as for Panel A. CD90 was used with FSC-A to separate CD90-FSC-A+ hematopoietic cells from CD90+FSC-A+ non-hematopoietic populations [132, 133, 137, 139]. CD31 was used to confirm the population of hematopoietic cells and to separate non-hematopoietic cells into endothelial cells and fibroblasts [132, 133, 137]. His48 was used to separate His48+CD31+ neutrophils from His48-CD31+ macrophages by using a His48 vs CD31 gate [141, 142]. CD45 and CD163 were used to confirm populations of neutrophils and macrophages, respectively [132, 133, 136-139].

2.5.2.1 Cell Subtype Analysis

Macrophages and fibroblasts were further separated into distinct subtypes as indicated by distinctive expression patterns of proposed flow markers. In Panel A (**Figure 2.1**), CD68 and

CD11 were used together to distinguish between two subtypes of macrophages, namely pro-inflammatory macrophage M1 (CD11b/c++CD68++) and anti-inflammatory macrophage M2 (CD11b/c+CD68+) [152-154]. In addition, FSC-A was used to discriminate fibroblast subtypes based on the cell size: CD105+FSC-A+ as fibroblast Type I and CD105+FSC-A++ as fibroblast Type II [155]. In the case of Panel B (**Figure 2.2**), CD163+ and CD163++ were used to discriminate between macrophages M1 and M2, respectively [156], whereas CD90 was used along with FSC-A to distinguish fibroblast subtypes.

2.5.2.3 Thresholding and Backgating

Multiple plots and parameters were used to decide the threshold limit in the generation of gates and to verify gate positions (**Figure 2.4A**). Contour and density plots (**Figure 2.4A (iii) and (iv)),** which show expression levels and relative density of data, are commonly used in placing the gates [145, 157]. Backgating was used to verify the gate positions (**Figure 2.4B**). Backgating not only helped to analyse cells identified in a gate on dot plots with different parameters but also showed the final gated population within the population of its ancestors. The same gating strategy was applied across all eight time points within the same panel to compute the percentage of each cell type in the total cell population.

2.5.3 Statistical Analyses

Mixed effects models and correlation analyses were used to evaluate the degree of similarity in results from Panels A and B. Distinct mixed effects models were used to assess variation between panels for cell types (neutrophils, macrophages, endothelial cells and fibroblasts) and for subtypes (M1 and M2 macrophages, and Type I and II fibroblasts). Density data for a particular cell type or

subtype (i.e., % of cells in total cell population) at each time point was obtained from one flow cytometry run. To analyse the effect of flow panel on estimates of cell density, we used the data for each of the eight time points as independent data points (i.e., time not included in the model; n=8 for each panel). We ran a full-factorial model with flow panel (A vs. B) and cell type (or subtype) as the independent variables, which allowed us to analyse the effect of panel simultaneously across cell types (or subtypes). Because each flow cytometry run generated data for each cell type (or subtype), the identity of each flow cytometry run was included as a random variable for the mixed effects model. Pearson's correlations were used further to analyse the relationship between the results from Panel A and B, and to complement the results from mixed effects models.

2.6 RESULTS

Across both panels, flow cytometric analyses revealed variations in vocal fold cellular composition following injury (**Figure 2.5A and B; Table 2.7 and S2.3 Table**). Across all cell types, data from Panels A and B (i.e., two types of analyses) were not significantly different from each other (mixed effects model: $F_{1,14}$=0.4, p=0.5630) and significantly positively correlated with each other (Pearson's correlation: $p<0.01$ for all pairwise correlations). Therefore, for the final examination of changes to cell types across time, we averaged the results from the two panels (**Figure 2.5**C).

In uninjured controls, neutrophils, macrophages, endothelial cells and fibroblasts, respectively, represented 7.70%, 4.70%, 9.54% and 53.49% of the total cell population. In surgically injured vocal folds, fibroblasts also appeared as the prevalent cell type (>50%) among the four cell types at all time-points except Day 2 and Day 3. This result is consistent with results

from the mixed effects model, wherein the effect of cell type was significant ($F_{3,42}$=59.3, $p<0.0001$) and was driven by the fact that fibroblasts were more abundant than any other cell type analysed (Tukey's HSD, $p<0.05$). No significant differences were found in cell density among the remaining cell types. Neutrophils were ranged from 2.31% to 14.37% on average throughout the examined time course. Macrophages appeared as the most dominant cell type (~33%) on Day 2. Shortly after, both neutrophils and macrophages were found in less than 5% of the total cell populations. The population of endothelial cells was below 5% in injured vocal folds on average except a relatively sharp increase during Week 2 (14.10%).

Across fibroblast types I and II cells as well as M1 and M2 cells, results from the gating analyses for Panels A and B were not significantly different ($p>0.8$ each for both fibroblast and macrophage subtypes) and significantly correlated with each other (Pearson's correlation: $p<0.05$ for each subtype). From the mixed effects model analyses, we also observed that M1 cells were, overall, more abundant than M2 cells ($F_{1,14}$=6.1, $p=0.0275$) but that type I and II fibroblasts were not different in abundance. As such, data from Panels A and B were, again, averaged in the analysis of temporal dynamics of subtypes (**Figure 2.6**). Whereas the density of M2 macrophages showed minimal changes following vocal fold injury (ranged from 0.90% to 2.97% across time points), the density of M1 macrophages dramatically changed following injury. In particular, M1 density peaked two days after injury (29.91%) and returned to baseline level within five days post-injury. In contrast, both fibroblast subtypes showed dynamic changes over the time course of the study (ranging from 3.54% to 42.18%), albeit with slightly different profiles.

2.7 DISCUSSION

2.7.1 Neutrophils and Macrophages

In this study, multi-parametric flow cytometry was used to analyse dynamic changes to cell composition of vocal folds up to four weeks following injury. Our results (**Figure 2.5C**) are generally consistent with the temporal dynamics of immune cells (neutrophils and macrophages) known in general wound healing literature. In dermal wound healing, neutrophils arrive at the wound site in the first few hours, peak in abundance one day after the injury, and reduce rapidly by the third day after injury [78, 82, 83, 158-161]. Macrophages peak slightly later, by the second day after the injury, but also demonstrate rapid decreases on the third day after surgery [78, 83, 158, 159]. Given the similarities in the temporal dynamics of neutrophil and macrophage changes following injury in vocal folds and other types of tissue, comparable cellular functions of immune cells underlying the inflammation and repair processes are speculated.

For instance, our results showed that neutrophils and macrophages arrived at the wound site within the first three days after injury (**Figure 2.5C**) [78, 82, 83, 158-161], representing the phase of acute inflammation [162, 163]. Activated neutrophils and macrophages carry out anti-bacterial functions and phagocytose bacteria and cell debris, and use free oxygen radicals to absorb the waste. A rapid increase in neutrophils was found on Day 1 (**Figure 2.5C**) followed by a sharp decline on Day 3 (**Figure 2.5C**). The decline might be due to their apoptosis and phagocytosis by macrophages and other immune cells in the wound [78, 164]. The depletion of neutrophils is also necessary to help the transition from acute inflammation to the sub-acute and repair phases after injury [165]. Further, our results showed that the percentage of macrophages increased from

12.81% to 32.88% between Day 1 and Day 2. When monocytes arrive at the wound area, cells differentiate into tissue macrophages that take over the phagocytosis. As proposed for other tissues, autocrine signaling contributes to the dominant presence of macrophages during the early stage of wound healing [82, 160, 164]. Macrophages secrete reactive oxygen species [166] as well as various chemokines such as platelet-derived growth factor, tumor necrosis factor alpha, interleukin 6, granulocyte colony-stimulating factor and granulocyte macrophage colony-stimulating factor that attract additional macrophages from the neighborhood to the wound area [82, 160, 164].

2.7.2 Endothelial Cells

In addition to immune cells, the temporal pattern of endothelial cells (**Figure 2.5C**) following vocal fold damage also resembles the general wound healing literature [82, 160]. In our study, endothelial cells contributed about 9% of the total cell population in uninjured controls that were likely originated from the endothelium layer of undisturbed blood capillaries in native vocal fold mucosae. A rise in the endothelial cells population was observed in Week 2 after surgery (**Figure 2.5C**), representing about 14% of total cell populations. Our results suggested an active angiogenesis might have started between Week 1 and Week 2 post surgery. To our best knowledge, this study is the first to evaluate the population of endothelial cells in vocal fold injury and healing. Further investigation on the precise role of endothelial cells, their interaction with other cell types as well as their implications in vocal fold scarring is warranted.

2.7.3 Fibroblasts

As reported in the wound healing literature, fibroblasts normally arrive at the wound site around Day 3 and start the proliferative phase [78, 82, 110, 160]. These cells usually reach their maximum

concentrations between Day 5 and Day 7, and start to decrease gradually by the end of Week 1 [78, 83, 158, 159]. Interestingly, our data (**Figure 2.5C**) showed that fibroblasts were predominantly present in injured vocal folds spanning from the early acute inflammatory to later remodeling phases of wound healing. Previous studies reported the abundant presence of fibroblasts up to one week after surgical vocal fold injury [18, 109, 111]. Our data suggests an abundance of fibroblasts in the wound site up to four weeks after surgery, which confirms the important role of fibroblast in the wound remodeling of vocal folds. Fibroblasts persisted as the dominant cell type in acute injured vocal folds (Day 1: 53.81%; Day 2: 29.37%) despite the infiltration of neutrophils and macrophages during that time window. Our previous work showed that both macrophages and fibroblasts were the major cell source of DAMP, high mobility group box-1, in modulating the inflammatory cytokine production in acute vocal fold injury [29, 84]. Our data and others collectively suggest immunological and repair functions of fibroblasts that are unique in vocal folds [167, 168].

2.7.4 Putative Macrophage and Fibroblast Subtypes

Our gating analyses suggested the presence of putative macrophage and fibroblast subpopulations in native and injured vocal folds. In uninjured vocal folds (Day 0), macrophages M1 and M2 represented about 2-3% of the total cell population. After the injury, the population of M1 peaked at Day 2 (~30%) and M2 stayed relatively stable (1-2%) throughout the examined time course (**Figure 2.6A**). We speculate that M1 were classically activated macrophages involved in phagocytic activities and inflammation at the acute phase (i.e., Day 2) whereas M2 were alternatively activated macrophages involved in cell proliferation and repair activities [30, 152, 169]. Although M2 appeared as a minor population in vocal folds, their presence in native vocal

folds might suggest ongoing repair activities to maintain vocal fold hemostasis for daily mechanical and chemical challenges. Two fibroblast-like populations, CD105+FSC-A+ (fibroblast type I) and CD105+FSC-A++ (fibroblast type II), were identified in our flow data (**Figure 2.6B**). The population of CD105/FSC-A++ would likely be myofibroblasts known in the wound healing literature [82, 155, 170-173]. Myofibroblasts are commonly found during the tissue remodeling phase to contract the wound and synthesize extracellular matrix given their contractile and secretory properties [174]. In uninjured vocal folds, fibroblast Type I were found to be higher in population as compared to Type II (**Figure 2.6B**). Following injury, these two populations showed an oscillatory function in terms of their population (**Figure 2.6B**). One possible explanation of this oscillation is due to the transdifferentiation of fibroblasts and myofibroblasts in response to dynamical changes in surrounding cytokine stimulants and the extracellular matrix environment [29, 84, 170, 171, 175-177]. The oscillatory result suggested that vocal fold fibroblasts could be highly sensitive to chemical and mechanical stimuli in switching their phenotypes to myofibroblasts; and vice versa. Further, in our previous study [29], myofibroblasts were barely detected in injured vocal fold lamina propria using immunohistochemistry (IHC). One possible reason was that alpha smooth muscle actin (α-SMA) was used as the IHC marker for myofibroblasts previously. α-SMA, however, would need to be fully incorporated into actin stress fibers intracellularly to be visibly observed. Our results suggest that flow cytometry might be more sensitive to detect the presence of vocal fold myofibroblasts using CD105+FSC-A++ as a marker compared to the IHC approach. Further functional studies are necessary to confirm if CD105+FSC-A++ cells behave as typical myofibroblasts known in the literature. In addition, further investigation related to the oscillating dynamics of fibroblast-myofibroblast

transdifferentiation may reveal unknown signaling pathways and cell-ECM interactions that are specific to the vocal folds microenvironment. Such information will provide insights that may help develop effective treatment strategies to control the fibrotic activity in vocal fold injuries.

2.7.5 Study Limitations and Conclusion

In this study, vocal fold samples were pooled from multiple animals to ensure a sufficient cell number to detect any small percentages of cell subpopulation. This biological sample pooling however resulted in a reduction of the sample size for each time point, limited the information on individual variation and decreased statistical power. As a result, this sample pooling limited the possibility of statistical evaluation of time effects. Nevertheless, efforts were made to verify the speculated time-varying dynamics of the cell population. First, cross-platform verification and analysis were performed with the application of two independent flow panels. Robust patterns of cell dynamics across time were observed in both Panel A and Panel B (Figure 5) and no statistical differences were noted in cell density between the two panels for all time points. Second, additional cell samples were obtained from two independent animal pools at Day 2 following surgery. By applying the same gating strategy of Panel A, the two sample pools showed comparable percentages of cell populations (Table S2.4). Plausible confounding factors, such as sample variability (animal heterogeneity) and technical variability (surgical procedures and sample preparation), were thus considered to be reasonably controlled in this study. In other words, variations across time points observed in the datasets could be likely explained by the effect of time. Larger animals such as pigs can be considered for future studies to minimize the need of sample pooling for vocal fold cell phenotyping work. In addition, computational models have been recommended to reduce the reliance on animal and human data to complement empirical

investigation [178, 179]. Results from this study will be subjected to our ongoing work in the development of computational models that numerically simulate the cellular and molecular response to vocal fold surgical injuries [46, 66, 180-183].

Recent studies have shown the important role of epithelial cells in vocal fold wound healing [184-188]. Given the small size of rat vocal folds, it was impossible to precisely dissect the epithelial layer out from the lamina propria for this flow cytometry analysis. Antibodies used in the current flow panels were thus carefully selected to ensure no immunoreaction with epithelial cells [133]. In future work, additional fluorescent cell surface markers will be required to identify epithelial cells because the parameters of SSC and FSC are not accurate enough to separate epithelial cells from others. Based on our results, Panel A (11 parameters) and Panel B (8 parameters) showed similar cell populations and their density. If the source of tissue is a limiting factor in future studies, the more parsimonious flow panel with eight parameters would be recommended for expansion to discriminate epithelial cells and others in vocal folds.

A multi-parametric flow cytometry study was used to phenotype cell populations in rat vocal folds following surgical injury. Precise identification of cell phenotypes involved in vocal fold injury is fundamental in understanding the pathogenesis of vocal fold scarring. These findings will also assist in designing more precise treatment strategies to target specific cell populations and timing of application in minimizing iatrogenic scarring following vocal fold surgery.

2.8 ACKNOWLEDGEMENTS

We would like to acknowledge Dr. Susan Thibeault, Dr. Suzanne King, Dr. Martin Richer, Dr. David Mosser and his PhD candidate student, Rahul Suresh, for technical assistance and advice on

flow cytometry, as well as Dr. Douglas Powell for providing trainings for the animal work. This study was supported by National Institute of Deafness and other Communication Disorder of the National Institutes of Health under awards number R03DC012112 (PI: Li-Jessen) and R01DC005788 (PI: Mongeau). All authors read and approved the final manuscript. We declare that the authors have no conflict of interest.

2.9 TABLES

Table 2.1: Summary of Vocal Fold Cellularity in Literature.

Study	Human/ Animals	Methods to Cell Detection	Summary
Boseley et al., 2006 [27]	Humans (ages 11-73 years)	H&E	• Location of vocal fold included SLP, ILP and DLP. • Macrophages and myofibroblasts were found predominantly in the SLP.
Branski et al., 2005 [111]	Female white rabbits	MTS	• Study time-points included 12 hours and 1, 3, 5, 7, 10, 14 and 21 days post-injury. • Location of vocal fold included EPI, SLP, ILP, DLP and TA. • Fibroblasts were found maximum at Day 3 post-injury.
Catten et al., 1998 [28]	Humans (ages 2 days - 14 years)	ICC	• Location of vocal fold included SLP, ILP and DLP. • Macrophages and myofibroblasts were found predominantly in the SLP. • Fibroblasts were found predominantly in the DLP.
King et al., 2015 [30]	Female Landrace pigs	FC, H&E and IHC	• Study time-points included 1, 3, 5, 7 and 23 days post-injury. • Location of vocal fold included SLP. • Macrophages were found maximum at Day 5 and Day 23 in vocal fold post LPS and surgical injury, respectively. • Neutrophil-like cells were found maximum at Day 1 and Day 3 in vocal fold post LPS and surgical injury, respectively.
Ling et al., 2009 [108]	Male Sprague–Dawley rats	H&E	• Study time-points included 1, 3, 5 and 7 days post-injury. • Location of vocal fold included EPI, SLP, ILP, DLP and TA. • Neutrophil-like cells were found maximum at Day 1. • Neutrophil-like cells, epithelial cells and fibroblast-like cells were recruited sequentially at the wound site.
Ling et al., 2010 [109]	Male Sprague–	FC, ICC and IHC	• Study time-points included 1, 3, 5, and 7 days post-injury.

	Dawley rats		• Location of vocal fold included EPI, SLP, ILP, DLP and TA. • Fibroblasts were found uniformly distributed in the lamina propria.
Muñoz-Pinto et al., 2009 [107]	Humans (ages 2-94 years)	PDA	• Location of vocal fold included EPI, SLP, ILP and DLP. • The mean cell density of EPI and LP was 0.57 million cells per milligram of tissue total protein.
Tateya et al., 2006 [18]	Male Sprague-Dawley rats	IHC	• Study time-points included 1, 3, 7 and 14 days post-injury. • Location of vocal fold included ILP. • Fibroblasts were found maximum at Day 3.

Methods to Cell Detection: ICC: Immunocytochemistry, IHC: Immunohistochemistry, FC: Flow Cytometry, H&E: Hematoxylin and Eosin Stain, MTS: Masson's Trichrome Staining, PDA: PicoGreen DNA Assay. Location of vocal fold – EPI: Epithelium, SLP: Superficial Lamina Propria, ILP: Intermediate Lamina Propria, DLP: Deep Lamina Propria, TA: Thyroarytenoid Muscle.

Table 2.2. Number of Rats Sacrificed and Cells Obtained from Vocal Folds at Each Study Time Point.

Time-point	Number of Rats Sacrificed	Total Number of Cells Isolated
Day 0 (Uninjured controls)	20	2.15×10^5
Day 1	17	4.16×10^5
Day 2	16	2.02×10^6
Day 3	18	4.16×10^5
Day 5	17	3.88×10^5
Day 7	18	2.97×10^5
Week 2	17	2.24×10^5
Week 4	19	2.22×10^5

Table 2.3. List of Markers and Parameters in Panel A and Their Corresponding Biological Functions.

	Parameters	Significance	References
1	CD11b/c	CD11b/c is involved in adhesion activities of leukocytes including granulocytes, monocytes and macrophages. CD11b/c plays an important role in chemotaxis and apoptosis. CD11b/c can also be used as a marker to discriminate macrophage subtypes in the study of functional heterogeneity of macrophages.	[133, 134, 189]
2	CD29	CD29 is a member of the integrin family that plays an important role in cell-cell or cell-matrix interaction. CD29 binds to extracellular matrix proteins including collagen, laminin, fibronectin and vitronectin. During inflammation, CD29 helps neutrophils migrate to the wound site. Other functions of CD29 include cell adhesion, signal transduction and cell differentiation.	[133, 190, 191]
3	CD44H	CD44H acts as cell adhesion receptors. Hyaluronate has the ligand of CD44H. CD44H also acts as regulators of cell migration, cell-to-cell and cell-to-substrate interactions.	[192, 193]
4	CD45	CD45 is the primary surface marker to distinguish between hematopoietic and non-hematopoietic cells. CD45 helps in controlling the signals originating from cytokine and integrin receptors. CD45 also plays an important role to regulate B-cell and T-cell antigen receptor signaling, cell growth and cell differentiation.	[133, 194]
5	CD68	CD68 mediates the process of phagocytosis for macrophages. CD68 helps in both intracellular and extracellular activities like lysosomal metabolism, cell-to-cell and cell-to-pathogen interactions. The expression of CD68 on macrophages and monocytes is mostly cytoplasmic.	[140, 195]
6	CD105	CD105 acts as a regulator of angiogenesis and neovascularization, and facilitates the binding of endothelial cells to integrins. The expression of CD105 results in the cytoskeletal reorganization that affects cell morphology and migration. During the process of inflammation and healing, the expression of CD105 is enhanced on activated endothelium in tissues that undergo angiogenesis.	[196, 197]
7	CD106	CD106 mediates cell adhesion of leukocytes such as lymphocytes and monocytes to activated endothelium and functions in leukocyte-endothelial cell signal transduction. The expression of CD106 is enhanced in endothelial cells under the stimulation of inflammatory cytokines.	[198-200]

8	His48	His48 has been shown to react with monocytes and granulocytes via an antigen molecule which is expressed on their surface. His48 is mainly expressed by neutrophils and used as a marker to distinguish neutrophils from other cell populations. His48 is also commonly used in combination with other surface markers (such as CD11, CD45, CD68 etc.) to identify granulocytes.	[141, 142]
9	Cell Viability	To distinguish between live and dead cells.	[201]
10	FSC	Forward-scattered light (FSC) reflects the cell-surface area or size.	[149]
11	SSC	Side-scattered light (SSC) reflects the cell granularity or intracellular complexity.	[149]

Table 2.4. List of Markers and Parameters in Panel B and Their Corresponding Biological Functions.

	Parameters	Significance	References
1	CD31	CD31 is also known as platelet-endothelial cell adhesion molecule-1 (PECAM-1). CD31 plays a major role in cell-cell and cell-matrix interactions and signal transduction. CD31 mediates in both homotypic and heterotypic cell adhesion by binding to either itself or the leukocyte integrin αvβ3. CD31 also plays a role in neutrophils recruitment, transendothelial migration of leukocytes, vasculogenesis, angiogenesis, integrin activation as well as in cardiovascular development.	[202-204]
2	CD45	CD45 is the primary surface marker to distinguish between hematopoietic and non-hematopoietic cells. CD45 helps in controlling the signals originating from cytokine and integrin receptors. CD45 also plays an important role to regulate B-cell and T-cell antigen receptor signaling, cell growth and cell differentiation.	[133, 194]
3	CD90	CD90 interacts with CD45 and regulates the vascular permeability during the process of inflammation. Most peripheral T cells, fibroblasts, thymocytes and endothelial cells express CD90 on their cell surface. Other functions include differentiation of hematopoietic stem cells, proliferation and activation of lymphocytes, and adhesion of thymocytes.	[205, 206]
4	CD163	CD163 acts as a scavenger receptor for both hemoglobin and hemoglobin-haptoglobin complex. CD163 is exclusively expressed by most of the subtypes of macrophages and mediates the activation of macrophages during inflammation.	[207-209]
5	His48	His48 has been shown to react with monocytes and granulocytes via an antigen molecule which is expressed on their surface. His48 is mainly expressed by neutrophils and used as a marker to distinguish neutrophils from other cell populations. His48 is also commonly used in combination with other surface markers (such as CD11, CD45, CD68 etc.) to identify granulocytes.	[141, 142]
6	Cell Viability	To distinguish between live and dead cells.	[201]
7	FSC	Forward-scattered light (FSC) reflects the cell-surface area or size.	[149]
8	SSC	Side-scattered light (SSC) reflects the cell granularity or internal complexity.	[149]

Table 2.5. Rat Cell Surface Marker Profile for Flow Cytometry in Panel A.

Marker	Fluorochrome	Neutrophil	Macrophage	Endothelial Cell	Fibroblast	References
CD11b/c	FITC	+	+	-	-	[132-135]
CD29	PE-Cy7	+	+	+	+	[132, 133, 136, 137]
CD44H	APC-Cy7	-	+	+	+	[132, 133, 137]
CD45	PerCP-Cy5.5	+	+	-	-	[132, 133, 136-139]
CD68	PE-Texas Red	+	+	-	+	[132, 133, 138, 140]
CD105	PE	-	+	+	+	[132, 133, 137, 139]
CD106	Brilliant Violet 421	-	-	+	-	[132, 137]
His48	APC	+	-	-	-	[141, 142]
Cell Viability Dye	AmCyan	+	+	+	+	[201]

"+" shows positive expression and "-" shows negative expression

Table 2.6. Rat Cell Surface Marker Profile for Flow Cytometry in Panel B.

Marker	Fluorochrome	Neutrophil	Macrophage	Endothelial Cell	Fibroblast	References
CD31	APC	+	+	+	-	[132, 133, 137]
CD45	PerCP-Cy5.5	+	+	-	-	[132, 133, 136-139]
CD90	FITC	-	-	+	+	[132, 133, 137, 139]
CD163	PE-Cy7	-	+	-	-	[132, 133, 139]
His48	PE	+	-	-	-	[141, 142]
Cell Viability Dye	AmCyan	+	+	+	+	[201]

"+" shows positive expression and "-" shows negative expression.

Table 2.7. Gating Results.

Panel	Time	Neutrophil	Macrophage	Endothelial Cell	Fibroblast	Fibroblast I	Fibroblast II	M1 Macrophage	M2 Macrophage
A	Day0	7.14	4.57	9.18	51.32	37.83	13.49	2.09	2.44
A	Day1	13.53	11.22	3.19	56.23	30.99	25.24	8.87	2.35
A	Day2	11.29	31.68	1.93	31.13	3.24	27.89	29.23	2.45
A	Day3	7.68	9.41	2.18	20.03	9.11	10.92	7.8	1.61
A	Day5	2.31	4.18	3.3	55.12	34.93	20.19	3.25	0.94
A	Day7	2.16	3.62	3.13	62.55	20.96	41.58	2.03	1.58
A	Week2	2.53	2.92	13.46	44.27	27.45	16.82	1.59	1.33
A	Week4	2.89	3.35	4.87	63.79	29.07	34.72	1.25	2.11
B	Day0	8.25	4.84	9.91	55.65	39.24	16.41	3.17	1.67
B	Day1	15.21	14.4	6.44	51.4	24.32	27.08	11.67	2.73
B	Day2	14.04	34.07	1.61	27.6	3.84	23.76	30.59	3.48
B	Day3	8.55	10.7	2.32	20.78	10.12	10.66	8.04	2.66
B	Day5	2.84	4.92	2.6	50.83	30.88	19.95	4.06	0.86
B	Day7	2.46	4.11	4.5	61.37	18.6	42.77	2.66	1.45
B	Week2	2.62	2.4	14.75	65.84	41.46	24.38	1.81	0.59
B	Week4	3.29	3.9	5.7	61.51	25.44	36.07	1.8	2.1

The number represents the percentage of the cell population.

2.10 FIGURES

Figure 2.1. Flowchart of Gating Strategy for Panel A

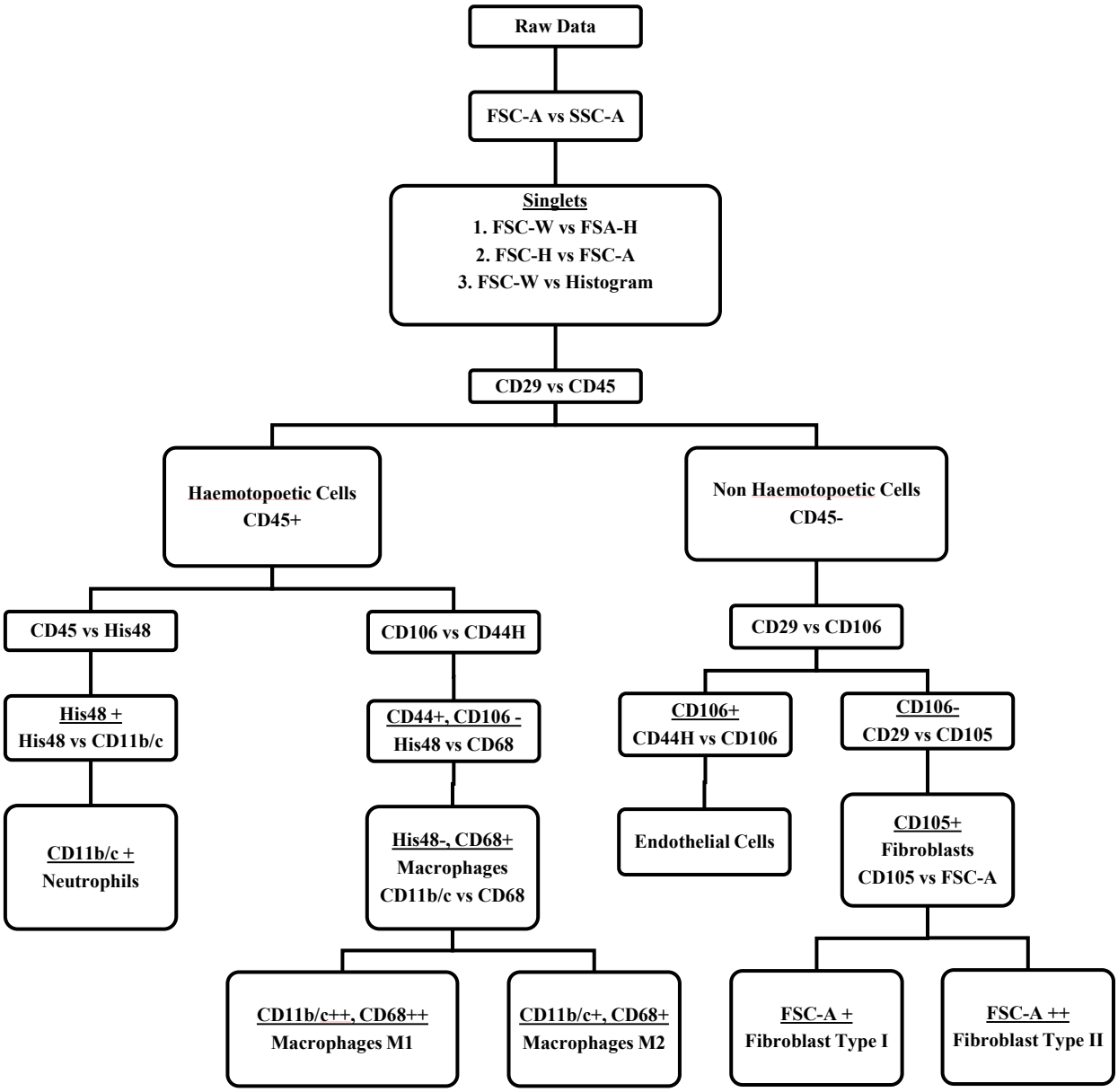

Figure 2.2. Flowchart of Gating Strategy for Panel B.

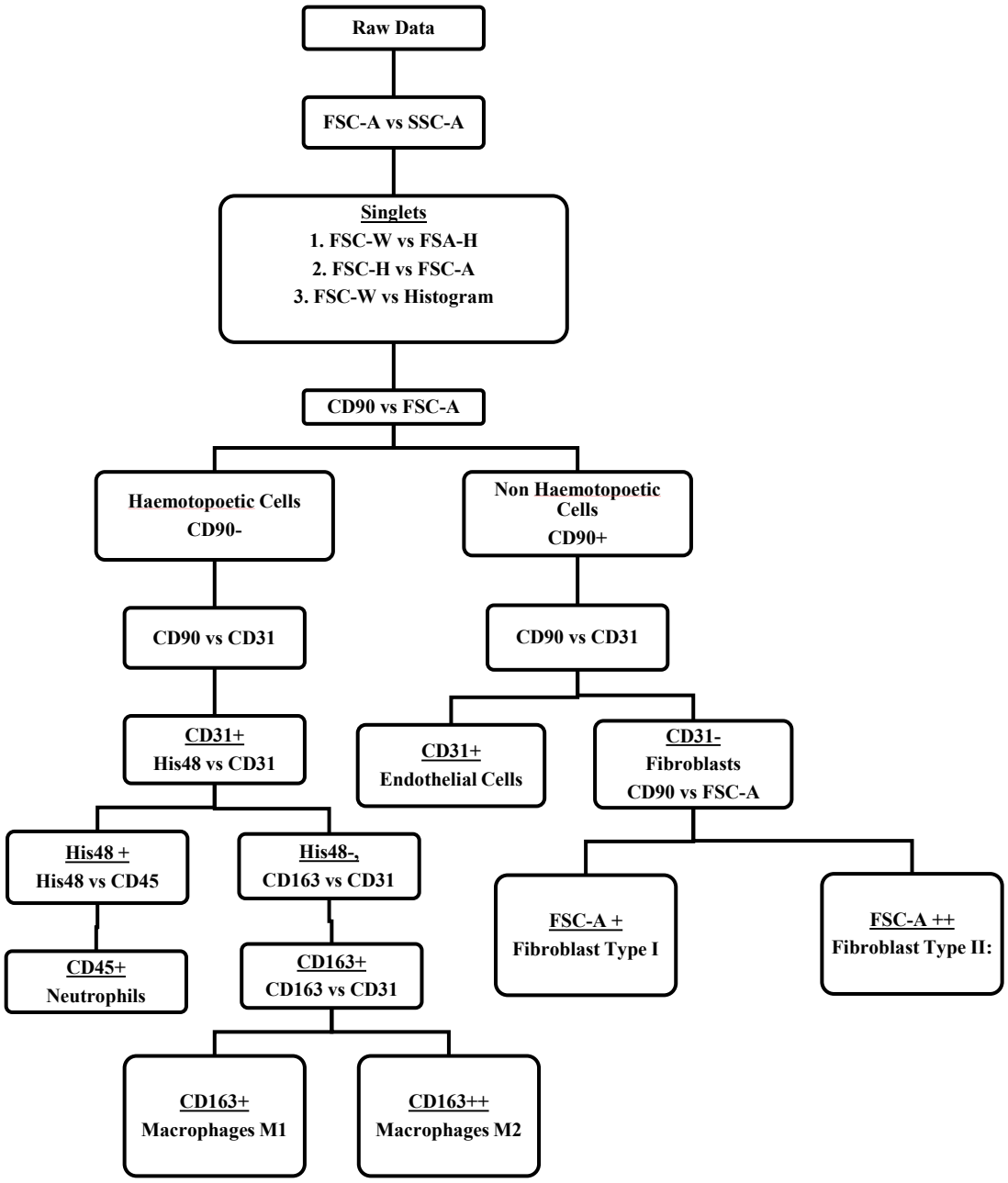

Figure 2.3. Example of Gating Strategy for Panel A from Day 2 Sample. First FSC-A vs SSC-A were used for the exclusion of debris, other non-cellular particles and lymphocytes. Three tests (FSC-W vs FSC-H to select low FSC-W cells, FSC-W histogram to check the threshold and FSC-H vs FSC-A to select cells that were clustered diagonally) were implemented to exclude doublets that were considered as single cells. The CD29 vs CD45 plot was used to separate CD29+CD45+ hematopoietic cells from CD29+CD45- non-hematopoietic cells. For the hematopoietic cells, CD45+His48+ cells were selected as neutrophils and were further verified using a His48+CD11b/c+ gate, and macrophages were identified by using CD106-CD44H+ and His48-CD68+ gates. In the case of non-hematopoietic cells, CD106 was used to distinguish CD29+CD106+ endothelial cells from CD29+CD106- fibroblasts. Endothelial cells and fibroblasts were then confirmed by using CD44H+CD106+ and CD29+CD105+ gates, respectively. CD68 and CD11 were used together to distinguish between two subtypes of macrophages, namely M1 (CD11b/c++CD68++) and M2 (CD11b/c+CD68+). In addition, FSC-A was used to separate fibroblast subtypes based on the cell size: CD105+FSC-A+ as fibroblast Type I and CD105+FSC-A++ as fibroblast Type II.

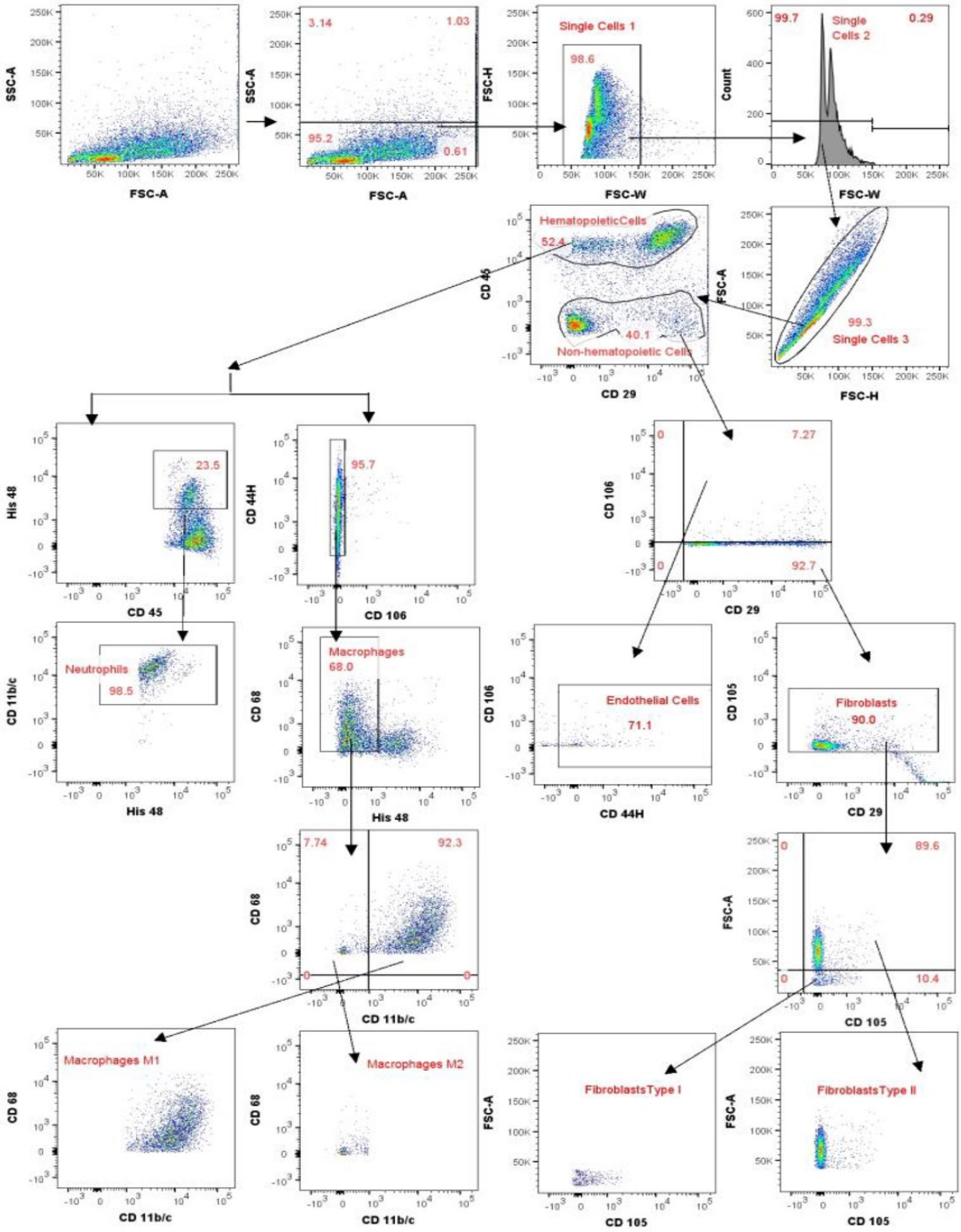
SSC-A
FSC-A
3.14
1.03
95.2
0.61
FSC-H
Single Cells 1
98.6
FSC-W
Count
99.7
Single Cells 2
0.29
HematopoieticCells
52.4
CD 45
CD 29
40.1
Non-hematopoietic Cells
99.3
Single Cells 3
His 48
23.5
CD 44H
95.7
CD 106
7.27
92.7
Neutrophils
98.5
CD 11b/c
Macrophages
68.0
CD 68
Endothelial Cells
71.1
CD 105
Fibroblasts
90.0
7.74
92.3
89.6
10.4
Macrophages M1
Macrophages M2
FibroblastsType I
FibroblastsType II

Figure 2.4. Verification of Gating Strategy. (A) Various plots were used for verification: (i) Original plot, (ii) Smoothing curve, (iii) Contour plot, (iv) Density plot, (v) Zebra Plot and (vi) Histogram. (B) Backgating for neutrophils. This dataset is the same as that shown in Figure 2.3. Here, the final gated population is overlayed on each gating step as red dots on the dot plot.

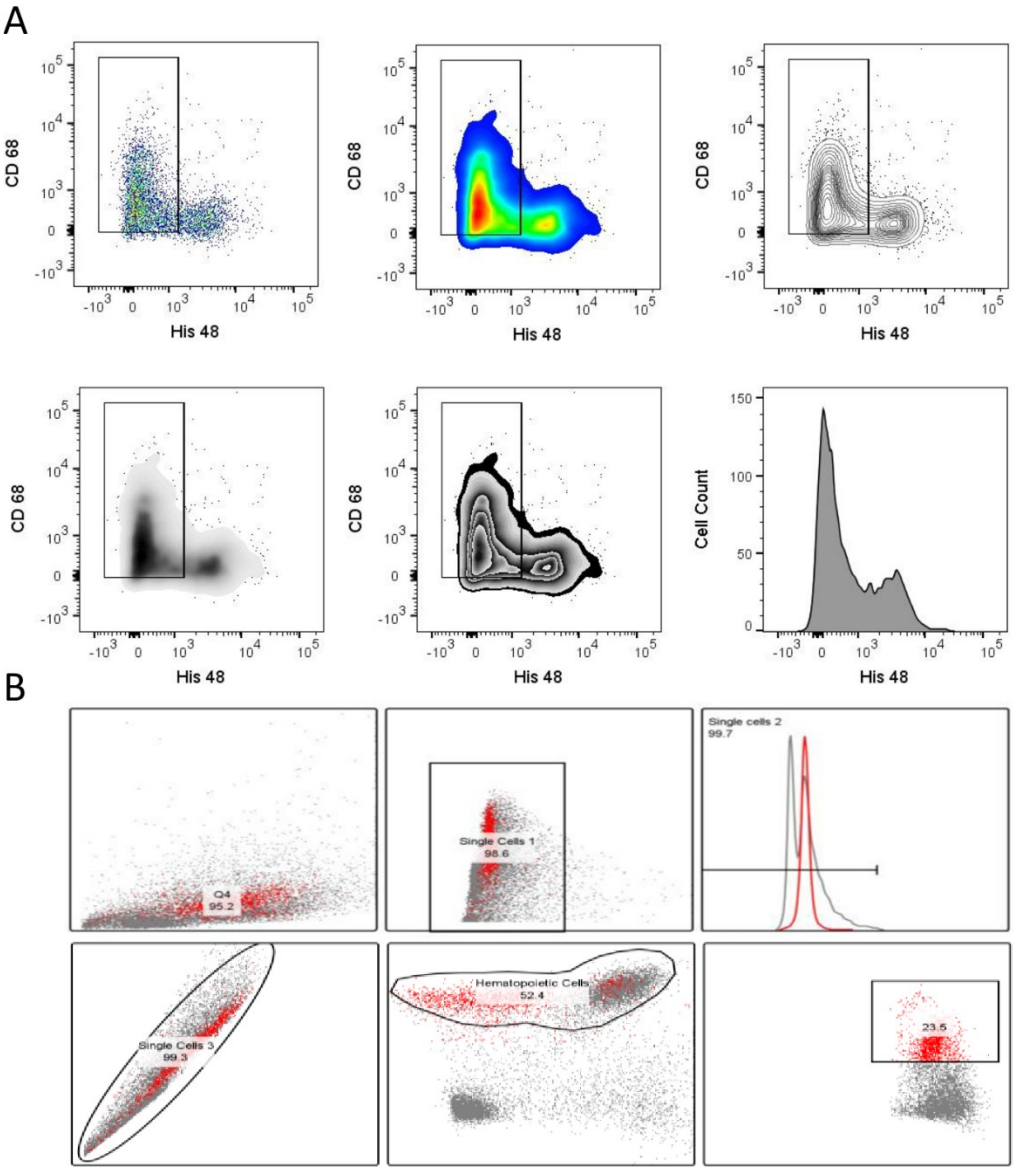

Figure 2.5. Percentage of each cell type over time in Panel A and B with gating method. Behaviour of four cell types in two different panels: (A) Panel A and (B) Panel B. (C) Combination of two panels listed above in one curve.

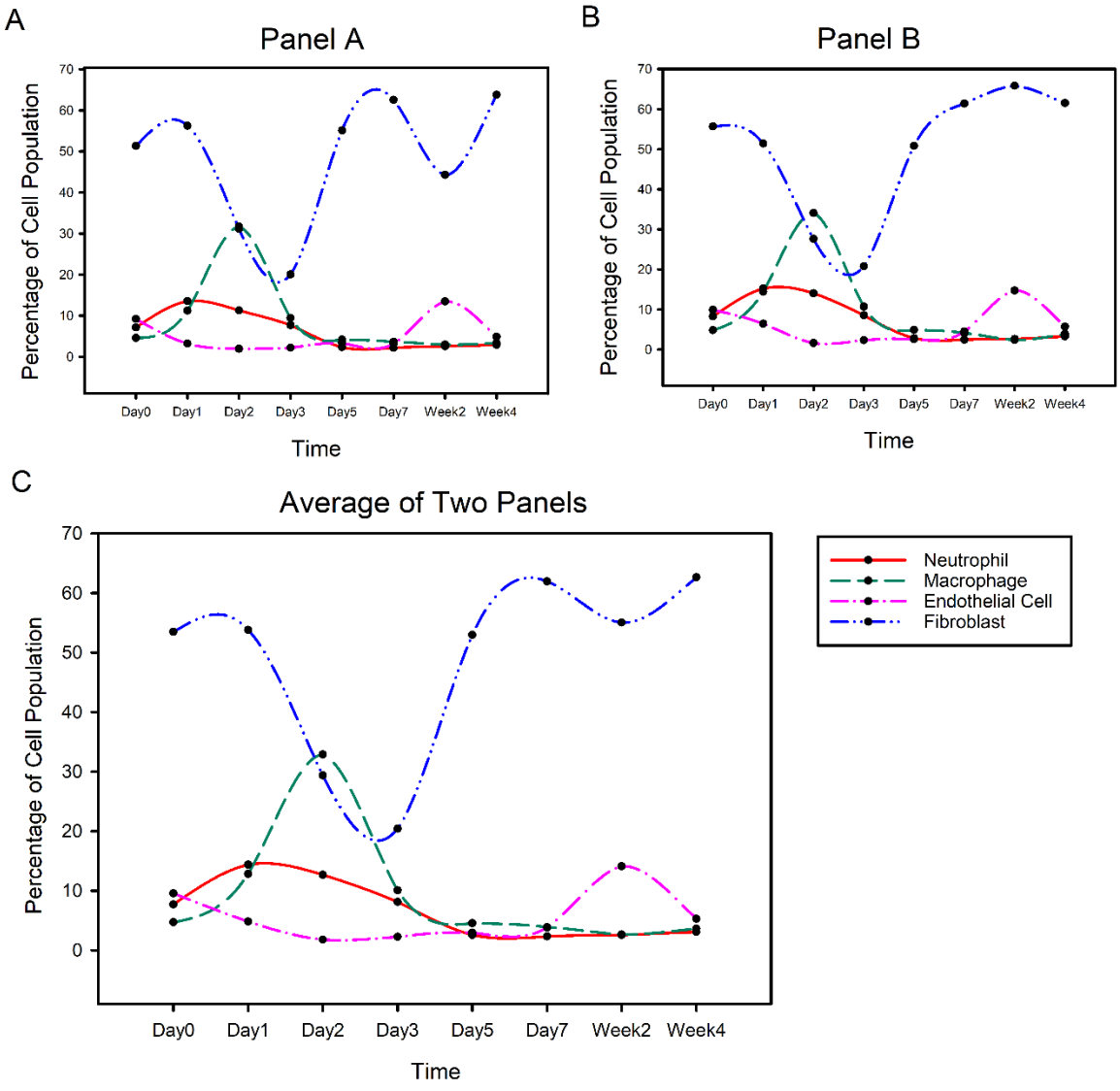

Figure 2.6. Cell Subtypes Analysis. (A) Macrophages Subtypes M1 and M2. (B) Fibroblast Subtypes Type I and Type II.

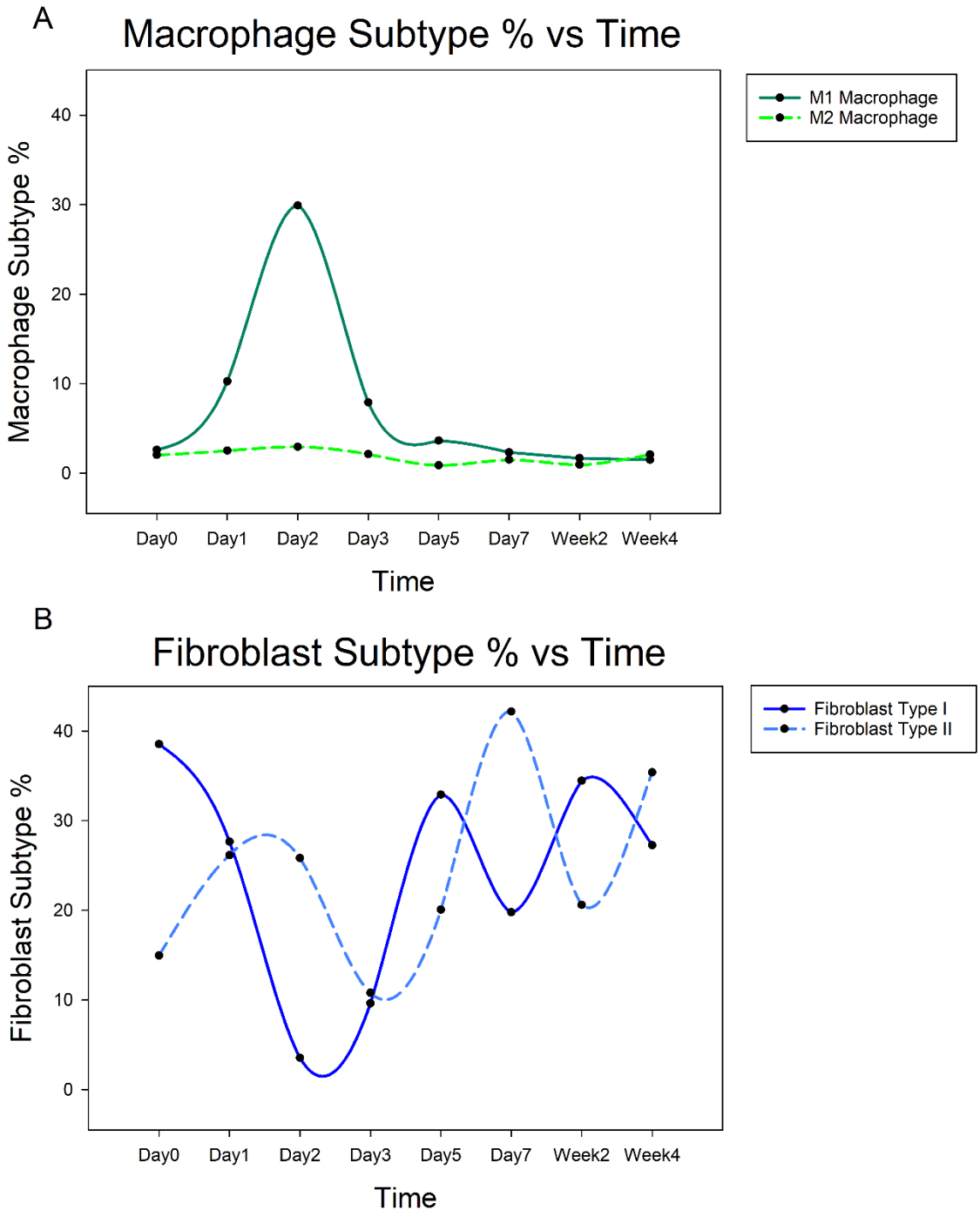

2.11 SUPPORTING INFORMATION

S2.1 Table: **Laser configuration of FACSAria II and Preconjugated primary antibody-fluorochrome list for Panel A.**

Marker	Fluorochrome	Bandpass Filter (nm/nm)	Excitation (nm)	Fluorescence Emission Color	Description	Company / Catalog Number
CD11b/c	FITC	530/30	488	Green	Mouse Anti-CD11b/c equivalent antibody [MRC OX-42]	Abcam/ ab112170
CD29	PE-Cy7	780/60	488	Infrared	Anti-mouse/Rat CD29 (Integrin beta 1)	eBiociences/ 25-0291
CD44H	APC-Cy7	780/60	633	Infrared	Anti-Rat CD44H APC-eFluor 780 [OX49]	eBiosciences / Custom order
CD45	PerCP-Cy5.5	695/40	488	Far Red	Mouse Anti-rat CD45 Antibody [OX-1]	Biolegend/ 202220
CD68	PE-Texas Red	610/20	488	Orange	Mouse Anti Rat CD68 RPE-Texas Red [ED1]	AbD Serotec/ Custom order
CD105	PE	575/26	488	Yellow	Rabbit Anti-CD105/Endoglin polyclonal antibody	BIOSS/ bs-4609R-PE
CD106	Brilliant Violet 421	450/50	405	Blue	Mouse Anti-rat CD106 [MR106]	BD/ Custom order
His48	APC	660/20	633	Red	Anti-Rat Granulocyte Marker [HIS48]	eBiosciences / Custom Order
Cell Viability Dye	AmCyan	525/20	405	Green	Fixable Viability Dye eFluor® 506	eBiosciences / 65-0866-14

S2.2 Table: **Laser configuration of FACSAria II and Preconjugated primary antibody-fluorochrome list for Panel B.**

Marker	Fluorochrome	Bandpass Filter (nm/nm)	Excitation (nm)	Fluorescence Emission Color	Description	Company / Catalog Number
CD31	APC	660/20	633	Red	Anti-Rat CD31 (PECAM-1) [TLD-3A12] eFluor 660 / APC	eBiosciences/ 50-0310
CD45	PerCP-Cy5.5	695/40	488	Far Red	Mouse Anti-rat CD45 Antibody [OX-1]	Biolegend/ 202220
CD90	FITC	530/30	488	Green	Mouse Anti- Rat THY1 / CD90 [HIS51]	LSBio/ LS-C105942
CD163	PE-Cy7	780/60	488	Infrared	Mouse Anti Rat CD163 [ED2]	AbD Serotec/ Custom order
His48	PE	575/26	488	Yellow	Anti-Granulocytes antibody [HIS48]	eBioscience/ 12-0570
Cell Viability Dye	AmCyan	525/20	405	Green	Fixable Viability Dye eFluor® 506	eBiosciences/ 65-0866-14

S2.3 Table. **Flow Cytometry Results.** The numbers were calculated by gating analysis.

Cell	Panel	Day 0	Day1	Day2	Day3	Day5	Day7	Week2	Week4
Neutrophil	**A**	1387	2063	1440	1478	465	326	435	471
	B	1578	2314	1797	1574	560	374	451	541
Macrophage	**A**	887	1711	4042	1812	840	545	502	546
	B	926	2190	4361	1969	970	626	413	642
Endothelial Cell	**A**	1783	487	246	420	662	471	2317	794
	B	1896	980	206	427	513	686	2542	938
Fibroblast	**A**	9966	8575	3971	3856	11074	9422	7622	10403
	B	10649	7819	3532	3824	10014	9347	11347	10129
Fibroblast I	**A**	7347	4726	413	1754	7018	3158	4726	4741
	B	7509	3699	491	1862	6083	2833	7145	4190
Fibroblast II	**A**	2619	3849	3558	2102	4056	6264	2896	5662
	B	3140	4120	3041	1962	3931	6514	4202	5939
Macrophage M1	**A**	406	1352	3729	1502	652	306	274	204
	B	607	1775	3915	1480	800	405	312	296
Macrophage M2	**A**	473	359	313	310	188	238	229	344
	B	319	415	446	489	170	221	101	346
Total	**A**	19420	15250	12757	19254	20089	15064	17216	16307
	B	19136	15212	12799	18404	19700	15230	17235	16467

S2.4 Table: Percentages of the cell population of two independent animal pools on Day 2 following vocal fold surgery.

Cell Type	Pool 1	Pool 2
Neutrophil	11.29	11.84
Macrophage	31.68	32.82
Endothelial Cell	1.93	2.01
Fibroblast	31.13	32
Fibroblast I	3.24	3.07
Fibroblast II	27.89	28.93
M1 Macrophage	29.23	30.4
M2 Macrophage	2.45	2.42

CHAPTER 3: SENSITIVITY ANALYSIS, CALIBRATION AND VALIDATION OF VOCAL FOLD AGENT-BASED MODELS

3.1 PREFACE

In Chapter 2, a multi-parametric flow cytometry study was conducted to identify and enumerate four cell populations, namely neutrophils, macrophages, fibroblasts and endothelial cells in rat vocal folds following surgical injury. In this study, results from Chapter 2 were used to expand existing agent based models of vocal fold injury and repair (VF-ABM). The cellular outputs of VF-ABM were calibrated using empirical flow data from Day 1, Day 2, Day 3 and Day 5, and validated using time-points of Day 7, Week 2 and Week 4. The model sensitivity analysis and calibration were implemented using Random Forests and SPOTPY (Statistical Parameter Optimization Tool for Python), respectively. VF-ABM were validated using 95% confidence intervals to estimate corresponding accuracies in predicting each cell population. My contributions towards this manuscript include development of theoretical concepts, design of experiment, literature review, development of algorithms for sensitivity analysis, implementing Random Forests, data curation, developing three strategies for model calibration and validation, agent based model calibration using SPOTPY, statistical evaluation of model, and writing of manuscript.

Towards a physiological scale of vocal fold agent-based biological models: sensitivity analysis, calibration and validation

Aman Garg[1], Samson Yuen[2], Nuttiiya Seekhao[3], Grace Yu[4], Joseph JaJa[3], Luc Mongeau[1,5,6], Nicole Y. K. Li-Jessen[1,2,6]

[1] Department of Biological and Biomedical Engineering, McGill University, Montreal, Quebec, Canada

[2] School of Communication Sciences and Disorders, McGill University, Montreal, Quebec, Canada

[3] Department of Electrical and Computer Engineering, University of Maryland, College Park, Maryland, USA

[4] Department of Physiology, McGill University, Montreal, Quebec, Canada

[5] Department of Mechanical Engineering, McGill University, Montreal, Quebec, Canada

[6] Department of Otolaryngology-Head and Neck Surgery, McGill University, Montreal, Quebec, Canada

AG: Data Curation, Investigation, Methodology, Sensitivity Analysis, Calibration, Validation, Formal analysis, Writing - original draft, Writing - Review and editing

SY: Model development, Model Optimisation, Investigation, Methodology, Writing - Review and editing

NS: Model development, Investigation, Writing - Review and editing

GY: Model rules development and verification, Writing - Review and editing

JJ: Supervision, Investigation, Writing - Review and editing

LM: Formal analysis, Project administration, Resources, Supervision, Validation, Writing - Review and editing

NLJ: Conceptualization, Fund acquisition, Investigation, Methodology, Project administration, Resources, Supervision, Validation, Writing - Review and editing

PREPARED FOR JOURNAL IEEE TRANSACTIONS ON COMPUTATIONAL BIOLOGY AND BIOINFORMATICS

3.2 ABSTRACT

Agent based models of vocal fold injury and repair (VF-ABM) were developed to numerically simulate the cellular and molecular dynamics involved in surgical vocal fold injury and scarring. The aim of this study was to improve the biological representation of VF-ABM through sensitivity analysis, model calibration and verification. Empirical data of vocal fold cell populations were obtained using flow cytometry up to four weeks following surgical injury. Random Forests were used as a sensitivity analysis method to identify parameters that were most influential to ABM outputs. Statistical Parameter Optimization Tool for Python (SPOTPY) was used to calibrate those parameter values to match the simulation data with the corresponding empirical flow cytometry data. Three variations of calibration strategies were used and prediction accuracies of cellular outputs were obtained. The ABM predicted outputs were considered accurate if the empirical data points fell within the 95% confidence intervals of simulated outputs. Cell population quantities were calculated for Day 7, Week 2 and Week 4 respectively. Predicted cell populations were 100% accurate for Day 7. Although the trends of simulated cell populations were qualitatively comparable to those of the empirical data for Weeks 2 and 4, the empirical data values fell outside of the 95% statistical confidence intervals.

3.3 INTRODUCTION

Agent based computational models (ABM) have been used to simulate complex system dynamics. The basic framework of ABM consists of agents and agent-rules. Agents are decision-making units that interact with other agents and the environment. Agent-rules are formulated to control the action and decision of agents in the virtual world [67]. ABM have been widely applied to ecology,

economics, geography, business, political sciences and social sciences [210, 211]. Apart from those applications, ABM were also developed to understand complex acute and chronic diseases such as diabetes, traumatic brain injury, spinal cord injuries, acute liver failure and sepsis [41-45]. Owing to a large number of interacting components in biological systems, the conventional experimental approach of studying one isolated cell or molecule is not sufficient to understand the complexity of biological systems. Conventional experimental approaches have generated much useful knowledge and information about individual components of biological systems [48, 49]. The challenge is to connect these datasets in comprehending the complex dynamics of these systems [49]. In particular, the reductionist approach is limited to illuminate the mechanisms of interaction between individual components in deciphering the biological complexity [48]. For example, enzymes in a specific molecular pathway are often analyzed in isolation. Catalytic reactivity for these biological catalysts (enzymes) is however emerged from complex and dynamic interactions among various components (e.g., reactants, substrates, products etc.) of the targeted pathway [50]. Thus, the aggregated dynamics of these interactions are not intuitive and cannot be conceptualized by investigating each enzyme individually [50].

Systems biology provides an alternative method of investigation of investigating the aggregated activity of individual biological components at a systems level. In other words, systems biology focuses on the comprehension of how a process, a cell, a group of cells, or an organism act as a whole [51]. The main tool in systems biology is computational modeling and simulation. For example, system biology has been utilized for creating simulations of signalling pathways, transcription networks, metabolic processes and physiological processes, biochemical mechanisms [49]. Systems biology can be used to quantify the interrelationships (structure or

organization) and interaction (behavior or dynamics) between biological components and provide insights into developing a deeper mechanistic understanding of complex biological processes [52]. Systems biology does not only emphasize on the quantification of interactions between components, but also has potentials for reproducing emergent properties of a system. ABM, for instance, have been used widely as a tool of systems biology to simulate emergent behavior that may not be possible through other simulation approaches. In ABM, the emergent behavior is resulted from the interactions between individual components (agents) that is not programmed by users [53].

In addition, experimental/ research hypotheses can be tested using computational models, i.e., running silico experiments. The simulation results can then be validated by in vivo or in vitro empirical experiments [52, 54]. In the application of biomedical science, computer models can be used to numerically simulate individual treatment response of a disease as a function of patient profile [55]. In the era of personalized/ precision medicine, computational models have become an indispensable tool to integrate different forms of patient data (e.g., demographics, clinical, lifestyle etc.) and generate specific disease phenotypes or cohorts for in silico clinical trials [56, 57].

Model calibration is an important step to ensure a sufficient authenticity of model representation to the real world. Model calibration involves systematic alterations of the values of parameters in the model iteratively until the simulated outputs and the observable behavior of the system are as close as possible. Some common parameter estimation methods for ABM calibration have been reported to reduce the uncertainty of the model (**Table 3.1**). The pattern-oriented approach is used to estimate parameters by comparing observed trends and patterns in the model with empirical data [212-214]. For complex models having a large number of parameters, this

approach has been limited to the identification of relevant patterns for identifying hidden information [214]. The particle optimization (PSO) algorithm is a heuristic optimization method that is more suitable for computational models with a large number of parameters [215, 216]. The PSO investigates the mutual collaboration between particles for sharing the internal information and reduce parameter space by discarding implausible inputs [215, 216]. Since PSO has a low convergence rate in the iterative process, it is not ideal for ABM which require over thousands of iterations for each simulation [216]. Genetic algorithms (GA) are another heuristic optimization method that use a natural selection process to estimate as many as possible solutions simultaneously [217, 218]. In GA, the model parameter values are progressively modified using genetic operators namely mutation and crossover, to optimize the model's fitness in predicting the empirical data [217, 218]. One limitation of GA is parameter overfitting and variation in the results for each run [218]. Other existing tools for parameter estimation in ABM include parameter sweeping, Bayesian approaches, greedy algorithms and regressions, hybrid approaches and nonlinear multi-grid/finite difference methods. These methods are often notably expensive in terms of computing resources and are not ideal for biological models at large scales [219-223].

When the model has a large number of parameters with unknown values, model calibration can also be computationally expensive. The parameter search space scales up with the number of parameters in the model [224, 225]. Lengthy simulation times, ambiguities in model design and a large number of unknown parameters can also limit the efficiency of model calibration [226]. Sensitivity analysis is thus required to reduce the number of parameters before model calibration. Sensitivity analysis is a statistical technique to explore the variability of model outputs by systematically varying the input parameters. Multiple sensitive analysis methods have been

reported for ABM [227, 228]. The most common techniques are One Parameter At a Time (OPAT), Fourier Amplitude Sensitivity Test (FAST) regression-based methods and variance-based methods [227, 229, 230]. These methods, however, are often computationally expensive or unreliable for a large number of agents or they require excessive numerical simulation times [227, 229-232]. One alternative option for sensitivity analysis is therefore needed for running large-scale ABM with long-time scale simulations.

3.4 VF-ABM Development and Implementation

Vocal fold agent-based models (VF-ABM) were developed to numerically simulate the inflammatory and healing process following a surgical injury at a physiological scale [59-66]. VF-ABM were evolved on a computer node with two NVIDIA Tesla P100 12 GB Graphics Processing Units (GPUs) and two Intel E5-2683 v4 computer processing units (CPUs). GPUs were mainly used for running the chemical diffusion component of the model and implementing the visualizations of the simulations Open Graphics Library (OpenGL). The model was implemented in the object-oriented programming language C++ and Open Multi-Processing (OpenMP) for parallel computing [64-66].

The dimensions of the VF-ABM correspond to the physiological size of rat vocal folds, since most of the empirical data were available for this animal model [16, 20, 21, 31, 99, 110, 233-238]. The model size and configuration details are summarized in **Table 3.2**. Agent-rules of VF-ABM were formulated based on reported mechanisms in the vocal fold wound healing literature [18-20, 70, 71] (**Table 3.3**). Each time-step (or tick) corresponds to approximately 30 minutes of "real time" (Algorithm 1). A detailed description of VF-ABM can be found in [64]. In

brief, VF-ABM were composed of: (1) cells (platelets, macrophages, neutrophils and fibroblasts), (2) extracellular matrix (ECM) substances (collagen type I, elastin and hyaluronic acid (HA)) and (3) chemical mediators (tumor necrosis factor-α (TNF-α), interleukin-1β (IL-1β), interleukin-10 (IL-10), interleukin-6 (IL-6) interleukin-8 (IL-8), basic fibroblast growth factor (bFGF), and transforming growth factor (TGF-β1)). Based on initial inputs of initial wound size, the model was used to predict the post-injury trajectories of inflammatory cytokines and ECM markers in surgical vocal fold injury [63]. Partial calibration and validation were performed with vocal fold biological data [18-20, 70, 71]. However as quantitative data on vocal fold cellularity were limited, the cellular data have not been fully calibrated and validated in current VF-ABM.

3.5 STUDY OBJECTIVES

The objectives of this study were 1) to implement sensitivity analysis of VF-ABM and identify key influential parameters in the model, and 2) to calibrate and verify the cell number outputs of VF-ABM with empirical vocal fold cell population data from flow cytometry.

3.5.1 Vocal Fold Cell Population Data

Multi-parametric flow cytometry using up to 11 parameters were used to identify and enumerate neutrophils, macrophages, endothelial cells and fibroblasts in surgically injured rat vocal folds up to 4 weeks post-injury. Distinctive cell populations were identified using bivariate gating. The percentage of specific cell populations from the total population were calculated [237]. Based on the empirical data, an influx of neutrophils, macrophages, endothelial cells and fibroblasts was observed one day, two days, two weeks and one week post-surgery, respectively. Fibroblasts were the dominant cell type in both injured and uninjured rat vocal folds. In addition, subtypes of

macrophages and fibroblasts, putatively corresponding to classically and alternatively activated macrophages and to typical fibroblasts and myofibroblasts, appeared to show distinct patterns of temporal changes in surgical vocal fold repair [29, 30, 84, 152, 169-171, 175-177].

3.6 SENSITIVITY ANALYSIS, MODEL CALIBRATION AND VALIDATION

In this study, Random Forests and Robust Parameter Estimation (ROPE) were used for sensitivity analysis and model calibration respectively. The goal of sensitivity analysis was to determine the influence of model parameters on the ABM outputs in order to select the most important parameters and reduce the number of parameters for calibration. Random Forests were chosen as sensitivity analysis method because it does not require many samples for the implementation and thus makes the computational cost feasible for the notable scale of VF-ABM. ROPE was selected for VF-ABM calibration because it accelerates the calibration process by iteratively using information from previous simulations to estimate the outputs of subsequent ones [239, 240].

3.6.1 SENSITIVITY ANALYSIS

The Random Forests algorithm was used to perform the sensitivity analysis in this study (**Figure 3.1**). Random Forests are a machine learning procedure that has been employed for the quantification of parameter importance and parameter selection [241-243]. This method has been used for ecological, biological and disease models [244-249]. It can handle high dimensional data, thousands of input variables, complex parameter interaction, and missing data [250].

Random Forests use an ensemble method with decision trees that are constructed using bootstrapping [251]. To split the node on any variable (or parameter) within a tree, the GINI

impurity criterion (GINI Index) is used [252, 253]. The GINI Index for two descendent nodes should be less than that of the parent node. A node is split if the change in GINI Index is significant [226]

$$\Delta \boldsymbol{i}(\boldsymbol{t}) = \boldsymbol{i}(\boldsymbol{t}) - \frac{\boldsymbol{N_L}}{\boldsymbol{N}} \boldsymbol{i}(\boldsymbol{t_L}) - \frac{\boldsymbol{N_R}}{\boldsymbol{N}} \boldsymbol{i}(\boldsymbol{t_R}). \qquad \textbf{Equation 3.1}$$

where, t_L is the node on the left, and t_R the node on the right, N_L is the number of samples on left node and N_R is the number of samples on right node. The importance of any variable (or parameter) is determined by Mean decrease GINI, given by [226]

$$\boldsymbol{I}(\boldsymbol{P}) = \sum_{\boldsymbol{T}} \sum_{\boldsymbol{N}} \Delta \boldsymbol{i_P}\ (\boldsymbol{N}, \boldsymbol{T})\ . \qquad \textbf{Equation 3.2}$$

The mean decrease GINI *(I)* for a parameter *(P)* is evaluated by adding up the weighted GINI indices *(i)* for all nodes *(N)* where parameter *P* is used (averaged over all trees *T* in the forest) [252]. This quantity indicates how often a parameter *P* was selected for a split and provides a relative ranking of the parameters.

To find the suitable number of iterations, *n* for our sensitivity analysis, pilot tests were implemented with *n* = 3000, 4000, 4500, 5000, and 5500. It was observed that after 4500, the top three parameters for each cell type and time-point were identical and thus *n*=5000 was chosen for this study. Global sensitivity analysis was then implemented independently for the first four time-points (Day 1, Day 2, Day 3 and Day 5) as these time points would be used for the subsequent calibration.

The R package *RandomForest* was implemented in our computations (Algorithm 2) [254]. The user setting was set as (1) Number of Input parameters = 213, (2) Number of Output

Parameters = Neutrophils, Macrophages, or Fibroblasts and (3) Number of Samples/ Number of Iterations of Model = 5000. The ranking of parameter importance was then obtained by sorting the parameters according to their Mean Decrease GINI (**Figure 3.2, S3.1, S3.2 and S3.3**).

3.6.2 MODEL CALIBRATION

The Statistical Parameter Optimization Tool for Python (SPOTPY) package was used for parameter calibration [239]. The SPOTPY package has a library of algorithms and objective functions for model calibration and validation. The overview of SPOTPY calibration is shown in Algorithm 3. The algorithm has five major steps: (1) Sampling, (2) Simulation, (3) Evaluation, (4) Objective Function and (5) Parameter Estimation. Sampling was implemented for the most important parameters based on the sensitivity analysis using a uniform distribution and a predefined range. After sampling was done, the simulation was evolved with the generated parameter set using the sampling function and the output was stored as simulated data. The empirical flow cytometry data was then added as evaluation data. An objective function was then used to estimate the performance of the model for that given parameter set. The root mean square error (RMSE) was then used as the objective function, which determines the fitness of simulated data to evaluated data. RMSE is given by

$$\boldsymbol{RMSE = \sqrt{1/m \sum_i^m (e(i) - s(i))^2}} \qquad \textbf{Equation 3.3}$$

Here, *e(i)* is evaluated data, *s(i)* is simulated data and m is the total number of parameters.

Lastly, the Robust Parameter Estimation (ROPE) algorithm was used for parameter optimization based on the concept of data depth [239]. The principle of ROPE is to identify a set

of parameter vectors with the high model performance and subsequently generate a set of parameter vectors with high data depth with respect to the first set [239, 240]. Instead of requiring thousands of random parameter sets, ROPE uses the results from the previous simulation as knowledge to define the parameter sets for the subsequent simulations. ROPE is recommended when the model requires parallel computing and the simulations are expensive, as the case of VF-ABM herein [239, 240]. The top 10% results are used to generate the next parameter sets. After estimating the best set of parameters, the algorithm repeats the sampling again. This time, the algorithm uses parameter sets learnt from previous runs to determine the parameter set for next run. The procedure repeats either until the defined number of iterations is reached or the RMSE reaches zero.

In the present study, three variations of model calibration were evaluated (**Figure 3.3** and **Figure 3.4**). In all cases, flow cytometry data from the first four time-points (Day 1, Day 2, Day 3 and Day 5) was used and the VF-ABM was run 800 times iteratively for each calibration step. The number of important parameters determined by Random Forests were varied in these three strategies. For Strategy 1, the top three parameters for each cell type for each time point were used to proceed for calibration (**Table 3.4**). Hence, a total of 36 top parameters were ranked for each cell type at each time point (3 parameters x 3 cell types x 4 time points). Since same parameters were passed to each of these 12 categories (3 cell types x 4 time points) for sensitivity analysis, 12 of 36 parameters were overlapped across conditions. As a result, a set of 24 unique parameters was calibrated iteratively with all other parameters being fixed as constants until the model eventually yielded a satisfactory match between simulation data and empirical data. All four time points (Day 1, Day 2, Day 3 and Day 5) were first calibrated for each cell type individually and calibrated

values of parameter sets for each cell type were determined. Subsequently, a new parameter range was reduced to 10% of its original range close to the calibrated value and was then re-entered manually in SPOTPY. The modified range for a particular parameter was estimated using

$$\boldsymbol{Mi'} = \begin{cases} \boldsymbol{C - 0.1 \times (Ma - Mi),\ if\ [C - 0.1 \times (Ma - Mi)] > Mi} \\ \boldsymbol{Mi,\ if\ [C - 0.1 \times (Ma - Mi)] < Mi} \end{cases} \quad \textbf{Equation 3.4}$$

$$\boldsymbol{Ma'} = \begin{cases} \boldsymbol{C + 0.1 \times (Ma - Mi),\ if\ [C + 0.1 \times (Ma - Mi)] < Ma} \\ \boldsymbol{Ma,\ if\ [C + 0.1 \times (Ma - Mi)] > Ma} \end{cases} \quad \textbf{Equation 3.5}$$

where, *Mi'* and *Ma'* are new minima and maxima, *Mi* and *Ma* are old minima and maxima and *C* is the calibrated value of the parameter. The parameters were then recalibrated again using the modified range with ROPE.

For Strategy 2, the workflow was similar to that of Strategy 1 but with no manually modified parameter ranges and recalibration (**Figure 3.3** and **Figure 3.4**, **Table 3.5**). Strategy 2 was chosen for evaluation because this approach is commonly reported in the literature [219-223]. For Strategy 2a, the same set of 24 parameters was used as those of Strategy 1, representing the top three parameters for each cell type at each time point from the sensitivity analysis. For Strategy 2b, the top 5 parameters for each cell type across all time points were subjected to calibration.

3.6.3 MODEL VALIDATION

For model validation, the calibrated model was evaluated statistically for its accuracy in predicting cell counts at the Day 7, Week 2 and Week 4. Given ABM's stochastic properties, the model was run 100 times up to Day 28 to generate a representative data set for statistical evaluation. The means and standard deviations of model outputs for each cell type were computed at each time-

point. A 95% confidence interval was computed for each cell type from the simulations using [62, 63, 255]

$$\boldsymbol{Confidence\ Interval} = \mu \pm \boldsymbol{z} \times (\boldsymbol{\sigma}/\sqrt{\boldsymbol{n}}) \qquad \textbf{Equation 3.6}$$

Here, μ is the mean value of a predicted cell type, z is value on the standard normal curve with area (1-α) between $-z$ and z, σ is the standard deviation of a predicted cell type and n is the number of simulations. The VF-ABM-predicted outputs would be considered accurate if the empirical results for a given cell type fall within the 95% confidence interval (α = 5% = 0.05; z = 1.96) of the simulation outputs.

3.7 RESULTS

Random Forests were used to quantify the variance contribution of influential parameters to model outputs. Mean decrease GINI was used to rank the parameters from most influential to least influential. **Figure 3.2** shows the 25 most influential parameters for each cell type at Day 1, with information on the associated biological functions. Rankings of all other model parameters across days are available in the Supplementary Information (**S3.1, S3.2, S3.3, S3.4, S3.5, S3.6 and S3.7**). Parameters related to cytokine synthesis, cell activation, ECM synthesis and cell recruitment (sprouting amount) were found in most of the top 25 parameters across all cell types and time-points. For Strategies 1 and 2a, 45.83% of parameters used (11/24) were related to sprouting amount and sprouting frequency. For Strategy 2b, 66.7% of parameters (10/15) were related to sprouting amount and sprouting frequency.

The simulated trajectories of cell populations were different depending on the calibration

method. The VF-ABM has reproduced the most approximated dynamics of all cell populations from the empirical data between Day 1 to Week 4 (**Figure 3.5** and **Figure 3.6**) with Strategy 1. For neutrophils, the peak was delayed by one day. Macrophage predictions reached a maximum concentration on Day 2, in contrast to Day 1 in the data. For fibroblasts, the model predicted the peak at the correct time point on Day 2 but did not resemble the oscillation pattern as observed in the empirical data. Although Strategy 2a best predicted the neutrophils peak, Strategy accurately predicted peaks for other cell types. On the other hand, Strategy 2b worked well for macrophages only.

In addition to the overall patterns, statistical tests of 95% confidence intervals were used to quantitatively evaluate the prediction accuracy of model outputs. Prediction accuracy was calculated for each time point (i.e., Day 7, Week 2 and Week 4) based on how many empirical data points (i.e., counts of neutrophils, macrophages and fibroblasts) fell within the 95% confidence interval ($\alpha = 5\% = 0.05$; $z = 1.96$) of simulated outputs **(Table 3.6)**. For Day 7, all empirical data were within the 95% confidence intervals and thus a 100% prediction accuracy (3/3) was reached with Strategy 1. Prediction accuracy was zero for both Strategies 2a and 2b. For Week 2 and Week 4, all empirical data points fell outside the 95% intervals. However, when examining the data closely, Strategy 1 showed the closest predicted ranges to the empirical data. For example, the empirical cell counts for neutrophils were 180 and 214 at Week 2 and Week 4 respectively; whereas the VF-ABM predicted ranges were from 203.13 to 206.61 and from 208.48 to 211.84 respectively.

3.8 DISCUSSIONS

In this study, VF-ABM were calibrated for Day 1, Day 2, Day 3 and Day 5 and validated for Day 7, Week 2 and Week 4. Random Forests were implemented as a sensitivity analysis method to identify the most influential parameters to ABM outputs for cell populations. Sensitivity analysis results indicated a high influence of sprouting-related parameters on the model. In the current ABM, there were 20 parameters related to sprouting amount and sprouting frequency. Among them, 11 parameters were identified as most influential to the model output based on sensitivity analysis. Sprouting frequency corresponds to the rate of the cell infiltration whereas sprouting amount corresponds to the number of cells to proliferate within the tissue.

In current VF-ABM, many biological activities of neutrophils, macrophages and fibroblasts are controlled by parameters of sprouting frequency and amount. Tissue repair process starts with the migration of cells into the wound area [78, 164]. Upon tissue injury, neutrophils transmigrate through blood capillaries to the damage site [82, 160, 164]. Neutrophils are responsible to clean up damaged cell and tissue debris [78, 164]. Macrophages infiltrate into the wound right after neutrophils. Macrophages play a key role in the transition between the inflammatory and proliferative phases through the release of growth factors and cytokines that mediate ECM synthesis of fibroblasts [82, 160, 164]. Growth factors and cytokines also stimulate the migration and proliferation of fibroblasts [78, 82, 110, 160]. Fibroblasts proliferate and synthesize ECM components for repairing the connective tissue of the wound [78, 82, 110, 160]. Two sprouting-related parameters, namely parameter 155 (WhSproutAmount4) and parameters 156 (WhSproutAmount5) were used to control the amount of neutrophils. Three sprouting-related parameters [parameter 159 (WhSproutAmount8), 160 (WhSproutAmount9) and parameters 161

(WhSproutAmount10)] were used to control the amount of macrophages. Four sporuting-related parameters [parameter 150 (WhSproutFreq5), 162 (WhSproutAmount11), 163 (WhSproutAmount12) and parameters 164 (WhSproutAmount13)] were used to control the amount of fibroblasts.

Parameters of sprouting frequency and amount were basically used to abstract the transmigration of neutrophils and macrophages from capillary to mucosal tissue as well as the recruitment and proliferation of fibroblasts in VF-ABM. Further, the sprouting-related parameters for fibroblasts were also linked to cytokines, growth factors and ECM contents in VF-ABM. Sprouting-related parameters are thus critical to initiate and sustain cell activities of neutrophils, macrophages and fibroblasts during tissue repair. The ABM outputs of cell numbers are mostly determined by the sprouting amount and sprouting frequency of these three cell types. As cell numbers were used as inputs for calibration, it is reasonable that the parameters of sprouting amount and frequency have the strongest influence on outputs of cell numbers in VF-ABM.

The execution of Random Forests does not require a large number of samples for running sensitivity analysis. This feature makes Random Forests less computationally expensive and more reliable for simulating long time scale models as compared to other sensitivity analysis methods [241-243, 250]. For example, the estimated number of samples required for Fourier Amplitude Sensitivity Test (FAST) is 128 × parameter number ^ 2. That is, a total of 5,766,549 samples for the case of VF-ABM. An estimated time of running FAST is seven years with the computer node of two NVIDIA Tesla P100 12 GB GPUs and two Intel E5-2683 v4 CPUs [231, 232]. FAST is thus not a practical option for the sensitivity analysis of VF-ABM. On the other hand, Random Forests required only 5000 samples for the same model. The Random Forests method requires

fewer samples because it uses a bootstrapping method for sampling [241-243, 256]. The bootstrapping method uses samples as a population and takes random samples with replacement from this population to build other samples [256]. Hence, Random Forests aggregate several possible forests built from sub-samples of original data. One limitation of Random Forests is to set a prior assumption of the number of trees. There is no unique way to estimate the optimal number of trees [257]. In this study, the number of trees was estimated by implementing Random Forests iteratively as a function of tree number until the sensitivity analysis results converged.

ROPE calibration protocol was used for VF-ABM calibration and three calibration strategies were evaluated. These three calibration strategies were incorporated with different sets of parameters to determine the effect of parameter variation on calibration procedures and model prediction accuracy. Overall, Strategy 1 generated better resemblance and prediction accuracies than those from the other two strategies (**Figure 3.5** and **Table 3.6**). Strategy 1 involved an additional step of parameter range modification and model recalibration. The second calibration was performed on a narrower and more specific parameter range. In other words, Strategy 1 optimized the parameter value twice as compared to once in Strategies 2a and 2b. The inclusion of recalibration with modified narrow range and repeated calibration for a parameter notably increased the accuracy of model calibration. At the same time, Strategy 2 is four times less computationally expensive than Strategy 1. For running the calibration algorithm itself, Strategy 1 and Strategy 2 took eight and two days respectively for VF-ABM using existing computing resources (i.e., two NVIDIA Tesla P100 12 GB GPUs and two Intel E5-2683 v4 CPUs). The choice of calibration strategies depends on the purpose of the models. Strategy 1 would be useful if the statistical accuracy is particularly important to the application of the models. For example,

identifying the type of tumor (adenocarcinoma or neuroendocrine) and its subtypes is paramount to prescribe the correct cancer treatment for a patient [258, 259]. Although the pathology may look alike, the treatments for these two conditions are completely different [258]. Subtypes of adenocarcinoma that are associated with mucinous cystic neoplasms would need a less aggressive course of treatment compared to treatments for other conditions [258, 259]. Hence, accuracy in differentiating subtypes of tumors is essential to determine the most effective treatment. On the other hand, if the purpose of the model is to match the overall dynamics of empirical data with simulation data and achieving statistical accuracy is not the main concern, such as bird flocking and consumer purchase patterns, Strategy 2 can be a viable option given its lower cost [260].

The overall temporal trajectories of neutrophils, macrophages and fibroblasts were found to be in reasonable agreement between empirical and simulated data (**Figure 3.5**). Despite the stochasticity property of ABM, the dynamic of randomness (as reflected on the error bars) was not notable from the simulation data (**Figure 3.5**, **Figure 3.6** and **Table 3.6**). As such, current ABM may be limited to represent the population variations as seen in the observable data. Statistically, VF-ABM was accurate in predicting the empirical data for Day 7 with 100% accuracy for all cell counts, but not for longer time points (Week 2 and Week 4). One plausible reason could be the lack of empirical data for time points between Day 7 and Week 2 to train the model during calibration. Thus, empirical data from extra time points between Day 7 and Week 2 may be required for the ABM calibration. In addition, more number of parameters may need to be calibrated for better model performance. There was no significant difference in mean decrease GINI score of top 25 parameters for each cell type at each time point and thus only three parameters were considered for calibration as first pass herein. As such, including the remaining 22 parameters in the

calibration might further improve the accuracy of model prediction. Current VF-ABM, however, were not able to reach the magnitude of neutrophils and macrophages peaks as seen in the empirical data. For neutrophils and macrophages, the estimation of initial parameter range for their sprouting frequencies (i.e., the rate of the cell infiltration when there is tissue damage) was difficult to define for calibration. The infiltration rates of neutrophils and macrophages were reported as a function of blood flow in the human circulatory system [261]. However, specific information on rates of blood flow and injury-induced vasodilation within the vocal fold lamina propria are not available to date. Such data are necessary to better simulate the transmigration of neutrophils and macrophages from capillary to mucosal tissue in VF-ABM.

In addition, the VF-ABM stimulated data showed a notable discrepancy of fibroblast counts from the empirical trend at Week 2 and Week 4. The simulated fibroblast counts were lower than those of empirically observed by 1.8 and 14 folds for Week 2 and Week 4, respectively. Specifically, between Day 2 and Day 5, the ABM-simulated fibroblast curve was critically damped while the empirical curve was underdamped. Further, the ABM was not able to produce similar final value (Week 4) as compared to the empirical data. Based on literature, proliferation rates of fibroblasts are 15.4 ± 1.1% after 4 days, 4.1 ± 0.6% after 1 week, and less than 0.5% after 2 weeks from rodent cardiac literature [262]. Since the proliferation rate of fibroblasts greatly depends on the microenvironment such as cytokine levels and ECM contents, the exact rate for vocal fold fibroblasts was not fully accurate given the cardiac tissue data. Additional empirical data are thus needed to better estimate the proliferation rates of vocal fold fibroblasts in both homeostatic and injurious conditions. Once the data become available, parameters related to the sprouting amount and sprouting frequency of fibroblasts can be revised to improve the long-term prediction of VF-

ABM.

In summary, future work includes extending the existing model, and further refining the rules and parameters that might have a significant effect on the accuracy of the model and strengthens the applicability of the model to the real clinical scenario. Such a system will substantially contribute to the advancement of vocal fold research leading to explain the mechanisms underlying inflammation and wound healing. Results from this study suggested the areas of improvements for the next generation of VF-ABM. When successfully validated, the model may provide insights in designing more precise treatment strategies to target specific cell populations and timing of application in optimizing wound healing outcomes following vocal fold surgery. Ultimately, the VF-ABM will contribute to the advancement of computational medicine in voice disorders.

3.9 ACKNOWLEDGEMENTS

We would like to acknowledge Compute Canada for their support of clusters and computational resources, which made this calibration possible. This study was supported by National Institute of Deafness and other Communication Disorder of the National Institutes of Health under award number R03DC012112 (PI: Li-Jessen) and R01DC005788 (PI: Mongeau). All authors read and approved the final manuscript. We declare that the authors have no conflict of interest.

3.10 ALGORITHMS

Algorithm 1: Overview of 3D Rat VF ABM

```
Procedure VFABM
    Initialization of patches
    Initialization of chemicals
    Initialization of cells
    Initialization of ECM
    Initialization of damage

    For each tick
      /* Model Computation */
      For each Patch
          Seed Cell Function
          ECM Function
          ECM Fragmentation
      For each Cell
          Cell Function
      For each Chemical Type
          Diffuse Chemical

      /* Model Update */
      For each Patch
          Update ECM
          Update Patch
          Update Chemicals
      For each Cell
          Update Cell
```

Algorithm 2: Random Forests in R

```
Library - clusterGeneration
Library - mnormt
Require - randomForest
Library - caret

Number of Trees = 600

X=Samples
Y=Model Output for a time point T and cell type C

Df = data.frame (Y,X)
allX = paste ("X", 1:ncol(X),sep="")
names(df) = c("Y", allX)
fit= randomForest(factor(Y)~., data=df)
VI_F = importance(fit)
varImp(fit)
varImpPlot(fit, type=2)
```

Algorithm 3: SPOTPY Calibration

Do
{
Sampling using ROPE: Generate Parameter Sets
Simulation: Run Model using Input Parameters
Evaluation: Comparing simulated results with experimental values
Objective Function: Determine Root Mean Squared Error (RMSE) between the simulations and experimental values.
Parameter Estimation: Return best parameter set with help of top 10% results (Using ROPE and RMSE)

} While (Iteration < 1000 && RMSE != 0)

Return best parameter set (having minimum RMSE)

End

3.11 TABLES

Table 3.1. Summary of Literature Showing Different Parameter Estimation Methods Used in Different ABM.

Study	Calibration Method	No of unknown parameters	Agent Based Model	Summary
Folcik et al., 2007 [220]	Parameter Sweeping	87	Basic Immune Simulator	Basic Immune Simulator (BIS) was developed to scrutinize the interactions among the cells of the innate and adaptive immune systems. For calibration, parameter sweeping of the initial agent population size was implemented, and simulation patterns were compared to those stated in the literature.
Grimm et al., 2005 [212]	Pattern-Oriented Approach	unreported	Ecology	A pattern-oriented modeling approach was used for decoding the internal organization of complicated agent-based systems.
Gallaher et al., 2017 [219]	Hybrid Approach	16	Glioblastoma multiforme model	A hybrid approach was used to converge on a set of parameters that fit bulk data and individual data. It also determined important parameters for the model and also those parameters which had little influence on the measured output.
Hussain et al., 2015 [223]	Bayesian Approach	24	Dynamics of acute inflammation	Bayesian statistical model checking, sequential hypothesis testing, and stochastic optimization were used for the automatic parameter estimation of complex stochastic models.
Li et al., 2017 [215]	Particle swarm optimization (PSO)	50	Immune System	The input space of parameters was condensed by discarding the implausible input values and particle swarm optimization algorithm (PSO) was used to calibrate the model parameters by fitting the empirical data among the non-implausible input values.
Moedomo et al., 2010 [217]	Genetic Algorithm	6	Avian Influenza (H5N1) viruses mutation	It involved the modeling of virus mutation which is responsible for Influenza Pandemic phenomena. Using the Genetic Algorithm, the chromosome solution and fitness values of Influenza Pandemic stages were specified and the maximum fitness values were obtained.

Tong et al., 2015 [221]	Greedy algorithm and Regression	4	Immune System	An integrated ABM regression model (IABMR) was developed having advantages of both ABM and differential equations (DE) which is capable to simulate the immune system at various scales, phenotypes and cell types. Greedy algorithm and Loess regression were employed estimating the key parameters of the ABM by fitting the experimental data set.
Wise et al., 2008 [222]	Nonlinear multigrid/finite difference method	20	Three-dimensional multispecies nonlinear tumor growth	A diffuse interface continuum model of multispecies tumor growth and tumor-induced angiogenesis was developed in both two and three dimensions. A nonlinear multigrid finite difference method with nearly optimal complexity was used as algorithm for the calibration.

Table 3.2. Summary of Initial Configurations of VF-ABM.

Item	Unit	Size	Reference
Vocal Fold Width	mm	1	[233]
	patches	142	
Vocal Fold Height	mm	1	[233]
	patches	142	
Vocal Fold Thickness	mm	0.2	[233]
	patches	28	
Vocal Fold Epithelium Thickness	mm	0.01	[31]
	patches	1	
Capillary Diameter	µm	7	[234]
	patches	1	
Capillary Gap	µm	12.89	[234]
	patches	1	
Total number of patches	patches	564,592	-
Total number of non-epi patches	patches	544,428	-
Total number of capillary patches	patches	138,450	-
Total number of tissue patches	patches	405,978	-
Simulated time-step	Minutes	30	-
Neutrophils	µm	7	[235]
	Cells	517	[237]
Macrophages	µm	6	[236]
	Cells	316	[237]
Fibroblasts	µm	6	[235]
	Cells	3594	[237]

Table 3.3. Summary of Agent Rules in VF-ABM.

Agent	Rules
Platelets	Secrete TGF-β1, MMP8 and IL-1β to attract other cells.
Neutrophils	Arrive at wound site within first three days after injury. Carry out anti-bacterial functions and secrete TNF-α and MMP8 to attract other Neutrophils and Macrophages. The decline on Day 3 shows the transition from acute inflammation to the sub-acute and repair phases after injury.
Macrophages	Represent phase of acute inflammation by arriving at wound site within first three days with a peak on Day 2. Responsible for phagocytosis of bacteria and cell debris and secrete reactive oxygen species, TNF-α, TGF-β1, FGF, IL-1β, IL-6, IL-8 and IL-10 which attract additional macrophages to wound area.
Fibroblasts	Dominant cell type in vocal folds. Start proliferation phase and show maximum concentration between Day 5 and Day 7. Play important role in wound remodeling and secrete TNF-α, TGF-β1, FGF, IL-6 and IL-8 to attract other cells. Deposit ECM proteins to repair tissue damage.

Table 3.4. Top Parameters Estimated by Random Forests Sensitivity Analysis.

Time Point	Cell	Parameter	Biological Significance
Day 1	Neutrophils	156-WhSproutAmount5	Determine the amount of neutrophil to sprout when damage is present
		164--WhSproutAmount13	Determine the amount of fibroblast to sprout when damage is present
		39--MacCytSynth14	Cytokine Synthesis
	Macrophages	148--WhSproutFreq3	Frequency to sprout blood macrophage when damage is present
		117--FibCytSynth10	Cytokine Synthesis
		133--FibCytSynth26	Cytokine Synthesis
	Fibroblasts	200--FibProlif0	Fibroblast Proliferation
		150--WhSproutFreq5	Frequency to sprout fibroblast when damage is present
		166--FibActivat1	Fibroblast Activation
Day 2	Neutrophils	156--WhSproutAmount5	Determine the amount of neutrophil to sprout when damage is present
		181--FibECMsynth0	Fibroblast ECM Synthesis
		103--MacCytSynth78	Cytokine Synthesis
	Macrophages	159--WhSproutAmount8	Determine the amount of tissue macrophage to sprout when damage is present
		158--WhSproutAmount7	Determine the amount of blood macrophage to sprout when damage is present
		177--NeuActivat2	Factor in Neutrophil activation
	Fibroblasts	14--NeuCytSynth10	Cytokine Synthesis
		72--MacCytSynth47	Cytokine Synthesis
		11--NeuCytSynth7	Cytokine Synthesis
Day 3	Neutrophils	156--WhSproutAmount5	Determine the amount of neutrophil to sprout when damage is present
		200--FibProlif0	Fibroblast Proliferation
		148--WhSproutFreq3	Frequency to sprout blood macrophage when damage is present
	Macrophages	149--WhSproutFreq4	Frequency to sprout tissue macrophage when damage is present
		160--WhSproutAmount9	Determine the amount of tissue macrophage to sprout when damage is present
		103--MacCytSynth78	Cytokine Synthesis

	Fibroblasts	110--FibCytSynth3	Cytokine Synthesis
		51--MacCytSynth26	Cytokine Synthesis
		117--FibCytSynth10	Cytokine Synthesis
Day 5	Neutrophils	156-WhSproutAmount5	Determine the amount of neutrophil to sprout when damage is present
		155-WhSproutAmount4	Determine the amount of neutrophil to sprout when damage is present
		153-WhSproutAmount2	Determine the amount of neutrophil to sprout when damage is 0
	Macrophages	154-WhSproutAmount3	Determine the amount of macrophage to sprout when damage is 0
		159--WhSproutAmount8	Determine the amount of tissue macrophage to sprout when damage is present
		149--WhSproutFreq4	Frequency to sprout tissue macrophage when damage is present
	Fibroblasts	200--FibProlif0	Fibroblast Proliferation
		51--MacCytSynth26	Cytokine Synthesis
		110--FibCytSynth3	Cytokine Synthesis

Table 3.5. Comparison of Parameters Used for Strategy 1 and Strategy 2.

Cell	Parameters	Strategy 1/2a	Strategy 2b
Neutrophils	156-WhSproutAmount5	●	●
	164--WhSproutAmount13	●	●
	39--MacCytSynth14	●	
	181--FibECMsynth0	●	
	103--MacCytSynth78	●	●
	155-WhSproutAmount4	●	●
	153-WhSproutAmount2	●	●
Macrophages	148--WhSproutFreq3	●	●
	133--FibCytSynth26	●	
	159--WhSproutAmount8	●	●
	158--WhSproutAmount7	●	●
	177--NeuActivat2	●	
	149--WhSproutFreq4	●	●
	160--WhSproutAmount9	●	
	154-WhSproutAmount3	●	●
Fibroblasts	200--FibProlif0	●	●
	150--WhSproutFreq5	●	●
	166--FibActivat1	●	
	14--NeuCytSynth10	●	
	72--MacCytSynth47	●	
	11--NeuCytSynth7	●	
	110--FibCytSynth3	●	●
	51--MacCytSynth26	●	●
	117--FibCytSynth10	●	●

Table 3.6. VF-ABM Prediction Accuracies for Strategy 1 and Strategy 2. * within the 95% Confidence Interval.

Cell	Time-point	Empirical data	95% Confidence Interval of ABM Outputs		
			Strategy 1	Strategy 2a	Strategy 2b
Neutrophils	Day 7	214	210.55 - 214.03*	201.25 - 204.39	583.11 - 588.69
Macrophages	Day 7	359	354.1 - 364.2*	89.38 - 92.22	152.24 - 167.62
Fibroblasts	Day 7	5751	5714.92 - 6411.98*	5288.46 - 5588.82	5046 - 5550.92
Prediction accuracy			**100%**	**0%**	**0%**
Neutrophils	Week 2	180	203.13 - 206.61	203.67 - 206.45	586.11 - 591.49
Macrophages	Week 2	186	124.14 - 129.46	65.07 - 67.27	38.91 - 41.17
Fibroblasts	Week 2	3854	2097.43 - 2186.57	1871.13 - 1975.09	1746.27 - 1912.37
Prediction accuracy			**0%**	**0%**	**0%**
Neutrophils	Week 4	214	208.48 - 211.84	208.09 - 211.97	600.75 - 605.69
Macrophages	Week 4	252	16.19 - 17.95	54.65 - 56.43	24.76 - 26.1
Fibroblasts	Week 4	4347	298.03 - 310.87	266.5 - 282.06	246.85 - 271.11
Prediction accuracy			**0%**	**0%**	**0%**

3.12 FIGURES

Figure 3.1. Flowchart of Random Forests for sensitivity analysis. Three factors were taken into account for sensitivity analysis namely, *T* trees, *P* input parameters and one output parameter. The algorithm produced categorical classes of output. It produced *T* trees by repeating the following procedure *T* times. It took *p* number of random parameters and then created and optimized a tree. GINI Index of all *p* parameters was computed for all the nodes in this tree. It was used to decide the further splitting of the node. After creating all *T* trees, mean decrease GINI was estimated for each parameter by aggregating the weighted GINI Index for all nodes in those trees where that parameter was used.

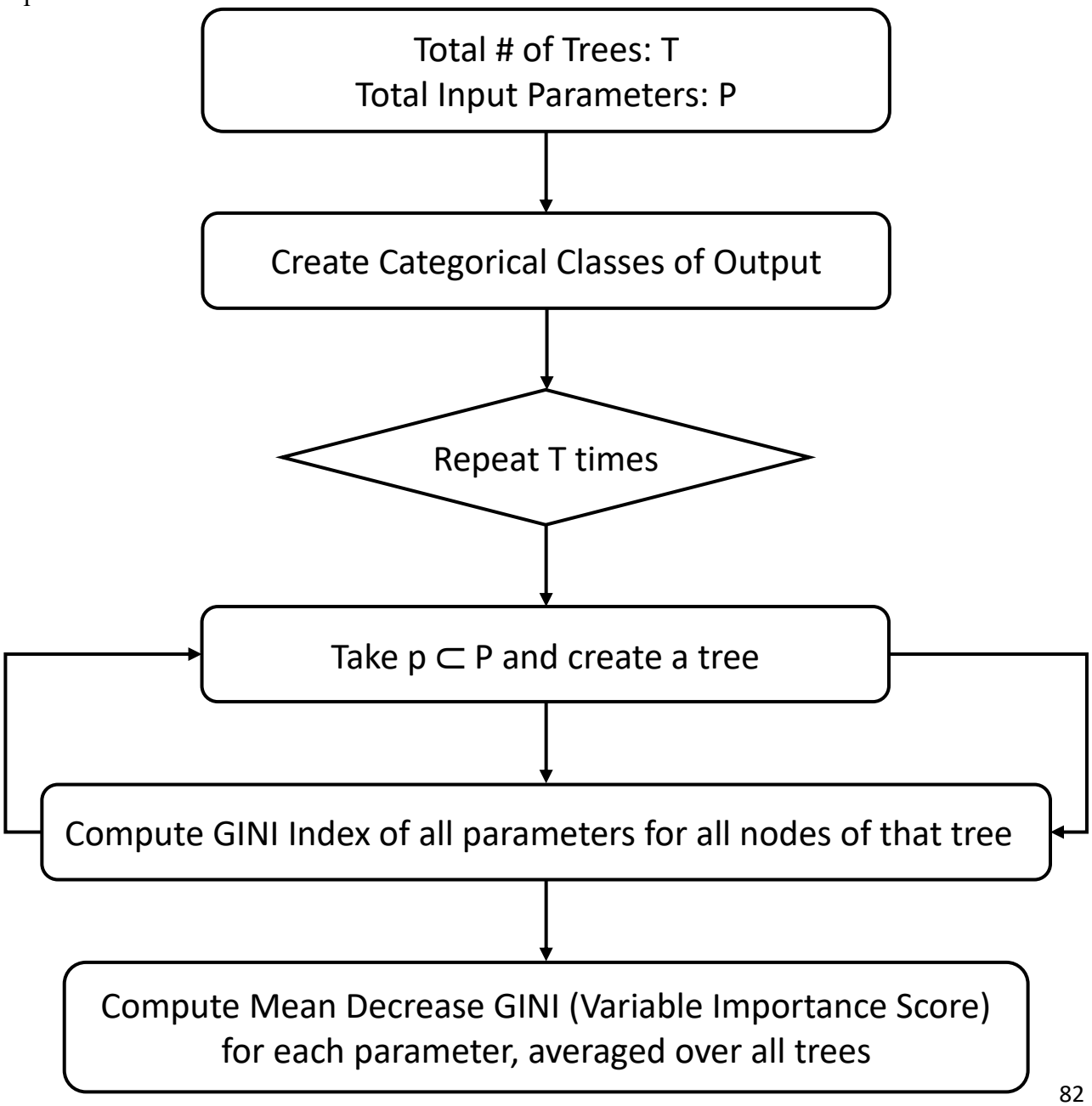

Figure 3.2. Top 25 parameters obtained by sensitivity analysis for Day 1. (A) Neutrophils. (B) Macrophages. (C) Fibroblasts. The biological function of each parameter is coded by the shade of the bar.

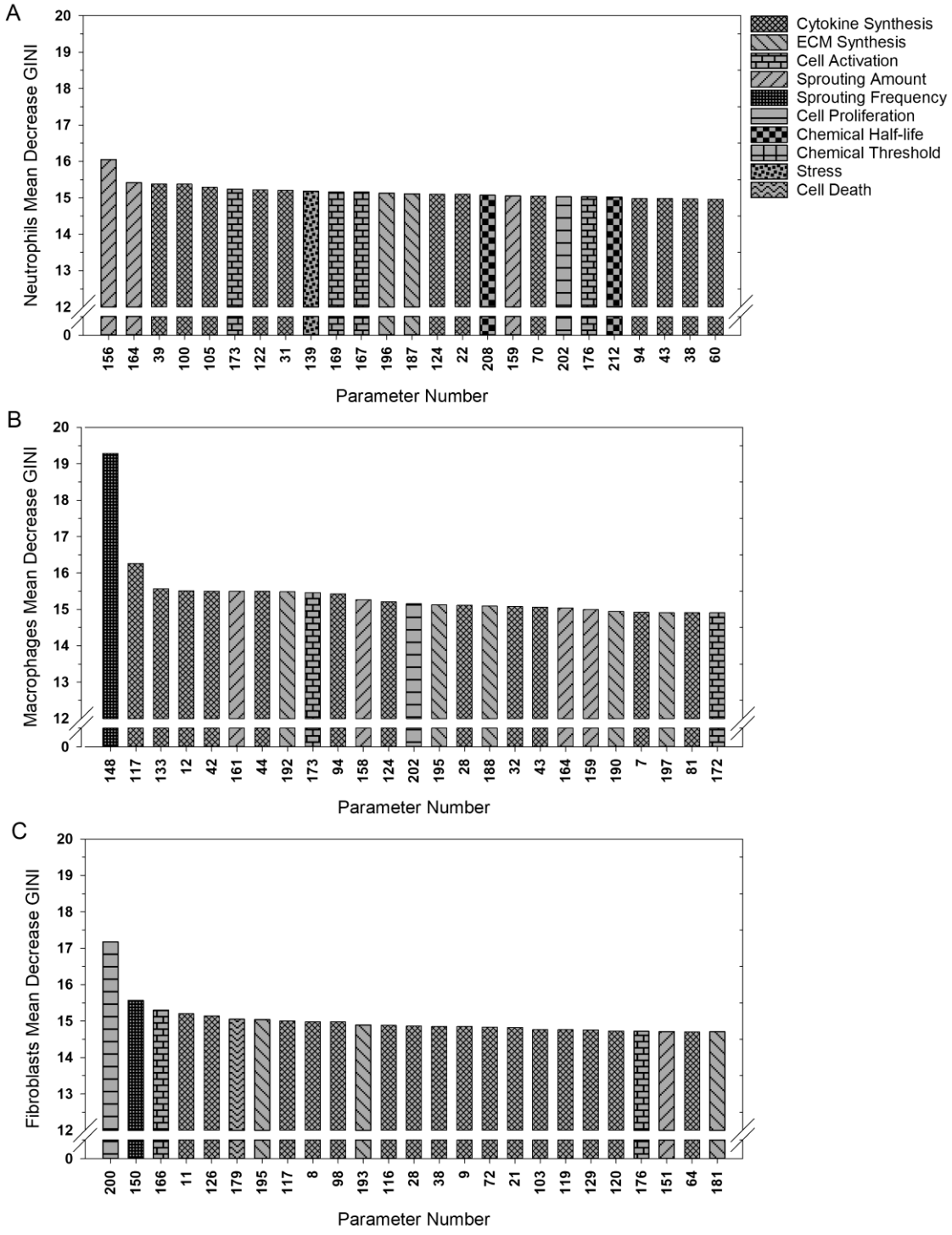

Figure 3.3. Flowchart for Calibration Strategy 1. * A total of 36 top parameters were ranked for each cell type at each time point (3 parameters x 3 cell types x 4 time points). However, twelve of them were overlapped across conditions. As a result, a total of 24 unique parameters were used for calibration.

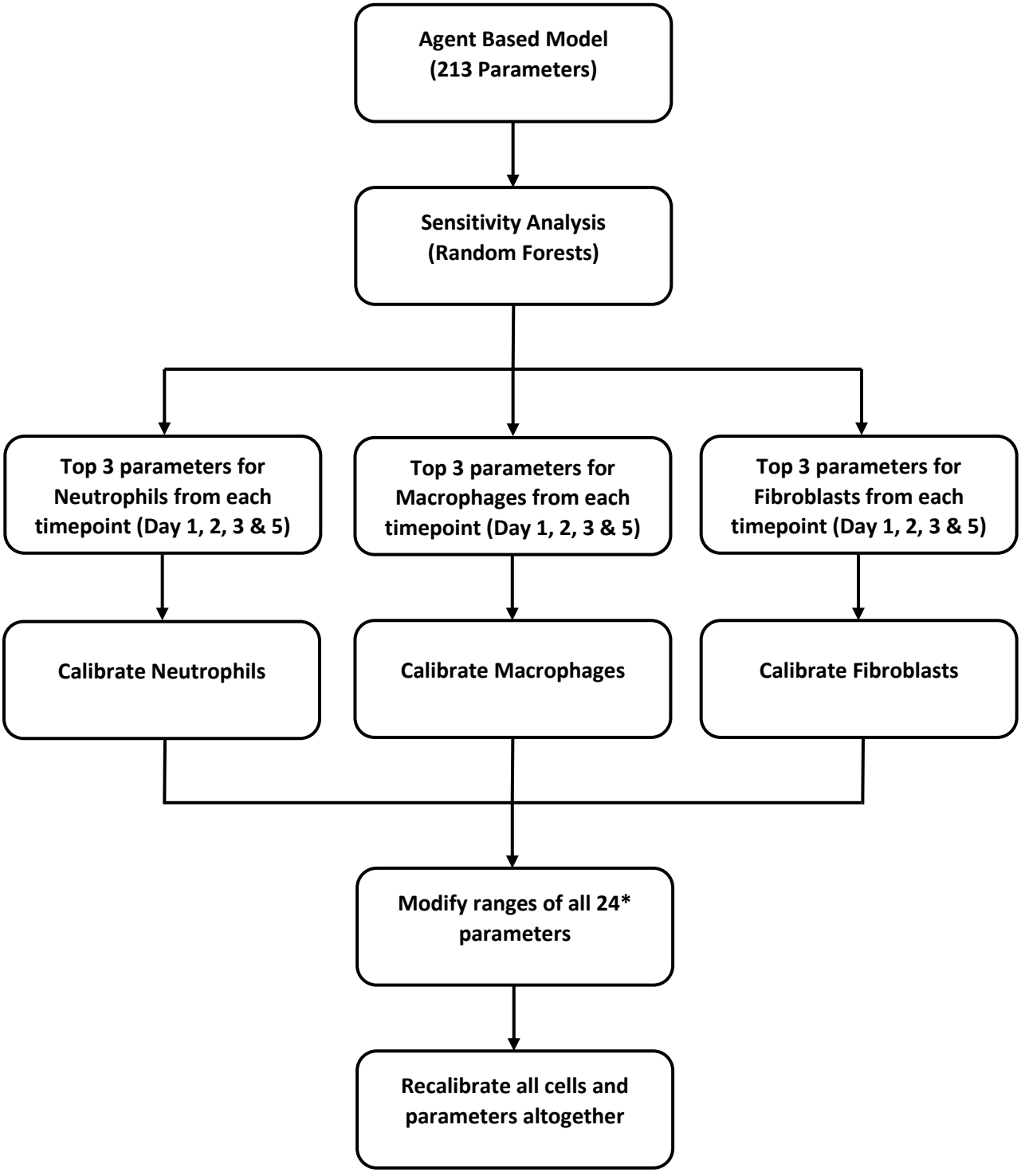

Figure 3.4. Flowchart for comparing two versions of Calibration Strategy 2. (A) Strategy 2a. (B) Strategy 2b. * A total of 36 top parameters were ranked for each cell type at each time point (3 parameters x 3 cell types x 4 time points). However, twelve of them were overlapped across conditions. As a result, a total of 24 unique parameters were used for calibration.

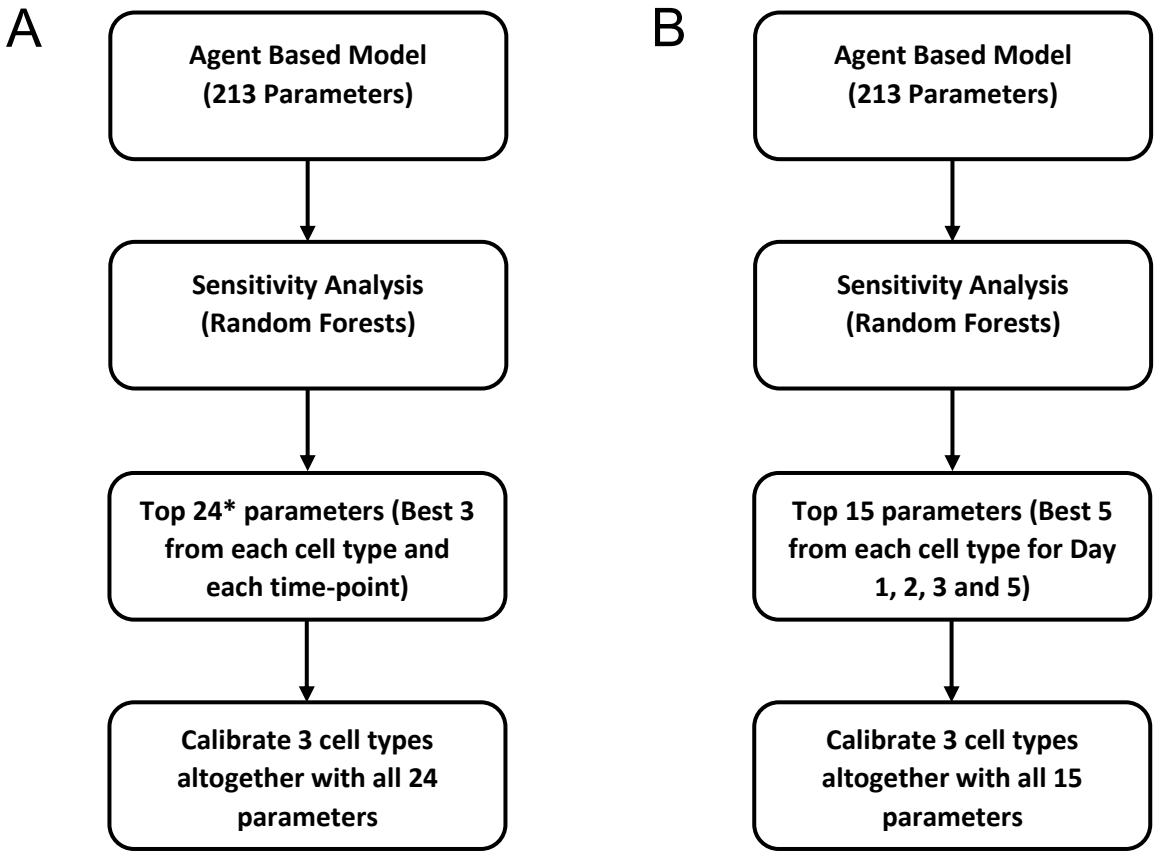

Figure 3.5. Comparison of cell dynamics between empirical and simulation data using (A-C) Strategy 1, (D-F) Strategy 2a and (G-I) Strategy 2b.

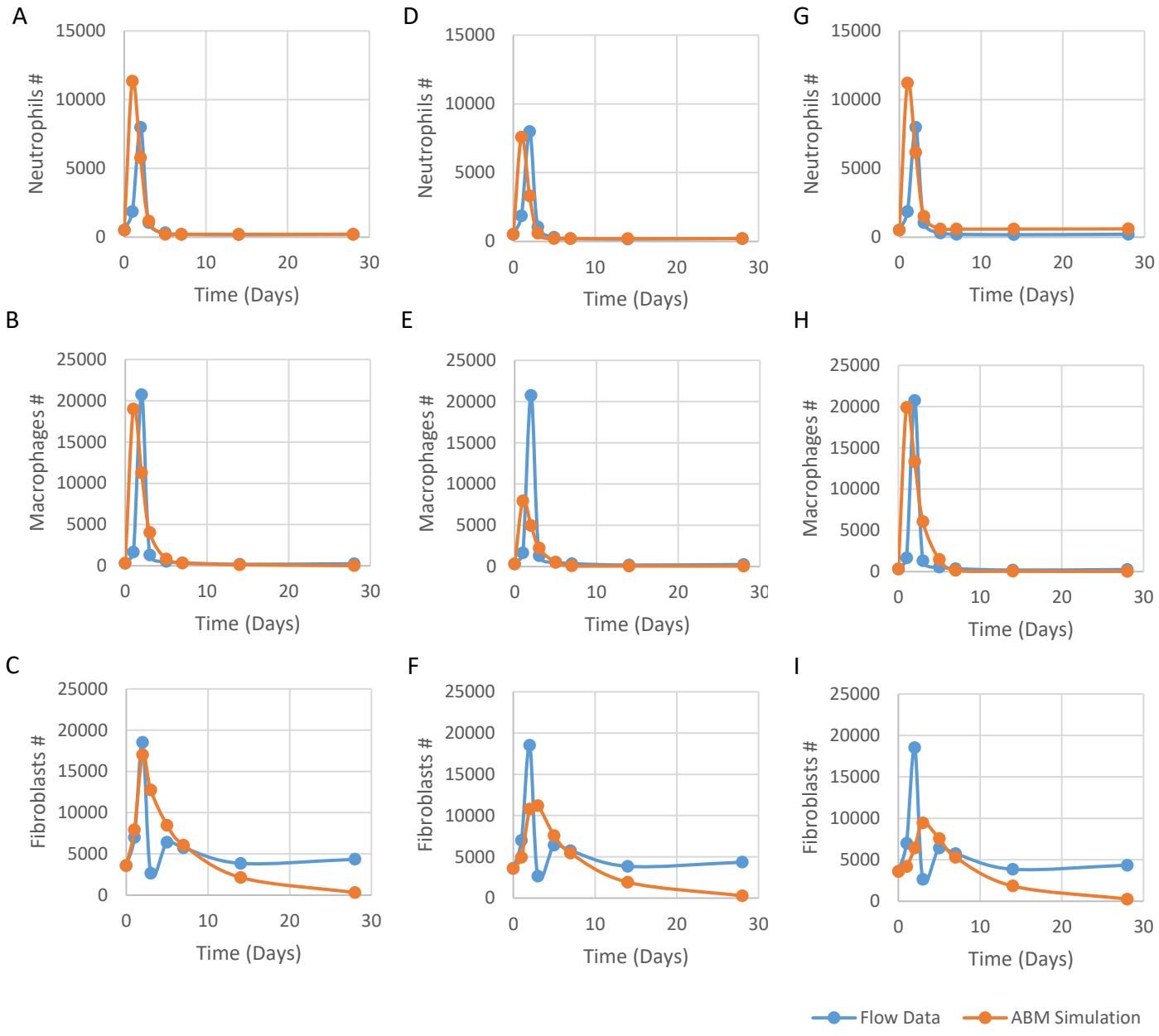

Figure 3.6. Empirical and model-predicted trajectories of cell types using Strategy 1

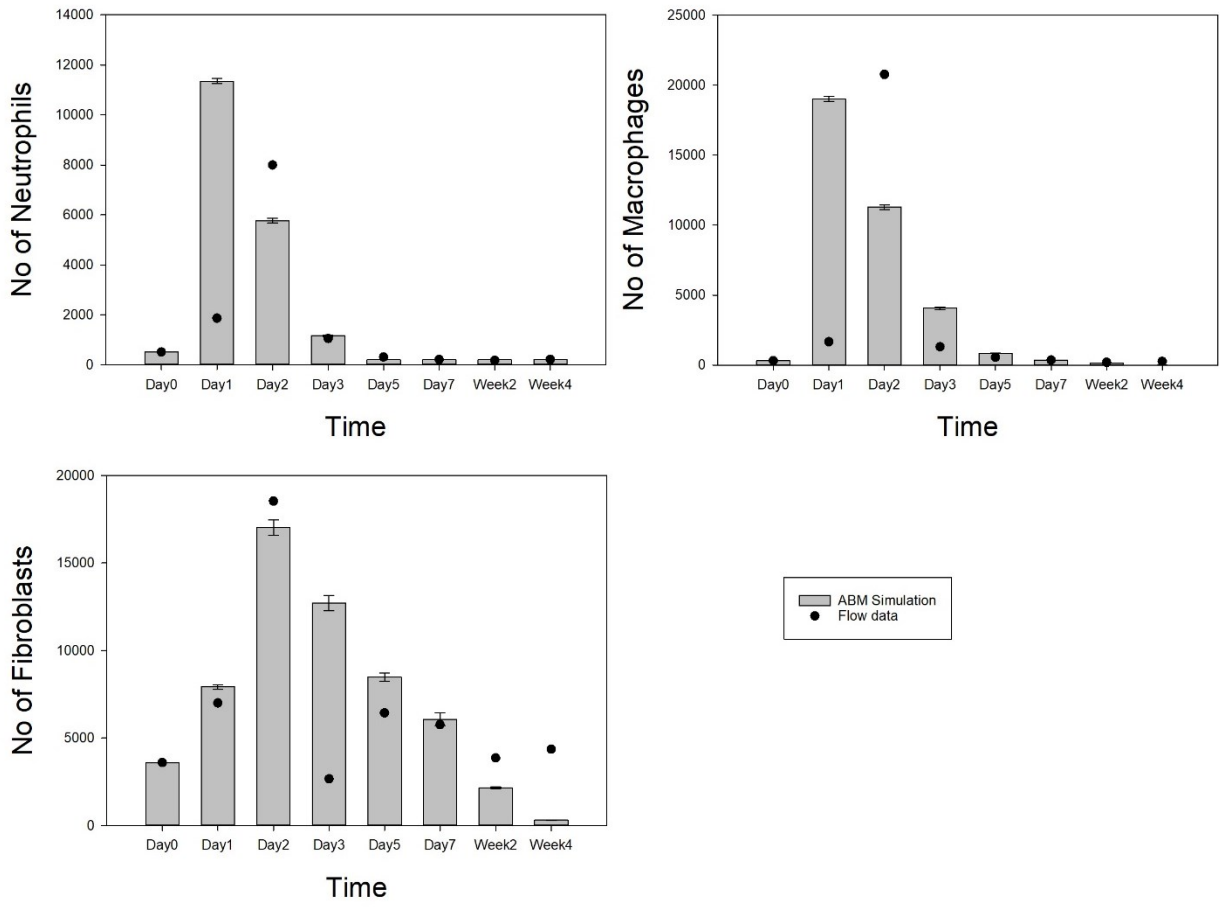

3.13 SUPPORTING INFORMATION

S3.1 Figure. Top 25 parameters obtained by sensitivity analysis for Day 2. (A) Neutrophils. (B) Macrophages. (C) Fibroblasts. The biological function of each parameter is coded by the shade of the bar.

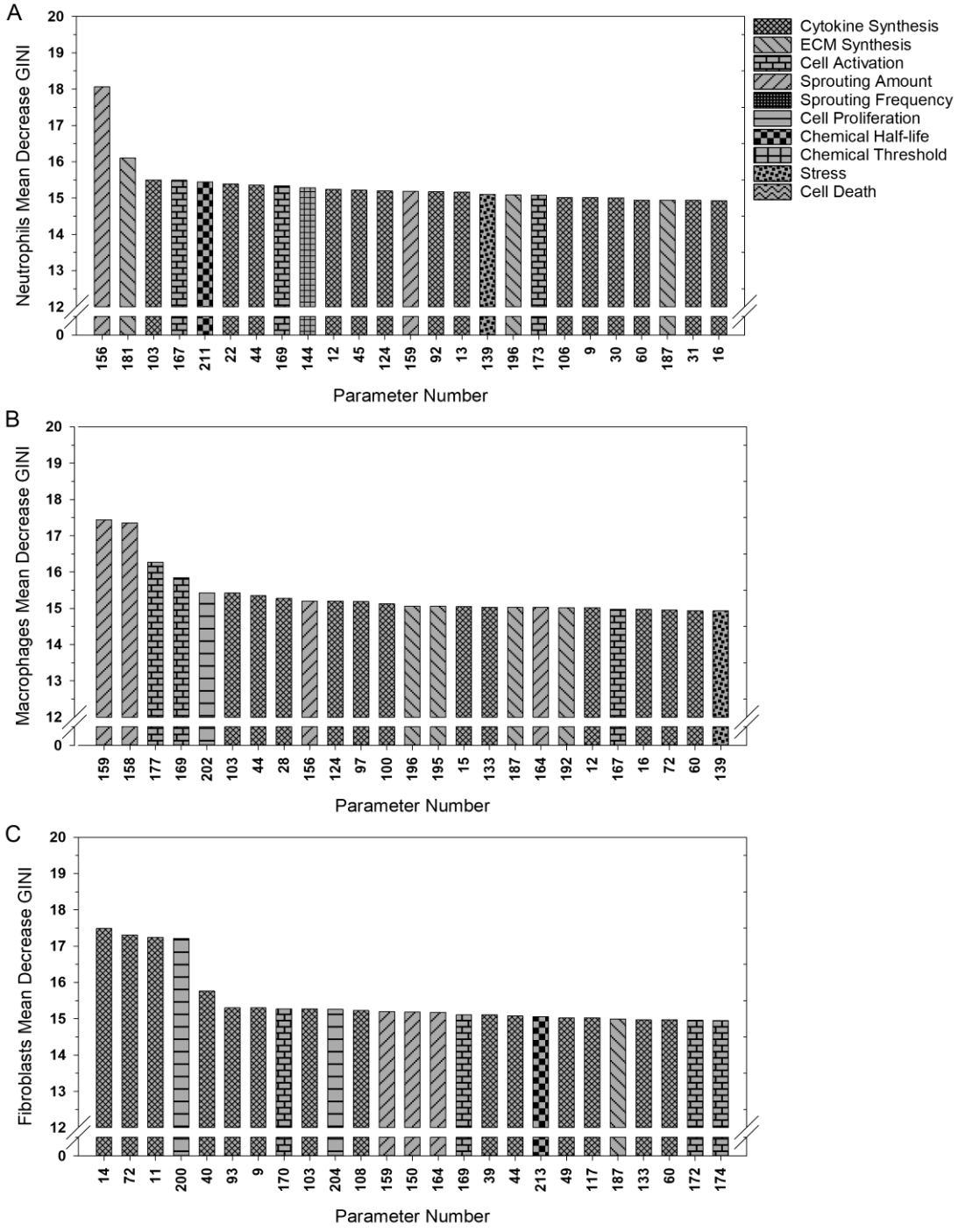

S3.2 Figure. Top 25 parameters obtained by sensitivity analysis for Day 3. (A) Neutrophils. (B) Macrophages. (C) Fibroblasts. The biological function of each parameter is coded by the shade of the bar.

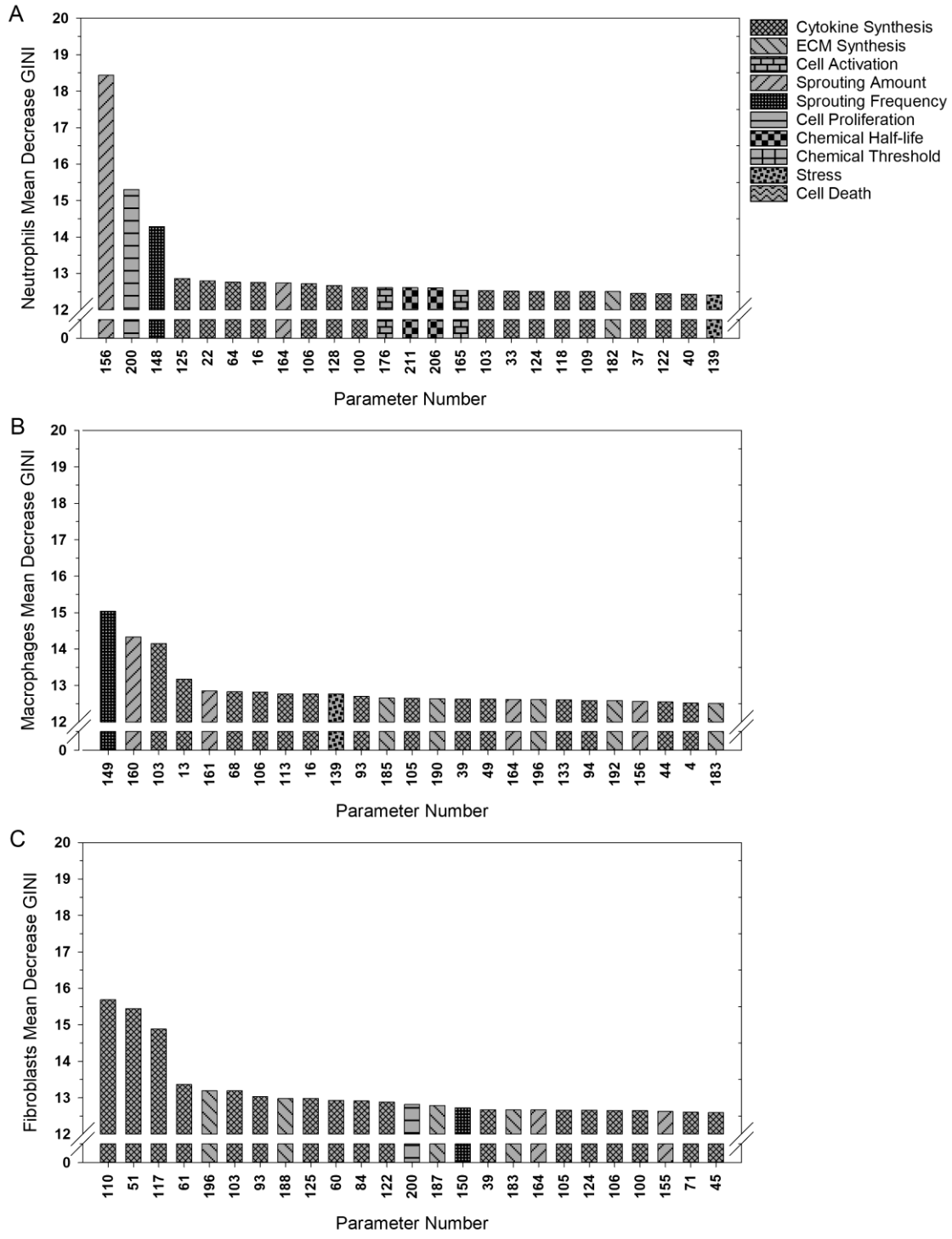

S3.3 Figure. Top 25 parameters obtained by sensitivity analysis for Day 5. (A) Neutrophils. (B) Macrophages. (C) Fibroblasts. The biological function of each parameter is coded by the shade of the bar.

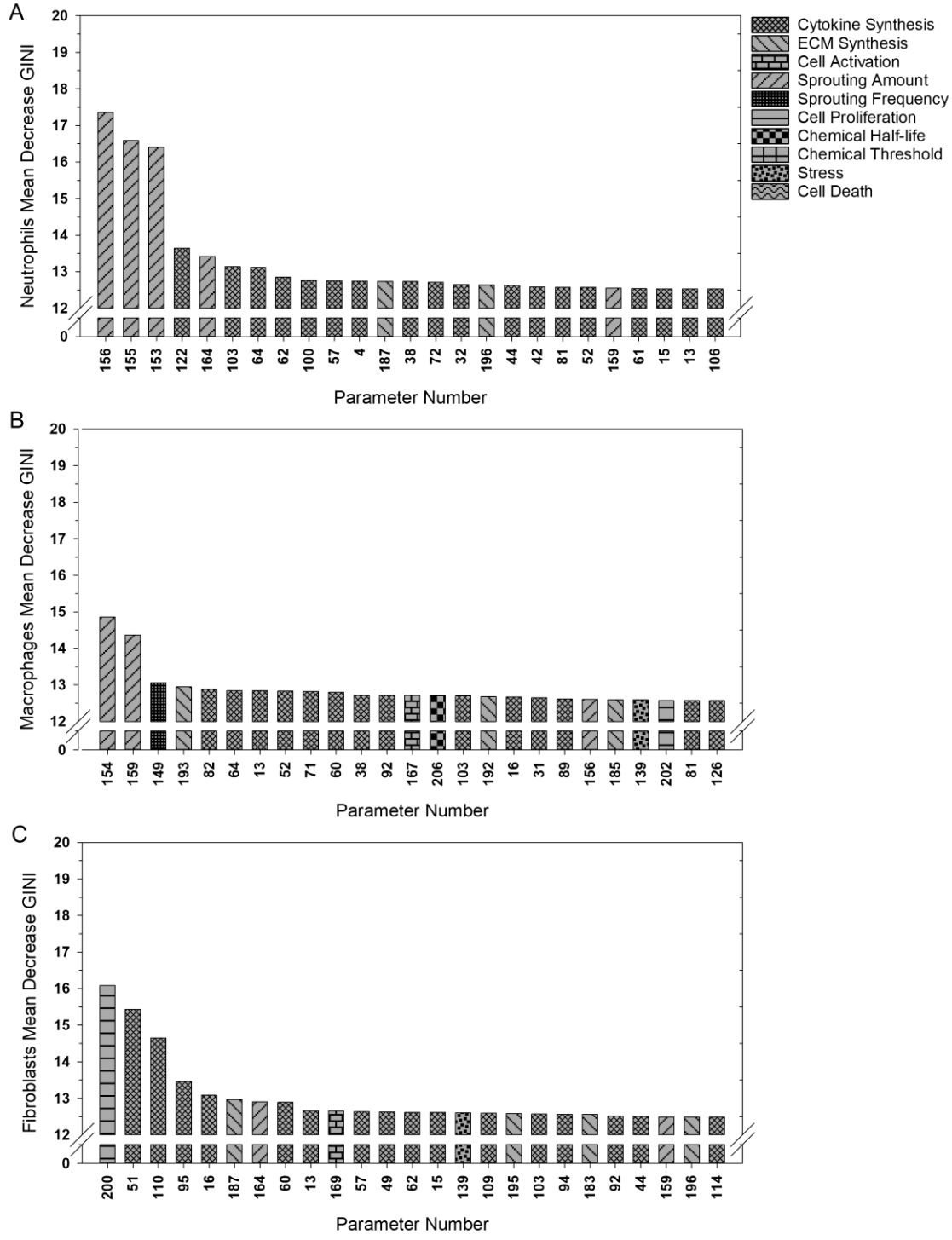

S3.4 Table. Functional Classification of Parameters Ranked by Sensitivity Analysis for Day 1. The number represents the number of parameters for specific function based on their ranking.

Cell Type	Biological Function	Parameters 1-50	Parameters 51-100	Parameters 101-150	Parameters 151-213
Neutrophils	Cytokine Synthesis	30	34	41	33
	ECM Synthesis	6	4	2	7
	Cell Activation	6	1	1	6
	Sprouting Amount	4	3	2	5
	Sprouting Frequency	0	0	0	6
	Cell Proliferation	1	2	1	2
	Chemical Half-life	2	2	2	2
	Chemical Threshold	0	1	0	1
	Stress	1	2	1	0
	Cell Death	0	1	0	1
Macrophages	Cytokine Synthesis	26	33	35	44
	ECM Synthesis	9	2	3	5
	Cell Activation	5	5	2	2
	Sprouting Amount	5	3	6	0
	Sprouting Frequency	1	0	0	5
	Cell Proliferation	2	0	0	4
	Chemical Half-life	0	4	3	1
	Chemical Threshold	1	0	0	1
	Stress	0	2	1	1
	Cell Death	1	1	0	0
Fibroblasts	Cytokine Synthesis	36	29	36	37
	ECM Synthesis	4	3	4	8
	Cell Activation	3	4	4	3
	Sprouting Amount	1	7	3	3
	Sprouting Frequency	1	0	0	5
	Cell Proliferation	2	2	1	1
	Chemical Half-life	1	3	2	2
	Chemical Threshold	0	0	0	2
	Stress	1	1	0	2
	Cell Death	1	1	0	0

S3.5 Table. Functional Classification of Parameters Ranked by Sensitivity Analysis for Day 2. The number represents the number of parameters for specific function based on their ranking.

Cell Type	Biological Function	Parameters 1-50	Parameters 51-100	Parameters 101-150	Parameters 151-213
Neutrophils	Cytokine Synthesis	28	40	30	40
	ECM Synthesis	8	1	4	6
	Cell Activation	5	3	5	1
	Sprouting Amount	4	2	5	3
	Sprouting Frequency	0	0	0	6
	Cell Proliferation	1	2	1	2
	Chemical Half-life	2	0	4	2
	Chemical Threshold	1	0	0	1
	Stress	1	1	1	1
	Cell Death	0	1	0	1
Macrophages	Cytokine Synthesis	28	37	37	36
	ECM Synthesis	4	2	6	7
	Cell Activation	6	4	1	3
	Sprouting Amount	6	4	1	3
	Sprouting Frequency	0	0	0	6
	Cell Proliferation	3	0	1	2
	Chemical Half-life	1	2	3	2
	Chemical Threshold	0	1	0	1
	Stress	1	0	1	2
	Cell Death	1	0	0	1
Fibroblasts	Cytokine Synthesis	34	37	29	38
	ECM Synthesis	3	2	5	9
	Cell Activation	5	2	4	3
	Sprouting Amount	2	3	4	5
	Sprouting Frequency	1	0	0	5
	Cell Proliferation	3	2	1	0
	Chemical Half-life	1	0	5	2
	Chemical Threshold	1	0	1	0
	Stress	0	3	1	0
	Cell Death	0	1	0	1

S3.6 Table. Functional Classification of Parameters Ranked by Sensitivity Analysis for Day 3. The number represents the number of parameters for specific function based on their ranking.

Cell Type	Biological Function	Parameters 1-50	Parameters 51-100	Parameters 101-150	Parameters 151-213
Neutrophils	Cytokine Synthesis	32	35	30	41
	ECM Synthesis	3	1	7	8
	Cell Activation	4	7	2	1
	Sprouting Amount	3	5	3	3
	Sprouting Frequency	1	0	0	5
	Cell Proliferation	2	1	2	1
	Chemical Half-life	2	0	4	2
	Chemical Threshold	1	1	0	0
	Stress	2	0	0	2
	Cell Death	0	0	2	0
Macrophages	Cytokine Synthesis	35	37	32	34
	ECM Synthesis	5	5	3	6
	Cell Activation	4	1	5	4
	Sprouting Amount	4	3	3	4
	Sprouting Frequency	1	0	0	5
	Cell Proliferation	0	1	1	4
	Chemical Half-life	0	1	4	3
	Chemical Threshold	0	1	0	1
	Stress	1	1	0	2
	Cell Death	0	0	2	0
Fibroblasts	Cytokine Synthesis	31	36	38	33
	ECM Synthesis	7	3	1	8
	Cell Activation	2	5	1	6
	Sprouting Amount	5	2	2	5
	Sprouting Frequency	1	0	0	5
	Cell Proliferation	1	1	3	1
	Chemical Half-life	1	3	2	2
	Chemical Threshold	1	0	1	0
	Stress	1	0	2	1
	Cell Death	0	0	0	2

S3.7 Table. Functional Classification of Parameters Ranked by Sensitivity Analysis for Day 5. The number represents the number of parameters for specific function based on their ranking.

Cell Type	Biological Function	Parameters 1-50	Parameters 51-100	Parameters 101-150	Parameters 151-213
Neutrophils	Cytokine Synthesis	34	36	31	37
	ECM Synthesis	5	3	5	6
	Cell Activation	3	3	4	4
	Sprouting Amount	5	5	0	4
	Sprouting Frequency	0	0	0	6
	Cell Proliferation	1	1	2	2
	Chemical Half-life	2	1	3	2
	Chemical Threshold	0	1	1	0
	Stress	0	0	3	1
	Cell Death	0	0	1	1
Macrophages	Cytokine Synthesis	31	30	37	40
	ECM Synthesis	6	4	4	5
	Cell Activation	2	4	3	5
	Sprouting Amount	5	3	3	3
	Sprouting Frequency	1	0	0	5
	Cell Proliferation	1	2	1	2
	Chemical Half-life	2	4	2	0
	Chemical Threshold	1	0	0	1
	Stress	1	1	0	2
	Cell Death	0	2	0	0
Fibroblasts	Cytokine Synthesis	37	32	30	39
	ECM Synthesis	4	5	5	5
	Cell Activation	3	4	4	3
	Sprouting Amount	2	4	5	3
	Sprouting Frequency	0	0	0	6
	Cell Proliferation	2	2	1	1
	Chemical Half-life	1	1	4	2
	Chemical Threshold	0	1	0	1
	Stress	1	0	0	3
	Cell Death	0	1	1	0

CHAPTER 4: CONCLUSIONS AND FUTURE DIRECTIONS

Iatrogenic vocal fold scarring is one of the most perplexing complications in phonosurgery. Surgical injury triggers a cascade of cellular and molecular events in inflammation and healing. Due to the individual-specific response to injury, a computational tool could be useful to aid clinicians in tailoring the vocal treatment. Our research group has developed vocal fold agent-based models (VF-ABM) to numerically simulate the inflammation and repair response to surgical injury [59-63, 69]. Additional empirical data, however, are needed for model calibration and validation to make this tool useful for clinical application.

In particular, empirical data on the temporal dynamics of the vocal fold cell population were limited for the purpose of model development. In this thesis, rodent models were used to provide quantitative data of major cell populations after surgical vocal fold injury and repair. The data were then used to calibrate and validate our VF-ABM. Existing sensitivity analysis methods [e.g., One Parameter At a Time (OPAT), Fourier Amplitude Sensitivity Test (FAST) etc.] and calibration algorithms [e.g., Genetic Algorithm (GA), Particle Swamp Optimization (PSO), Bayesian approach etc.] are not optimal for large scale ABM as in our case herein. We thus proposed a new approach utilizing Random Forests and ROPE for sensitivity analysis and model calibration respectively. Random Forests were used as the sensitivity analysis method to identify most influential parameters to ABM outputs for cell populations. ROPE calibration using SPOTPY package was used to calibrate those parameter values to match the simulation data with the corresponding empirical flow cytometry data. Model calibration was implemented such that the

model's simulated trajectories of cells matched observed trajectories collected from flow cytometry experiments on cell phenotyping in injured rat vocal folds.

General agreement was observed when comparing the dynamics of empirical and simulated results qualitatively. Statistically, VF-ABM was accurate in predicting the empirical data for Day 7 with 100% accuracy for all cell counts, but not for longer time points. Additional empirical data are needed to better estimate the vocal fold fibroblast proliferation at both homeostatic and injurious conditions in order to improve the long-term prediction of fibroblasts in VF-ABM. In particular, rules related to sprouting amount and sprouting frequency of cells need to be refined to optimize model outputs of cell dynamics at homeostatic status.

Calibration strategy can be further optimized by using a hybrid approach. One plausible idea is to implement GA and ROPE simultaneously for each run, such that modified calibration algorithm will include both the features of genetic operators from GA and data depth from ROPE. As GA uses the natural selection process for estimating many possible solutions simultaneously, the model parameter values are progressively modified using genetic operators to optimize the model's fitness in predicting the empirical data [217, 218]. The concern of GA in parameter overfitting and result variations might be alleviated if a combined approach with ROPE and Random Forests is implemented.

In addition, ongoing research efforts continuously improve the biological representation of VF-ABM including fibroblast proliferation, fibroblast-to-myofibroblast transdifferentiation and spatial alignment of ECM fibers. Empirical research has been conducted in parallel to determine the effect of growth factors and mechanical stimulation on vocal fold fibroblast behavior and ECM organization. Results will help better estimate the production and remodeling of ECM proteins by

activated fibroblasts in the vocal folds. Further, comprehensive investigation related to the oscillating dynamics of fibroblast-myofibroblast transdifferentiation may reveal unknown signaling pathways and cell-ECM interactions that are specific to the microenvironment of vocal folds. In addition, functional studies are warranted to confirm if CD105+FSC-A++ cells behave as typical myofibroblasts known in the literature as indicated from our flow cytometry studies. All aforesaid experiments will contribute to the development of preventive and treatment strategies for iatrogenic vocal fold scarring, ultimately contributing to the advancement of computational medicine in voice disorders.

REFERENCES

1. Bhattacharyya, N., *The prevalence of voice problems among adults in the United States.* The Laryngoscope, 2014. **124**(10): p. 2359-2362.
2. Morris, M.A., et al., *Prevalence and etiologies of adult communication disabilities in the United States: Results from the 2012 National Health Interview Survey.* Disability and health journal, 2016. **9**(1): p. 140-144.
3. Verdolini, K. and L.O. Ramig, *Occupational risks for voice problems.* Logopedics Phoniatrics Vocology, 2001. **26**(1): p. 37-46.
4. Benninger, M.S., et al., *Vocal fold scarring: Current concepts and management.* Otolaryngology-Head and Neck Surgery, 1996. **115**(5): p. 474-482.
5. Rosen, C.A., *Vocal Fold Scar*, in *The Otolaryngologica Clinics of North America. Voice Disorders and Phonosurgery*, C.A. Rosen and T. Murry, Editors. 2000, W.B. Saunders: Philadelphia.
6. Hirano, S., *Current treatment of vocal fold scarring.* Curr Opin Otolaryngol Head Neck Surg, 2005. **13**(3): p. 143-7.
7. Shin, Y.S., et al., *Persistent dysphonia after laryngomicrosurgery for benign vocal fold disease.* Clin Exp Otorhinolaryngol, 2013. **6**(3): p. 166-70.
8. Woo, P., et al., *Diagnosis and treatment of persistent dysphonia after laryngeal surgery: a retrospective analysis of 62 patients.* Laryngoscope, 1994. **104**(9): p. 1084-91.
9. Perouse, A.R. and B. Coulombeau, *Iatrogenic scarring of the vocal folds after phonosurgery for benign lesions. A descriptive study of 108 patients.* Rev Laryngol Otol Rhinol (Bord), 2014. **135**(2): p. 57-61.
10. Hansen, J.K. and S.L. Thibeault, *Current understanding and review of the literature: vocal fold scarring.* J Voice, 2006. **20**(1): p. 110-20.
11. Kent, R.D., *The MIT encyclopedia of communication disorders*. 2004: MIT Press.
12. Gray, S.D., *Cellular physiology of the vocal folds.* Otolaryngologic Clinics of North America, 2000. **33**(4): p. 679-697.
13. Gray, S.D., et al., *Biomechanical and histologic observations of vocal fold fibrous proteins.* Annals of Otology, Rhinology & Laryngology, 2000. **109**(1): p. 77-85.
14. Zeitels, S.M. and G.B. Healy, *Laryngology and phonosurgery.* New England Journal of Medicine, 2003. **349**(9): p. 882-892.
15. Welham, N.V., et al., *A rat excised larynx model of vocal fold scar.* J Speech Lang Hear Res, 2009. **52**(4): p. 1008-20.
16. Tateya, T., et al., *Postnatal development of rat vocal folds.* Ann Otol Rhinol Laryngol, 2006. **115**(3): p. 215-24.
17. Hirano, S., et al., *Regeneration of aged vocal folds with basic fibroblast growth factor in a rat model: a preliminary report.* Ann Otol Rhinol Laryngol, 2005. **114**(4): p. 304-8.
18. Tateya, I., et al., *Cell production in injured vocal folds: a rat study.* Ann Otol Rhinol Laryngol, 2006. **115**(2): p. 135-43.
19. Tateya, T., et al., *Histological study of acute vocal fold injury in a rat model.* Ann Otol Rhinol Laryngol, 2006. **115**(4): p. 285-92.
20. Tateya, T., et al., *Histologic characterization of rat vocal fold scarring.* Ann Otol Rhinol Laryngol, 2005. **114**(3): p. 183-91.
21. Tateya, I., T. Tateya, and D.M. Bless, *Homeostasis of hyaluronic acid in scarred rat vocal folds*, in *International Conference on voice Physiology and Biomechanics*. 2004: Marseille-France.

22. Ohno, T., et al., *Effect of hepatocyte growth factor on gene expression of extracellular matrix during wound healing of the injured rat vocal fold.* Ann Otol Rhinol Laryngol, 2008. **117**(9): p. 696-702.
23. Ohno, T., et al., *Expression of extracellular matrix proteins in the vocal folds and bone marrow derived stromal cells of rats.* Eur Arch Otorhinolaryngol, 2008. **265**(6): p. 669-74.
24. Ohno, T., S. Hirano, and B. Rousseau, *Gene expression of transforming growth factor-beta1 and hepatocyte growth factor during wound healing of injured rat vocal fold.* Laryngoscope, 2009. **119**(4): p. 806-10.
25. Ohno, T., S. Hirano, and B. Rousseau, *Extracellular matrix gene expression during wound healing of the injured rat vocal fold.* Otolaryngol Head Neck Surg, 2009. **140**(5): p. 757-61.
26. Welham, N.V., et al., *Proteomic changes in rat thyroarytenoid muscle induced by botulinum neurotoxin injection.* Proteomics, 2008. **8**(9): p. 1933-44.
27. Boseley, M.E. and C.J. Hartnick, *Development of the human true vocal fold: depth of cell layers and quantifying cell types within the lamina propria.* Annals of Otology, Rhinology & Laryngology, 2006. **115**(10): p. 784-788.
28. Catten, M., et al., *Analysis of cellular location and concentration in vocal fold lamina propria.* Otolaryngology—Head and Neck Surgery, 1998. **118**(5): p. 663-667.
29. Li‐Jessen, N.Y., et al., *Cellular source and proinflammatory roles of high‐mobility group box 1 in surgically injured rat vocal folds.* The Laryngoscope, 2016.
30. King, S.N., J. Guille, and S.L. Thibeault, *Characterization of the leukocyte response in acute vocal fold injury.* PloS one, 2015. **10**(10): p. e0139260.
31. Ling, C., et al., *Alteration in cellular morphology, density and distribution in rat vocal fold mucosa following injury.* Wound Repair and Regeneration, 2010. **18**(1): p. 89-97.
32. Cho, J.-H., et al., *Efficacy and Safety of Adjunctive Steroid Injection After Microsurgical Removal of Benign Vocal Fold Lesions.* Journal of Voice, 2017.
33. Tang, S.S. and S.L. Thibeault, *Timing of voice therapy: a primary investigation of voice outcomes for surgical benign vocal fold lesion patients.* Journal of Voice, 2017. **31**(1): p. 129. e1-129. e7.
34. Kanazawa, T., et al., *Single injection of basic fibroblast growth factor to treat severe vocal fold lesions and vocal fold paralysis.* The Laryngoscope, 2015. **125**(10): p. E338-E344.
35. Caffier, P.P., et al., *The use of injectable calcium hydroxylapatite in the surgically pretreated larynx with glottal insufficiency.* The Laryngoscope, 2017. **127**(5): p. 1125-1130.
36. Hirano, S., et al., *Regenerative phonosurgical treatments for vocal fold scar and sulcus with basic fibroblast growth factor.* The Laryngoscope, 2013. **123**(11): p. 2749-2755.
37. Bless, D.M. and N.V. Welham, *Characterization of vocal fold scar formation, prophylaxis and treatment using animal models.* Current opinion in otolaryngology & head and neck surgery, 2010. **18**(6): p. 481.
38. Bless, D.M., et al., *Growth factor therapy for vocal fold scarring in a canine model.* Annals of Otology, Rhinology & Laryngology, 2004. **113**(10): p. 777-785.
39. Hirano, S., *Current treatment of vocal fold scarring.* Current opinion in otolaryngology & head and neck surgery, 2005. **13**(3): p. 143-147.
40. Jia, X., et al., *Synthesis and characterization of in situ cross-linkable hyaluronic acid-based hydrogels with potential application for vocal fold regeneration.* Macromolecules, 2004. **37**(9): p. 3239-3248.
41. Clermont, G., et al., *In silico design of clinical trials: a method coming of age.* Crit Care Med, 2004. **32**(10): p. 2061-70.
42. Kumar, R., et al., *The dynamics of acute inflammation.* J Theor Biol, 2004. **230**(2): p. 145-55.
43. Vodovotz, Y., et al., *In silico models of acute inflammation in animals.* Shock, 2006. **26**(3): p. 235-44.

44. Vodovotz, Y., et al., *Translational systems approaches to the biology of inflammation and healing.* Immunopharmacol. and Immunotoxicol, 2010. **32**: p. 181-195.
45. Mi, Q., et al., *Translational systems biology of inflammation: applications to personalized medicine.* Personalized Medicine, 2010. **7**(5): p. 549-559.
46. Li, N.Y., et al., *Translational systems biology and voice pathophysiology.* The Laryngoscope, 2010. **120**(3): p. 511-515.
47. Tepole, A.B. and E. Kuhl, *Systems-based approaches toward wound healing.* Pediatric research, 2013. **73**(4-2): p. 553.
48. Diaz-Beltran, L., et al., *Systems biology as a comparative approach to understand complex gene expression in neurological diseases.* Behavioral Sciences, 2013. **3**(2): p. 253-272.
49. Prokop, A. and B. Csukás, *Systems Biology: Integrative Biology and Simulation Tools*. Vol. 1. 2013: Springer Science & Business Media.
50. Pidko, E.A., *Toward the Balance between the Reductionist and Systems Approaches in Computational Catalysis: Model versus Method Accuracy for the Description of Catalytic Systems*. 2017, ACS Publications.
51. Draghici, S., et al., *A systems biology approach for pathway level analysis.* Genome research, 2007. **17**(10): p. 1537-1545.
52. Vodovotz, Y., et al., *Translational systems biology of inflammation.* PLoS computational biology, 2008. **4**(4): p. e1000014.
53. Bonabeau, E., *Agent-based modeling: Methods and techniques for simulating human systems.* Proceedings of the National Academy of Sciences, 2002. **99**(suppl 3): p. 7280-7287.
54. Kitano, H., *Computational systems biology.* Nature, 2002. **420**(6912): p. 206.
55. De Castro, L.N. and J. Timmis, *Artificial immune systems: a new computational intelligence approach*. 2002: Springer Science & Business Media.
56. Auffray, C., Z. Chen, and L. Hood, *Systems medicine: the future of medical genomics and healthcare.* Genome medicine, 2009. **1**(1): p. 2.
57. Hood, L. and M. Flores, *A personal view on systems medicine and the emergence of proactive P4 medicine: predictive, preventive, personalized and participatory.* New biotechnology, 2012. **29**(6): p. 613-624.
58. *New Roadmap Emphasis Areas for 2008*. 2007; Available from: http://nihroadmap.nih.gov/2008initiatives.asp.
59. Li, N.Y.K., *Biosimulation of vocal fold inflammation and healing*, in *Communication Science and Disorders*. 2009, University of Pittsburgh: Pittsburgh.
60. Li, N.Y.K., et al., *Translational systems biology and voice pathophysiology.* Laryngoscope, 2010. **120**(3): p. 511-5.
61. Li, N.Y.K., et al., *A patient-specific in silico model of inflammation and healing tested in acute vocal fold injury.* PLoS One, 2008. **3**(7): p. e2789.
62. Li, N.Y.K., et al., *Biosimulation of acute phonotrauma: an extended model.* Laryngoscope, 2011. **121**(11): p. 2418-2428.
63. Li, N.Y.K., et al., *Biosimulation of inflammation and healing in surgically injured vocal folds.* Ann Otol Rhinol Laryngol, 2010. **119**(6): p. 412-423.
64. Seekhao, N., et al., *High-Performance Agent-based Modeling Applied to Vocal Fold Inflammation and Repair.* Frontiers in Physiology, 2018. **9**: p. 304.
65. Seekhao, N., et al., *In Situ Visualization for 3D Agent-Based Vocal Fold Inflammation and Repair Simulation.* Supercomputing frontiers and innovations, 2017. **4**(3): p. 68.
66. Seekhao, N., et al. *Real-time agent-based modeling simulation with in-situ visualization of complex biological systems: A case study on vocal fold inflammation and healing*. in *Parallel and Distributed Processing Symposium Workshops, 2016 IEEE International*. 2016. IEEE.

67. An, G., et al., *Agent‐based models in translational systems biology.* Wiley Interdisciplinary Reviews: Systems Biology and Medicine, 2009. **1**(2): p. 159-171.
68. Helbing, D., I. Farkas, and T. Vicsek, *Simulating dynamical features of escape panic.* Nature, 2000. **407**(6803): p. 487.
69. Tang, S.S., et al., *Mathematical model of vocal fold injury and repair.* in review.
70. Welham, N.V., et al., *Inflammatory factor profiles one hour following vocal fold injury.* Ann Otol Rhinol Laryngol, 2008. **117**(2): p. 145-52.
71. Lim, X., et al., *Changes in cytokine signaling and extracellular matrix production induced by inflammatory factors in cultured vocal fold fibroblasts.* Ann Otol Rhinol Laryngol, 2008. **117**(3): p. 227-38.
72. Roy, N., et al., *Voice disorders in teachers and the general population: effects on work performance, attendance, and future career choices.* Journal of Speech, Language, and Hearing Research, 2004. **47**: p. 542-551.
73. NIDCD, *Voice, Speech, and Language Quick Statistics*. 2012.
74. Ramig, L.O. and K. Verdolini, *Treatment efficacy: voice disorders.* Journal of Speech, Language, and Hearing Research, 1998. **41**(1): p. S101-S116.
75. Roy, N., et al., *Voice disorders in the general population: prevalence, risk factors, and occupational impact.* Laryngoscope, 2005. **115**(11): p. 1988-95.
76. Zeitels, S.M., et al., *Management of common voice problems: Committee report.* Otolaryngology - head and neck surgery, 2002. **126**(4): p. 333-48.
77. Farrell, N.F. and M.S. Clary, *Surgical Management of Phonotraumatic Lesions: Current Techniques.* Current Otorhinolaryngology Reports, 2016. **4**(3): p. 149-156.
78. Witte, M.B. and A. Barbul, *General principles of wound healing.* Surgical Clinics of North America, 1997. **77**(3): p. 509-528.
79. Cohen, K., R. Diegelmann, and W. Lindblad, *Wound Healing: Biochemical and Clinical Aspects*. 1992, Philadelphia: W.B. Saunders.
80. Hackham, D.J. and H.R. Ford, *Cellular, Biochemical, and Clinical Aspects of Wound Healing.* Surgical Infections, 2002. **3**(Supplement.1): p. S23-S35.
81. Diegelmann, R.F. and M.C. Evans, *Wound healing: an overview of acute, fibrotic and delayed healing.* Front Biosci, 2004. **9**: p. 283-9.
82. Broughton 2nd, G., J.E. Janis, and C.E. Attinger, *The basic science of wound healing.* Plastic and reconstructive surgery, 2006. **117**(7 Suppl): p. 12S-34S.
83. Kirsner, R.S. and W. Eaglstein, *The wound healing process.* Dermatologic clinics, 1993. **11**(4): p. 629-640.
84. Li, N.Y., B.J. Lee, and S.L. Thibeault, *Temporal and spatial expression of high‐mobility group box 1 in surgically injured rat vocal folds.* The Laryngoscope, 2012. **122**(2): p. 364-369.
85. Yamashita, M., D.M. Bless, and N.V. Welham, *Morphological and extracellular matrix changes following vocal fold injury in mice.* Cells Tissues Organs, 2010. **192**(4): p. 262-271.
86. Hirano, S., et al., *Histologic characterization of human scarred vocal folds.* Journal of Voice, 2009. **23**(4): p. 399-407.
87. King, S.N., et al., *Macrophage Response to Allogeneic Adipose Tissue-Derived Stromal Cells in Hyaluronan-Based Hydrogel in a Porcine Vocal Fold Injury Model.* Annals of Otology, Rhinology & Laryngology, 2017: p. 0003489417702923.
88. Lee, Y.C., et al., *Investigation of nanostructural changes following acute injury using atomic force microscopy in rabbit vocal folds.* Microscopy research and technique, 2015. **78**(7): p. 569-576.
89. Welham, N.V., et al., *Inflammatory factor profiles one hour following vocal fold injury.* The Annals of otology, rhinology, and laryngology, 2008. **117**(2): p. 145-152.

90. Thibeault, S.L., et al., *Histologic and rheologic characterization of vocal fold scarring.* Journal of Voice, 2002. **16**(1): p. 96-104.
91. Lim, X., et al., *Changes in cytokine signaling and extracellular matrix production induced by inflammatory factors in cultured vocal fold fibroblasts.* Annals of Otology, Rhinology & Laryngology, 2008. **117**(3): p. 227-238.
92. Lim, J.-Y., et al., *Regulation of wound healing by granulocyte-macrophage colony-stimulating factor after vocal fold injury.* PloS one, 2013. **8**(1): p. e54256.
93. Hertegård, S., et al., *Viscoelastic and histologic properties in scarred rabbit vocal folds after mesenchymal stem cell injection.* The Laryngoscope, 2006. **116**(7): p. 1248-1254.
94. Chen, X. and S.L. Thibeault, *Biocompatibility of a synthetic extracellular matrix on immortalized vocal fold fibroblasts in 3-D culture.* Acta biomaterialia, 2010. **6**(8): p. 2940-2948.
95. Duflo, S., et al., *Effect of a synthetic extracellular matrix on vocal fold lamina propria gene expression in early wound healing.* Tissue engineering, 2006. **12**(11): p. 3201-3207.
96. Suehiro, A., et al., *Effects of basic fibroblast growth factor on rat vocal fold fibroblasts.* Annals of Otology, Rhinology & Laryngology, 2010. **119**(10): p. 690-696.
97. Suzuki, R., et al., *Prevention of vocal fold scarring by local application of basic fibroblast growth factor in a rat vocal fold injury model.* The Laryngoscope, 2016.
98. Hiwatashi, N., et al., *SMAD3 expression and regulation of fibroplasia in vocal fold injury.* The Laryngoscope, 2017.
99. Tateya, I., et al., *Histological effect of basic fibroblast growth factor on chronic vocal fold scarring in a rat model.* Clinical and experimental otorhinolaryngology, 2016. **9**(1): p. 56.
100. Yiu, E.M., et al., *Wound‐healing effect of acupuncture for treating phonotraumatic vocal pathologies: A cytokine study.* The Laryngoscope, 2016. **126**(1): p. E18-E22.
101. Kaneko, M., et al., *Protective Effect of Astaxanthin on Vocal Fold Injury and Inflammation Due to Vocal Loading: A Clinical Trial.* Journal of Voice, 2017. **31**(3): p. 352-358.
102. Rohlfs, A.-K., et al., *Quantification of change in vocal fold tissue stiffness relative to depth of artificial damage.* Logopedics Phoniatrics Vocology, 2016: p. 1-10.
103. Allen, J., *Response of an ovine laryngeal injury model to a novel fibrosis inhibitor.* ANZ Journal of Surgery, 2016.
104. Chang, Z., et al., *TGF-β3 modulates the inflammatory environment and reduces scar formation following vocal fold mucosal injury in rats.* Disease models & mechanisms, 2014. **7**(1): p. 83-91.
105. Heris, H.K., et al., *Microstructural and mechanical characterization of scarred vocal folds.* Journal of biomechanics, 2015. **48**(4): p. 708-711.
106. Kojima, T., et al., *Quantification of acute vocal fold epithelial surface damage with increasing time and magnitude doses of vibration exposure.* PloS one, 2014. **9**(3): p. e91615.
107. Muñoz-Pinto, D., P. Whittaker, and M.S. Hahn, *Lamina propria cellularity and collagen composition: an integrated assessment of structure in humans.* Annals of Otology, Rhinology & Laryngology, 2009. **118**(4): p. 299-306.
108. Ling, C., et al., *Alteration in cellular morphology, density and distribution in rat vocal fold mucosa following injury.* Wound Repair Regen, 2010. **18**(1): p. 89-97.
109. Ling, C., et al., *Reactive response of fibrocytes to vocal fold mucosal injury in rat.* Wound Repair Regen, 2010. **18**(5): p. 514-23.
110. Tateya, T., et al., *Histological study of acute vocal fold injury in a rat model.* Annals of Otology, Rhinology & Laryngology, 2006. **115**(4): p. 285-292.
111. Branski, R.C., et al., *Acute vocal fold wound healing in a rabbit model.* Annals of Otology, Rhinology & Laryngology, 2005. **114**(1): p. 19-24.
112. Stevens, S.L., et al., *The use of flow cytometry to evaluate temporal changes in inflammatory cells following focal cerebral ischemia in mice.* Brain research, 2002. **932**(1): p. 110-119.

113. Perfetto, S.P., P.K. Chattopadhyay, and M. Roederer, *Seventeen-colour flow cytometry: unravelling the immune system.* Nature Reviews Immunology, 2004. **4**(8): p. 648-655.
114. Loken, M.R. and A.M. Stall, *Flow cytometry as an analytical and preparative tool in immunology.* Journal of immunological methods, 1982. **50**(3): p. R85-R112.
115. Brown, M. and C. Wittwer, *Flow cytometry: principles and clinical applications in hematology.* Clinical chemistry, 2000. **46**(8): p. 1221-1229.
116. Macey, M.G., *Flow Cytometry*. 2007: Springer.
117. Biosciences, B., *Introduction to Flow Cytometry: A learning guide.* Manual Part, 2000. **1**.
118. Kunisch, E., et al., *Macrophage specificity of three anti-CD68 monoclonal antibodies (KP1, EBM11, and PGM1) widely used for immunohistochemistry and flow cytometry.* Annals of the rheumatic diseases, 2004. **63**(7): p. 774-784.
119. Arnoulet, C., et al., *Four‐and five‐color flow cytometry analysis of leukocyte differentiation pathways in normal bone marrow: A reference document based on a systematic approach by the GTLLF and GEIL.* Cytometry Part B: Clinical Cytometry, 2010. **78**(1): p. 4-10.
120. Prussin, C. and D.D. Metcalfe, *Detection of intracytoplasmic cytokine using flow cytometry and directly conjugated anti-cytokine antibodies.* Journal of immunological methods, 1995. **188**(1): p. 117-128.
121. Maino, V.C. and L.J. Picker, *Identification of functional subsets by flow cytometry: intracellular detection of cytokine expression.* Cytometry, 1998. **34**(5): p. 207-215.
122. Baran, J., et al., *Three-color flow cytometry detection of intracellular cytokines in peripheral blood mononuclear cells: comparative analysis of phorbol myristate acetate-ionomycin and phytohemagglutinin stimulation.* Clinical and diagnostic laboratory immunology, 2001. **8**(2): p. 303-313.
123. Jung, T., et al., *Detection of intracellular cytokines by flow cytometry.* Journal of immunological methods, 1993. **159**(1-2): p. 197-207.
124. Allen, J., *Cause of vocal fold scar.* Current opinion in otolaryngology & head and neck surgery, 2010. **18**(6): p. 475-480.
125. Branski, R.C., et al., *Vocal fold wound healing: a review for clinicians.* J Voice, 2006. **20**(3): p. 432-42.
126. Bless, D.M. and N.V. Welham, *Characterization of vocal fold scar formation, prophylaxis, and treatment using animal models.* Current opinion in otolaryngology & head and neck surgery, 2010. **18**(6): p. 481-6.
127. Long, J.L., *Tissue engineering for treatment of vocal fold scar.* Current opinion in otolaryngology & head and neck surgery, 2010. **18**(6): p. 521-525.
128. Lim, X., et al., *Immediate inflammatory response and scar formation in wounded vocal folds.* Ann Otol Rhinol Laryngol, 2006. **115**(12): p. 921-9.
129. Singer, A.J. and R.A. Clark, *Cutaneous wound healing.* N Engl J Med, 1999. **341**(10): p. 738-46.
130. Roederer, M., *Spectral compensation for flow cytometry: visualization artifacts, limitations, and caveats.* Cytometry Part A, 2001. **45**(3): p. 194-205.
131. Roederer, M., *Compensation in flow cytometry.* Current Protocols in Cytometry, 2002: p. 1.14. 1-1.14. 20.
132. Pilling, D., et al., *Identification of markers that distinguish monocyte-derived fibrocytes from monocytes, macrophages, and fibroblasts.* PloS one, 2009. **4**(10): p. e7475.
133. Biosciences, B., *CD marker handbook*. 2014.
134. Smith, C. and Z. Li, *Role of CD11a and CD11b in corneal wound healing and inflammatory process.* Investigative Ophthalmology & Visual Science, 2004. **45**(13): p. 125-125.

135. Mizgerd, J.P., et al., *Neutrophil emigration in the skin, lungs, and peritoneum: different requirements for CD11/CD18 revealed by CD18-deficient mice.* Journal of Experimental Medicine, 1997. **186**(8): p. 1357-1364.
136. Ahmed, N., et al., *CD45-positive cells of haematopoietic origin enhance chondrogenic marker gene expression in rat marrow stromal cells.* International journal of molecular medicine, 2006. **18**(2): p. 233.
137. Kundrotas, G., *Surface markers distinguishing mesenchymal stem cells from fibroblasts.* Acta Medica Lituanica, 2012. **19**(2).
138. Inoue, T., et al., *Antibodies against macrophages that overlap in specificity with fibroblasts.* Kidney international, 2005. **67**(6): p. 2488-2493.
139. Van Landuyt, K.B., et al., *Flow cytometric characterization of freshly isolated and culture expanded human synovial cell populations in patients with chronic arthritis.* Arthritis research & therapy, 2010. **12**(1): p. R15.
140. Dijkstra, C., et al., *The heterogeneity of mononuclear phagocytes in lymphoid organs: distinct macrophage subpopulations in rat recognized by monoclonal antibodies ED1, ED2 and ED3*, in *Microenvironments in the Lymphoid System*. 1985, Springer. p. 409-419.
141. Fecho, K. and D.T. Lysle, *Morphine-induced enhancement in the granulocyte response to thioglycollate administration in the rat.* Inflammation, 2002. **26**(6): p. 259-271.
142. Iqbal, S., et al., *Progesterone and estrogen influence postexercise leukocyte infiltration in overiectomized female rats.* Applied Physiology, Nutrition, and Metabolism, 2008. **33**(6): p. 1207-1212.
143. Lugli, E., M. Roederer, and A. Cossarizza, *Data analysis in flow cytometry: the future just started.* Cytometry Part A, 2010. **77**(7): p. 705-713.
144. Autissier, P., et al., *Evaluation of a 12‐color flow cytometry panel to study lymphocyte, monocyte, and dendritic cell subsets in humans.* Cytometry part A, 2010. **77**(5): p. 410-419.
145. Pyne, S., et al., *Automated high-dimensional flow cytometric data analysis.* Proceedings of the National Academy of Sciences, 2009. **106**(21): p. 8519-8524.
146. Lugli, E., et al., *Subject classification obtained by cluster analysis and principal component analysis applied to flow cytometric data.* Cytometry Part A, 2007. **71**(5): p. 334-344.
147. Steinbrich‐Zöllner, M., et al., *From transcriptome to cytome: integrating cytometric profiling, multivariate cluster, and prediction analyses for a phenotypical classification of inflammatory diseases.* Cytometry Part A, 2008. **73**(4): p. 333-340.
148. Wakabayashi, Y., et al., *Bcl11b is required for differentiation and survival of αβ T lymphocytes.* Nature immunology, 2003. **4**(6): p. 533-539.
149. Shapiro, H.M., *Practical flow cytometry*. 2005: John Wiley & Sons.
150. Houtz, B., J. Trotter, and D. Sasaki, *BD FACService™ TECHNOTES.* 2004.
151. López-Sánchez, N. and J.M. Frade, *Genetic evidence for p75NTR-dependent tetraploidy in cortical projection neurons from adult mice.* Journal of Neuroscience, 2013. **33**(17): p. 7488-7500.
152. Mills, C., *M1 and M2 macrophages: oracles of health and disease.* Critical Reviews™ in Immunology, 2012. **32**(6).
153. Lee, S., et al., *Distinct macrophage phenotypes contribute to kidney injury and repair.* Journal of the American Society of Nephrology, 2011. **22**(2): p. 317-326.
154. Fujisaka, S., et al., *Regulatory mechanisms for adipose tissue M1 and M2 macrophages in diet-induced obese mice.* Diabetes, 2009. **58**(11): p. 2574-2582.
155. Chipev, C.C. and M. Simon, *Phenotypic differences between dermal fibroblasts from different body sites determine their responses to tension and TGFβ1.* BMC dermatology, 2002. **2**(1): p. 13.

156. Barros, M.H.M., et al., *Macrophage polarisation: an immunohistochemical approach for identifying M1 and M2 macrophages.* PloS one, 2013. **8**(11): p. e80908.
157. Herzenberg, L.A., et al., *Interpreting flow cytometry data: a guide for the perplexed.* Nature immunology, 2006. **7**(7): p. 681.
158. Martin, P., *Wound healing--aiming for perfect skin regeneration.* Science, 1997. **276**(5309): p. 75-81.
159. Robson, M.C., D.L. Steed, and M.G. Franz, *Wound healing: biologic features and approaches to maximize healing trajectories.* Current problems in surgery, 2001. **38**(2): p. A1-140.
160. Enoch, S. and D.J. Leaper, *Basic science of wound healing.* Surgery (Oxford), 2008. **26**(2): p. 31-37.
161. Pohlman, T.H., et al., *An endothelial cell surface factor (s) induced in vitro by lipopolysaccharide, interleukin 1, and tumor necrosis factor-alpha increases neutrophil adherence by a CDw18-dependent mechanism.* The Journal of Immunology, 1986. **136**(12): p. 4548-4553.
162. Hardy, M.A., *The biology of scar formation.* Phys Ther, 1989. **69**(12): p. 1014-24.
163. Nathan, C., *Points of control in inflammation.* Nature, 2002. **420**(6917): p. 846-52.
164. Oberyszyn, T.M., *Inflammation and wound healing.* Front Biosci, 2007. **12**(8): p. 2993-9.
165. Dovi, J.V., L.-K. He, and L.A. DiPietro, *Accelerated wound closure in neutrophil-depleted mice.* Journal of leukocyte biology, 2003. **73**(4): p. 448-455.
166. Park, J.E. and A. Barbul, *Understanding the role of immune regulation in wound healing.* Am J Surg, 2004. **187**(5A): p. 11S-16S.
167. King, S.N., et al., *Vocal fold fibroblasts immunoregulate activated macrophage phenotype.* Cytokine, 2013. **61**(1): p. 228-236.
168. Hanson, S.E., et al., *Characterization of mesenchymal stem cells from human vocal fold fibroblasts.* The Laryngoscope, 2010. **120**(3): p. 546-551.
169. Mills, C.D. and K. Ley, *M1 and M2 macrophages: the chicken and the egg of immunity.* Journal of innate immunity, 2014. **6**(6): p. 716-726.
170. Darby, I.A. and T.D. Hewitson, *Fibroblast differentiation in wound healing and fibrosis.* International review of cytology, 2007. **257**: p. 143-179.
171. Midgley, A.C., et al., *Transforming growth factor-β1 (TGF-β1)-stimulated fibroblast to myofibroblast differentiation is mediated by hyaluronan (HA)-facilitated epidermal growth factor receptor (EGFR) and CD44 co-localization in lipid rafts.* Journal of Biological Chemistry, 2013. **288**(21): p. 14824-14838.
172. Regan, M.C., et al., *The wound environment as a regulator of fibroblast phenotype.* Journal of Surgical Research, 1991. **50**(5): p. 442-448.
173. Desmoulibre, A., et al., *Transforming Growth Factor-ill Induces u-Smooth Muscle Actin Expression in Granulation Tissue Myofibroblasts and in Quiescent and Growing Cultured Fibroblasts.* The Journal of cell biology, 1993. **122**(1): p. 103-111.
174. Chaponnier, C., A. Desmoulière, and G. Gabbiani, *Tissue repair, contraction and the myofibroblast*. 2006: Springer.
175. Branco, A., et al., *Vocal fold myofibroblast profile of scarring.* The Laryngoscope, 2016. **126**(3).
176. Jetté, M.E., S.D. Hayer, and S.L. Thibeault, *Characterization of human vocal fold fibroblasts derived from chronic scar.* The Laryngoscope, 2013. **123**(3): p. 738-745.
177. Vyas, B., et al., *Inhibitory effects of hepatocyte growth factor and interleukin-6 on transforming growth factor-β1 mediated vocal fold fibroblast-myofibroblast differentiation.* Annals of Otology, Rhinology & Laryngology, 2010. **119**(5): p. 350-357.
178. Stephens, M.L., et al., *Reducing, refining and replacing the use of animals in toxicity testing*. Vol. 19. 2013: Royal Society of Chemistry.

179. Kassab, G.S., et al., *Augmenting surgery via multi-scale modeling and translational systems biology in the era of precision medicine: a multidisciplinary perspective.* Annals of biomedical engineering, 2016. **44**(9): p. 2611-2625.
180. Li, N.Y., et al., *Biosimulation of inflammation and healing in surgically injured vocal folds.* The Annals of otology, rhinology, and laryngology, 2010. **119**(6): p. 412.
181. Mi, Q., et al., *Translational systems biology of inflammation: potential applications to personalized medicine.* Personalized medicine, 2010. **7**(5): p. 549-559.
182. Seekhao, N., Jaja, J. Mongeau, L. & Li-Jessen, N. Y. K., *In situ visualization for 3D agent-based vocal fold inflammation and repair simulation.* Supercomputing Frontiers and Innovations, (in press).
183. Li, N.Y., H.K. Heris, and L. Mongeau, *Current understanding and future directions for vocal fold mechanobiology.* Journal of cytology & molecular biology, 2013. **1**(1): p. 001.
184. Levendoski, E.E., C. Leydon, and S.L. Thibeault, *Vocal fold epithelial barrier in health and injury: a research review.* Journal of Speech, Language, and Hearing Research, 2014. **57**(5): p. 1679-1691.
185. Leydon, C., et al., *Epithelial cells are active participants in vocal fold wound healing: an in vivo animal model of injury.* PloS one, 2014. **9**(12): p. e115389.
186. Tse, J.R., Z. Zhang, and J.L. Long, *Effects of vocal fold epithelium removal on vibration in an excised human larynx model.* The Journal of the Acoustical Society of America, 2015. **138**(1): p. EL60-EL64.
187. Novaleski, C.K., M. Mizuta, and B. Rousseau, *Evaluation of dying vocal fold epithelial cells by ultrastructural features and TUNEL method.* Cells Tissues Organs, 2016. **202**(5-6): p. 355-368.
188. Long, J.L., et al., *Epithelial differentiation of adipose‐derived stem cells for laryngeal tissue engineering.* The Laryngoscope, 2010. **120**(1): p. 125-131.
189. *Anti-CD11b/c antibody [OX42] (FITC) (ab112170)*. [cited 2017 January 26]; Available from: http://www.abcam.com/cd11bc-antibody-ox42-fitc-ab112170.html.
190. Noto, K., et al., *Identification and functional characterization of mouse CD29 with a mAb.* International immunology, 1995. **7**(5): p. 835-842.
191. Ridger, V.C., et al., *Differential effects of CD18, CD29, and CD49 integrin subunit inhibition on neutrophil migration in pulmonary inflammation.* The Journal of Immunology, 2001. **166**(5): p. 3484-3490.
192. Thomas, L., et al., *CD44H regulates tumor cell migration on hyaluronate-coated substrate.* J Cell Biol, 1992. **118**(4): p. 971-977.
193. Noonan, K.J., et al., *Spatial distribution of CD44 and hyaluronan in the proximal tibia of the growing rat.* Journal of orthopaedic research, 1996. **14**(4): p. 573-581.
194. Hermiston, M.L., Z. Xu, and A. Weiss, *CD45: a critical regulator of signaling thresholds in immune cells.* Annual review of immunology, 2003. **21**(1): p. 107-137.
195. Bauer, J., et al., *Phagocytic activity of macrophages and microglial cells during the course of acute and chronic relapsing experimental autoimmune encephalomyelitis.* Journal of neuroscience research, 1994. **38**(4): p. 365-375.
196. Nassiri, F., et al., *Endoglin (CD105): a review of its role in angiogenesis and tumor diagnosis, progression and therapy.* Anticancer research, 2011. **31**(6): p. 2283-2290.
197. Sanz-Rodriguez, F., et al., *Endoglin regulates cytoskeletal organization through binding to ZRP-1, a member of the Lim family of proteins.* Journal of Biological Chemistry, 2004. **279**(31): p. 32858-32868.
198. Bevilacqua, M.P., *Endothelial-leukocyte adhesion molecules.* Annual review of immunology, 1993. **11**(1): p. 767-804.

199. Kinashi, T., Y. St Pierre, and T.A. Springer, *Expression of glycophosphatidylinositol-anchored and-non-anchored isoforms of vascular cell adhesion molecule 1 in murine stromal and endothelial cells.* Journal of leukocyte biology, 1995. **57**(1): p. 168-173.
200. Kinashi, T. and T.A. Springer, *Adhesion molecules in hematopoietic cells.* Blood cells, 1994. **20**(1): p. 25-44.
201. Strober, W., *Trypan blue exclusion test of cell viability.* Current protocols in immunology, 2001: p. A3. B. 1-A3. B. 3.
202. Deaglio, S., et al., *CD38/CD31, a receptor/ligand system ruling adhesion and signaling in human leukocytes*, in *Human CD38 and Related Molecules*. 2000, Karger Publishers. p. 99-120.
203. Duncan, G.S., et al., *Genetic evidence for functional redundancy of platelet/endothelial cell adhesion molecule-1 (PECAM-1): CD31-deficient mice reveal PECAM-1-dependent and PECAM-1-independent functions.* The Journal of Immunology, 1999. **162**(5): p. 3022-3030.
204. Famiglietti, J., et al., *Tyrosine residue in exon 14 of the cytoplasmic domain of platelet endothelial cell adhesion molecule-1 (PECAM-1/CD31) regulates ligand binding specificity.* The Journal of cell biology, 1997. **138**(6): p. 1425-1435.
205. Ishizu, A., et al., *Thy-1 induced on rat endothelium regulates vascular permeability at sites of inflammation.* International immunology, 1995. **7**(12): p. 1939-1947.
206. He, H., et al., *Thy-1 supports adhesion of mouse thymocytes to thymic epithelial cells through a Ca2 (+)-independent mechanism.* J Exp Med, 1991. **173**(2): p. 515-518.
207. Ritter, M., et al., *Interaction of CD163 with the regulatory subunit of casein kinase II (CKII) and dependence of CD163 signaling on CKII and protein kinase C.* European journal of immunology, 2001. **31**(4): p. 999-1009.
208. Schaer, D.J., et al., *CD163 is the macrophage scavenger receptor for native and chemically modified hemoglobins in the absence of haptoglobin.* Blood, 2006. **107**(1): p. 373-380.
209. Polfliet, M.M., et al., *The rat macrophage scavenger receptor CD163: expression, regulation and role in inflammatory mediator production.* Immunobiology, 2006. **211**(6): p. 419-425.
210. Macal, C.M. and M.J. North. *Agent-based modeling and simulation: ABMS examples*. in *Simulation Conference, 2008. WSC 2008. Winter*. 2008. IEEE.
211. Macal, C.M. and M.J. North. *Tutorial on agent-based modeling and simulation*. in *Simulation conference, 2005 proceedings of the winter*. 2005. IEEE.
212. Grimm, V., et al., *Pattern-oriented modeling of agent-based complex systems: lessons from ecology.* science, 2005. **310**(5750): p. 987-991.
213. Wiegand, T., et al., *Using pattern‐oriented modeling for revealing hidden information: a key for reconciling ecological theory and application.* Oikos, 2003. **100**(2): p. 209-222.
214. Grimm, V. and S.F. Railsback, *Pattern-oriented modelling: a 'multi-scope'for predictive systems ecology.* Phil. Trans. R. Soc. B, 2012. **367**(1586): p. 298-310.
215. Li, T., Z. Cheng, and L. Zhang, *Developing a Novel Parameter Estimation Method for Agent-Based Model in Immune System Simulation under the Framework of History Matching: A Case Study on Influenza A Virus Infection.* International journal of molecular sciences, 2017. **18**(12): p. 2592.
216. Li, M., W. Du, and F. Nian, *An adaptive particle swarm optimization algorithm based on directed weighted complex network.* Mathematical Problems in Engineering, 2014. **2014**.
217. Moedomo, R.L., et al., *Simulation of influenza pandemic based on genetic algorithm and agent-based modeling: A multi-objective optimization problem solving.* Jurnal Matematika dan Sains, 2010. **15**(2): p. 47-59.
218. Katare, S., et al., *A hybrid genetic algorithm for efficient parameter estimation of large kinetic models.* Computers & chemical engineering, 2004. **28**(12): p. 2569-2581.

219. Gallaher, J., et al., *Hybrid approach for parameter estimation in agent-based models.* bioRxiv, 2017: p. 175661.
220. Folcik, V.A., G.C. An, and C.G. Orosz, *The Basic Immune Simulator: an agent-based model to study the interactions between innate and adaptive immunity.* Theoretical Biology and Medical Modelling, 2007. **4**(1): p. 39.
221. Tong, X., et al., *Development of an agent-based model (ABM) to simulate the immune system and integration of a regression method to estimate the key ABM parameters by fitting the experimental data.* PloS one, 2015. **10**(11): p. e0141295.
222. Wise, S.M., et al., *Three-dimensional multispecies nonlinear tumor growth—I: model and numerical method.* Journal of theoretical biology, 2008. **253**(3): p. 524-543.
223. Hussain, F., et al., *Automated parameter estimation for biological models using Bayesian statistical model checking.* BMC bioinformatics, 2015. **16**(17): p. S8.
224. Crooks, A., C. Castle, and M. Batty, *Key challenges in agent-based modelling for geo-spatial simulation.* Computers, Environment and Urban Systems, 2008. **32**(6): p. 417-430.
225. Windrum, P., G. Fagiolo, and A. Moneta, *Empirical validation of agent-based models: Alternatives and prospects.* Journal of Artificial Societies and Social Simulation, 2007. **10**(2): p. 8.
226. Fehler, M., F. Klügl, and F. Puppe. *Approaches for resolving the dilemma between model structure refinement and parameter calibration in agent-based simulations*. in *Proceedings of the fifth international joint conference on Autonomous agents and multiagent systems*. 2006. ACM.
227. Iooss, B. and P. Lemaître, *A review on global sensitivity analysis methods*, in *Uncertainty Management in Simulation-Optimization of Complex Systems*. 2015, Springer. p. 101-122.
228. Marino, S., et al., *A methodology for performing global uncertainty and sensitivity analysis in systems biology.* Journal of theoretical biology, 2008. **254**(1): p. 178-196.
229. Ten Broeke, G., G. Van Voorn, and A. Ligtenberg, *Which sensitivity analysis method should I use for my agent-based model?* Journal of Artificial Societies & Social Simulation, 2016. **19**(1).
230. Saltelli, A., S. Tarantola, and K.-S. Chan, *A quantitative model-independent method for global sensitivity analysis of model output.* Technometrics, 1999. **41**(1): p. 39-56.
231. McRae, G.J., J.W. Tilden, and J.H. Seinfeld, *Global sensitivity analysis—a computational implementation of the Fourier amplitude sensitivity test (FAST).* Computers & Chemical Engineering, 1982. **6**(1): p. 15-25.
232. Henkel, T., H. Wilson, and W. Krug. *Global sensitivity analysis of nonlinear mathematical models-an implementation of two complementing variance-based algorithms*. in *Proceedings of the Winter Simulation Conference*. 2012. Winter Simulation Conference.
233. Welham, N.V., et al., *A rat excised larynx model of vocal fold scar.* Journal of Speech, Language, and Hearing Research, 2009. **52**(4): p. 1008-1020.
234. Cortés-Sol, A., et al., *Inner capillary diameter of hypothalamic paraventricular nucleus of female rat increases during lactation.* BMC neuroscience, 2013. **14**(1): p. 7.
235. Burns, A.R., C.W. Smith, and D.C. Walker, *Unique structural features that influence neutrophil emigration into the lung.* Physiological reviews, 2003. **83**(2): p. 309-336.
236. Hohsfield, L.A., C.G. Ammann, and C. Humpel, *Inflammatory status of transmigrating primary rat monocytes in a novel perfusion model simulating blood flow.* Journal of neuroimmunology, 2013. **258**(1): p. 17-26.
237. Garg, A., *Multi-parametric flow cytometry for cell phenotyping in surgical vocal fold injuries.* Head & Neck, 2018 (In Review).
238. Tateya, I., et al., *Cell production in injured vocal folds: a rat study.* Annals of Otology, Rhinology & Laryngology, 2006. **115**(2): p. 135-143.

239. Houska, T., et al., *SPOTting model parameters using a ready-made python package.* PloS one, 2015. **10**(12): p. e0145180.
240. Bárdossy, A. and S. Singh, *Robust estimation of hydrological model parameters.* Hydrology and Earth System Sciences, 2008. **12**(6): p. 1273-1283.
241. Strobl, C., et al., *Conditional variable importance for random forests.* BMC bioinformatics, 2008. **9**(1): p. 307.
242. Criminisi, A., J. Shotton, and E. Konukoglu, *Decision forests: A unified framework for classification, regression, density estimation, manifold learning and semi-supervised learning.* Foundations and Trends® in Computer Graphics and Vision, 2012. **7**(2–3): p. 81-227.
243. Strobl, C., et al., *Bias in random forest variable importance measures: Illustrations, sources and a solution.* BMC bioinformatics, 2007. **8**(1): p. 25.
244. Lunetta, K.L., et al., *Screening large-scale association study data: exploiting interactions using random forests.* BMC genetics, 2004. **5**(1): p. 32.
245. Pappenberger, F., I. Iorgulescu, and K.J. Beven, *Sensitivity analysis based on regional splits and regression trees (SARS-RT).* Environmental Modelling & Software, 2006. **21**(7): p. 976-990.
246. Harper, E.B., J.C. Stella, and A.K. Fremier, *Global sensitivity analysis for complex ecological models: a case study of riparian cottonwood population dynamics.* Ecological Applications, 2011. **21**(4): p. 1225-1240.
247. Storlie, C.B., et al., *Implementation and evaluation of nonparametric regression procedures for sensitivity analysis of computationally demanding models.* Reliability Engineering & System Safety, 2009. **94**(11): p. 1735-1763.
248. Huang, B.F. and P.C. Boutros, *The parameter sensitivity of random forests.* BMC bioinformatics, 2016. **17**(1): p. 331.
249. Pereda, M., J.I. Santos, and J.M. Galán, *A brief introduction to the use of machine learning techniques in the analysis of agent-based models*, in *Advances in Management Engineering*. 2017, Springer. p. 179-186.
250. Breiman, L. and A. Cutler, *Random forests-classification description.* Department of Statistics, Berkeley, 2007. **2**.
251. Breiman, L., *Random forests.* Machine learning, 2001. **45**(1): p. 5-32.
252. Menze, B.H., et al., *A comparison of random forest and its Gini importance with standard chemometric methods for the feature selection and classification of spectral data.* BMC bioinformatics, 2009. **10**(1): p. 213.
253. Rodriguez-Galiano, V., et al., *Random Forest classification of Mediterranean land cover using multi-seasonal imagery and multi-seasonal texture.* Remote Sensing of Environment, 2012. **121**: p. 93-107.
254. Liaw, A. and M. Wiener, *Classification and regression by randomForest.* R news, 2002. **2**(3): p. 18-22.
255. Li, N.Y.-K., *Biosimulation of vocal fold inflammation and healing*. 2009, University of Pittsburgh.
256. Jiang, P., et al., *MiPred: classification of real and pseudo microRNA precursors using random forest prediction model with combined features.* Nucleic acids research, 2007. **35**(suppl_2): p. W339-W344.
257. Oshiro, T.M., P.S. Perez, and J.A. Baranauskas. *How many trees in a random forest?* in *International Workshop on Machine Learning and Data Mining in Pattern Recognition*. 2012. Springer.
258. Stănculeanu, D., et al., *Adenocarcinoma versus pancreatic neuroendocrine tumor-case report.* Romanian journal of morphology and embryology= Revue roumaine de morphologie et embryologie, 2017. **58**(3): p. 1091-1097.

259. Thompson, L.D., et al., *Mucinous cystic neoplasm (mucinous cystadenocarcinoma of low-grade malignant potential) of the pancreas: a clinicopathologic study of 130 cases.* The American journal of surgical pathology, 1999. **23**(1): p. 1-16.
260. Thompson, W.A., I. Vertinsky, and J.R. Krebs, *The survival value of flocking in birds: a simulation model.* The Journal of Animal Ecology, 1974: p. 785-820.
261. Butterfield, T.A., T.M. Best, and M.A. Merrick, *The dual roles of neutrophils and macrophages in inflammation: a critical balance between tissue damage and repair.* Journal of athletic training, 2006. **41**(4): p. 457.
262. Virag, J.I. and C.E. Murry, *Myofibroblast and endothelial cell proliferation during murine myocardial infarct repair.* The American journal of pathology, 2003. **163**(6): p. 2433-2440.